Atomic-scale Polarization Structures and Domain Dynamics in $BiFeO_3$ Thin Films

by

Linze Li

A dissertation submitted in partial fulfillment
of the requirements for the degree of
Doctor of Philosophy
(Materials Science and Engineering)
in The University of Michigan
2017

Doctoral Committee:

Professor Xiaoqing Pan, Co-Chair
Assistant Professor Emmanouil Kioupakis, Co-Chair
Adjunct Professor George Graham
Professor Wei Lu

DEDICATION

To my parents Yongxue Li and Qing Fang

wife Ruijie Fan

& daughter Ariel Li

ACKNOWLEDGMENTS

I would like to express my sincere gratitude to my advisor Prof. Xiaoqing Pan for his continuous support and expert guidance throughout my PhD study. I would also like to express my appreciation to Prof. George Graham, Prof. Emmanouil Kioupakis, and Prof. Wei Lu for having served on my committee. Their insightful comments on my work were valued greatly. In addition, I would like to acknowledge my undergraduate research advisor Prof. Jing Lu who introduced me into the academic realm and helped me to prepare for the challenges of graduate research.

All the work in the thesis would be impossible without the help of numerous friends and colleagues. I would like to thank Dr. Christopher Nelson, Dr. Peng Gao, Dr. Yi Zhang (older), Dr. Jacob Jokisaari and EMAL staff Dr. Haiping Sun and Dr. Kai Sun who trained me in TEM and other scientific instruments. I am grateful to Dr. Yi Zhang (younger), Dr. Lin Xie, and Dr. Sungjoo Kim for their contributions to this work. I would also like to thank the staff members of the National Center for Electron Microscopy (NCEM) at the Lawrence Berkeley National Lab, who trained me in and provide me access to use of the TEAM 0.5 and TEAM 1.0, two of the best microscopes in the world.

The work has been done in close collaboration with several other groups. I owe a deep sense of gratitude to Prof. Darrell Schlom, Dr. Alexander Melville, Dr. Carolina Adamo and Dr. Colin Heikes from Cornell University, who grew almost all the $BiFeO_3$ samples I have been working on; and also to Prof. Long-Qing Chen, Dr. Jason Britson, Xiaoxing Cheng, Bo Wang, and Zijian Hong from Penn State University, who have provided theoretical support to most of my research. I would also like to thank Dr. Hans Christen and Dr. Christianne Beekman from Oak Ridge National Lab and Dr. Jan-Chi Yang and Prof. Yinghao Chu from National Chiao Tung University for providing additional samples for this work.

The work was mainly supported by the Department of Energy (DOE) under grant DESC0014430 and the National Science Foundation (NSF) under grant DMR-1420620. The TEM used for this work was funded by the National Science Foundation under grant DMR-0723032. I would also like to acknowledge the National Center for Electron Microscopy at Lawrence Berkeley National Laboratory for their support under the DOE grant DEAC0205CH11231 for user facilities.

TABLE OF CONTENTS

LIST OF FIGURES

LIST OF TBALES

ABSTRACT

Ferroelectric materials have been utilized in a broad range of electronic, optical, and electromechanical applications and hold the promise for the design of future high-density nonvolatile memories and multifunctional nanodevices. The applications of ferroelectric materials stem from the functional structures of domains and domain walls and the ability to switch them by applying an electric field. A fundamental understanding of the microscopic mechanism underlying the domain formation and the domain switching, therefore, is critical for design of practical ferroelectric devices. In this work, a systematic study of atomic-scale polarization structures and microscopic domain-switching processes in ferroelectric $BiFeO_3$ thin films is performed by using atomic-resolution scanning transmission electron microscopy (STEM) and *in situ* transmission electron microscopy (TEM). The presented results, including structures and switching of strongly charged domain walls (sCDWs) and complex phenomena induced by nanoscale impurity defects, shed light on the interplay between ferroelectric polarization and bound charge, strain, or defect-induced local perturbations. This study opens up the possibility for developing novel ferroelectric nanodevices by control of sCDWs or through defect engineering.

CHAPTER 1

Introduction

1.1 Applications of ferroeletric materials

A ferroelectric is generally defined as a material whose spontaneous polarization can be reversed through the application of an external electric field that is greater than the coercive field (Fig. 1.1), a behavior similar to the reorientation of magnetic moments under an applied magnetic field for ferromagnetic materials. Since the discovery of ferroelectricity in $BaTiO_3$ in the mid-1940s, ferroelectrics have become a prototypical example of functional oxides, attracting considerable interest both in theoretical work and device engineering[1-4]. A wide spectrum of functional properties has been found in ferroelectric materials, including strong electromechanical coupling, high non-linear optical activity, pyroelectricity, and non-linear dielectric behavior[3,5-8]. These properties have made ferroelectric materials useful in a variety of electronic, optical, and electromechanical devices, such as ferroelectric varactors[9,10], infrared detectors[11,12], microwave phase filters[13-15], and piezoelectric microsensors and micromotors[16-18]. Most importantly, due to the ability of conversion between two or more stable polarization states by applying an electric field, ferroelectric material can be utilized in an important class of high-density and nonvolatile memories[6,19-23].

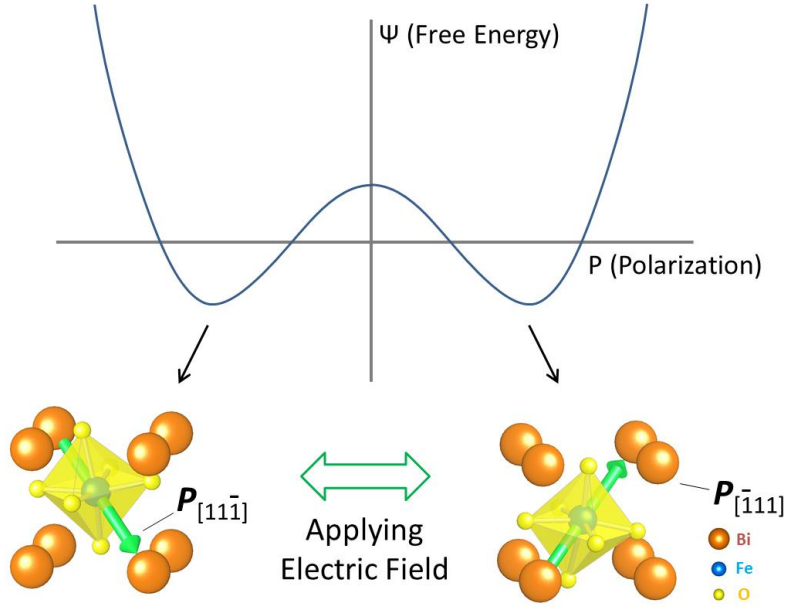

Fig. 1.1 Double well potential model of the ferroelectric polarization
The polarization (***P***) of ferroelectric $BiFeO_3$ is produced by displacive distortions of the cations and oxygen octahedral in the crystal lattice. The ferroelectric can adopt one of eight degenerate polarizations along the $<111>_{PC}$ axis of pseudocubic (PC) unit cell to minimize it's free energy. Polarizations are shown by green arrows. In principle, applying an electric field larger than a critical value can overcome the potential barrier and lead to ferroelectric switching.

Using ferroelectric polarization state to represent binary bits has been realized in a number of approaches for nonvolatile storage. The first example is the now commercially available ferroelectric random access memories (FeRAM), in which the dielectric in a standard dynamic random access memory capacitor is substituted with a ferroelectric[24,25]. It has a number of advantages, such as low-power consumption, fast writing speed and good cyclability, which in most cases is superior to the performance of other non-volatile devices. The readout mechanism, however, requires the memory to be overwritten and is thus known as "destructive readout". To overcome this drawback, several device paradigms have been developed to enable a "nondestructive" read operation. One of the examples is the ferroelectric field effect transistors (FeFET), which combines a semiconductor channel and a ferroelectric gate within a device[26,27]. Although the idea of

FeFET and its first experimental realization was presented several decades ago[8], it continues to attract much interest nowadays, with tremendous progress made to fabricate novel FeFET structure by coupling ferroelectrics with various nanostructures or organic materials[28-32].

Recent progress of producing high-quality oxide thin films has opened up several new possibilities for developing nonvolatile storage with nondestructive read operation on the basis of ferroelectric materials. These include switchable ferroelectric diodes utilizing the coupling between the polarization and interfacial Schottky junction[33-35], and ferroelectric tunneling junctions (FTJs) based on ultrathin ferroelectric films[36-43]. Compared to traditional FeRAM and FeFET, in which a storage unit is comprised of a full device cell, ferroelectric diodes and FTJs can utilize each individual domain as a storage unit. As the critical domain size in a ferroelectric thin film can reach down to the scale of less than 10 nanometers[44-47], these novel devices hold promise for a storage density larger than 10 Tb/inch^2. Moreover, through a gradual change of voltage-controlled domain configurations, memristive behavior with multilevel data storage has also been realized in these device structures[41,48,49].

The polarization of a ferroelectric material can also couple with other physical parameters, such as strain, magnetic order or optical properties. Notably, a novel mixed-phase structure that resembles the 'morphotropic phase boundary' is found in ferroelectric $BiFeO_3$ thin films with an epitaxial strain of ~4%[50-52]. These structures possess a large reversible electric-field-induced strain, demonstrating potential as a substitute for lead-based materials in future piezoelectric applications[53]. A coupling between ferroelectric and magnetic order can enable direct manipulation of magnetism by

applied electric field and vice versa[54,55]. While there are very few examples of the so called "multiferroic" that exhibit both ferroelectricity and ferromagnetism in a single material, indirect coupling between ferroelectric and magnetic properties has been realized through "magnetoelectric" interactions across interfaces in thin-film heterostructures or composite systems, opening the door to the design of practical devices [56-61]. The interaction between ferroelectric polarization and photovoltaic effect has been recently found to lead to a "ferroelectric photovoltaic" effect, in which the direction of the photocurrent can be reversibly switched along with the polarization switching[33,62,63]. Such new degree of control may find applications in novel optoelectronic devices.

Another key aspect for future application of ferroelectric materials is the myriad novel properties recently discovered at ferroelectric domain walls. One of these intriguing properties is the enhanced conductivity of domain walls compared to the surrounding domains, which could be caused by a lattice distortion and the consequent band gap lowering at the local domain wall region[64-68]. Anomalous photovoltaic effect has also been found at domain walls, where the photovoltaic charge separation occurs at the nanoscale steps of the electrostatic potential at these boundaries[69,70]. The observed photovoltaic effect can produce voltages that are significantly higher than the bandgap of the ferroelectric material, and the electric-field control over domain structures allows the photocurrent to be reversed in direction or turned off [69,70]. Ferroelectric domain walls can also become electrically active, carrying net bound charge, as a result of "head-to-head" or "tail-to-tail" polarization configurations. The bound charge at such charged domain walls can gather compensating free charges, resulting in a local insulator-metal transition[71-74]; and can lead to an accumulation of oxygen vacancies, effectively lowering

the local energy bandgap and enhancing the photocurrent[75]. Additionally, the bound charge at the charged domain walls can also affect the properties of the surrounding material by producing a depolarization field. For example, such a depolarizing field can lead to increased electromechanical response and therefore improved piezoelectric properties[76]. As ferroelectric domain walls can be easily created, erased and reconfigured within the same physical volume by external electric fields, these novel properties and functionalities at local domain walls may make them form building blocks for the development of future nanoelectronic devices.

1.2 Polarization structures and domain dynamics in ferroelectric thin films

Since most utilities of ferroelectrics are derived from the polarization configuration and the domain switching, or from their coupling to other material functionalities, an understanding of the static and dynamic properties of ferroelectric domains and domain walls is critical for the control of functional properties and the development of new applications. Recent advances in atomic-level control of thin-film growth, *e.g.* molecular beam epitaxy (MBE) and pulsed laser deposition (PLD), have made it possible to epitaxially grow high-quality ferroelectric thin films, varying from several unit cells to a few hundreds of nanometers in thickness, onto a large variety of single crystal substrates with a precise control over composition, atomic arrangements and interfaces[77-82]. The availability of such high-quality ferroelectric thin films, in conjunction with a broad spectrum of analytical tools, allows unprecedented opportunities to study the properties of ferroelectrics.

Static polarization structures of ferroelectric thin films depend strongly on the boundary conditions at the two interfaces (or surfaces) and thus can often be considerably different from their bulk materials. First, the lattice mismatch between the film and substrate leads to the biaxial-strain mechanical boundary condition[79,83-85]. This biaxial strain can be altered by choosing substrates spanning a wide range of lattice parameters and can reach up to several percent — far beyond where they would crack in bulk[50,86-89]. Such alteration of constraints from the substrates would allow ferroelectric properties of the thin films to be tuned via a strong polarization-strain coupling[79,85,90,91]; allow controlled formation of ferroelastic-ferroelectric domain patterns to release the biaxial strain[92-95]; or allow new phases that do not exist in bulk to be stabilized in the thin films[50,51,88,96,97]. Second, the electrical boundary condition is dependent critically on the free charge compensation capability at the interfaces and can be tailored by choosing substrates or epitaxial buffer layers with different conductivities[98,99]. Such change of electrical boundary condition, coupled with suitable strain boundary condition, would dramatically influence the domain patterns in ferroelectric thin films, resulting in controlled formation of large mono-domains[89], periodic stripe domains[100-103], or arrays of flux-closure domain structures[89,104,105]. Moreover, the polarization states of ferroelectric thin films could also be tuned by controlling the substrate vicinality due to additional symmetry restriction[106,107], or by altering the chemical environment at the free surfaces of the films as a result of local compositional changes[108].

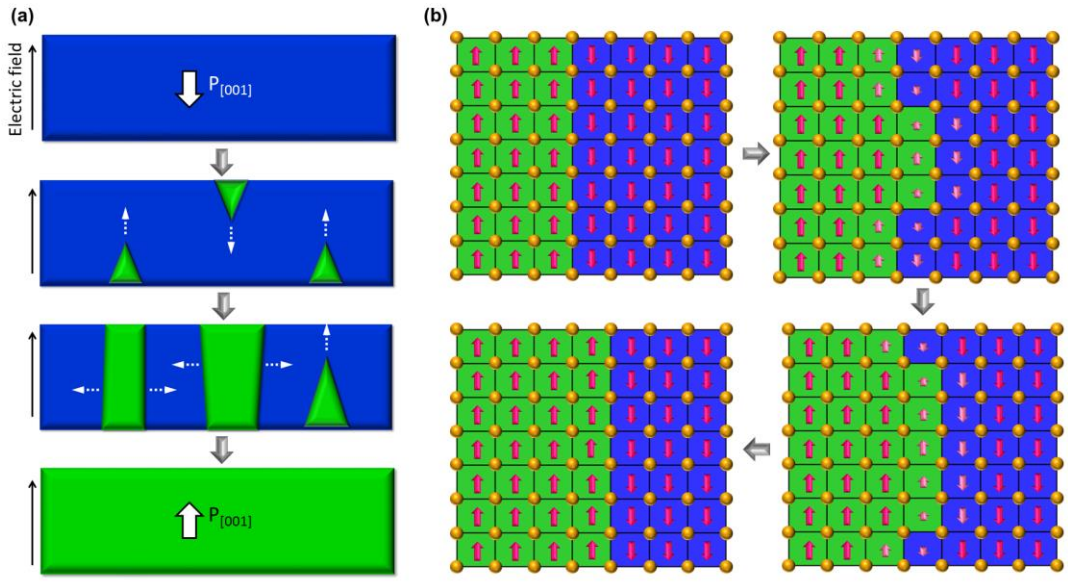

Fig. 1.2 Mechanisms of ferroelectric polarization switching
(a) Three-step switching process in a planar capacitor: first, nucleation of domains with reversed polarization at the interfaces; second, fast forward propagation of domains in the direction of the electric field; and last, slow lateral domain growth in the direction perpendicular to the electric field. **(b)** The classic Miller-Weinreich model, modified with a diffuse-boundary with attenuated polarization, for sidewise domain wall motion: formation of atomically thin nuclei on the domain wall and subsequent growth of the nuclei along the domain wall. At the atomically thin nucleus on the domain wall, the domain boundary is diffused and the polarization is attenuated.

The dynamic process of domain switching in ferroelectric thin films generally occurs in three steps (Fig. 1.2a): first, the nucleation of a domain with a reversed polarization, which usually takes place at the interfaces or defects due to the local high free energy; second, fast forward propagation of domains in the direction of the electric field, as a result of the high energy of the forward charged domain edge; and last, the lateral domain growth in the direction perpendicular to the electric field, enabled by a sidewise motion of the nominal charge-neutral domain wall. Such sidewise domain wall motion, in a classic model proposed by Miller and Weinreich[109], has been thought to occur through the formation of atomically thin nuclei on the domain wall and a subsequent growth of the nuclei along the domain wall (Fig. 1.2b). In real materials, however, the nucleation and growth of newly formed domains, and the motion of pre-

existing domain walls, usually proceed simultaneously and are strongly affected by local variations of free energies caused by interfaces or defects, resulting in highly inhomogeneous process with complex kinetics. Additionally, the interaction between domain switching and interfaces, defects, mechanical strains, or domain walls would usually cause several deleterious phenomena in ferroelectric devices, including a loss of switchable polarization after many switching cycles (fatigue)[7,110,111], a preference of one polarization state over the other (imprint/aging)[7,111], and a failure to retain its stored polarization (retention failure)[112-120].

An aspect of studies on ferroelectric switching dynamics is the correlation between the time of switching, t_s, or the rate of switching identified by the maximum switching current, i_{max}, and the applied field, E[121-123]. Now it is widely accepted that the switching kinetics basically follows the Merz's law: $t_s = t_0 e^{a/E}$ or $i_{max} = i_0 e^{-a/E}$, where a is the "activation field", first introduced by Merz in his studies on single crystals of barium titanate in 1954[121]. To describe the underlying physics of the measured switching time and current, two main models have been developed. The Kolmogorov-Avrami-Ishibashi (KAI) model developed by the group of Ishibashi based on the classical Kolmogorov–Avrami theory of crystallization enables a correct description of switching in systems where the switching process is mainly driven by domain wall propagation and domain coalescence[124,125]. In contrast, the nucleation-limited switching (NLS) model has been developed to describe the switching dynamics of systems where the switching process is dominated by nucleation effects[126]. These two models, however, are statistical treatments aggregating the switching behavior over large volumes; and thus are not well

suited to the description of the local switching phenomena occurring at nanoscale, where the switching depends sensitively on local microscopic structures and electrical details.

1.3 Local probing of ferroelectric materials

To explore local domain structures and switching behaviors in ferroelectric materials, a variety of techniques have been applied (Table 1.1), such as polarized light microscopy[127,128], synchrotron x-ray scattering[129], photoemission electron microscopy (PEEM)[130], and piezoresponse force microscopy (PFM)[2,5,131-133]. The use of polarized light microscopy to study ferroelectric domains can be traced back to the 1950s[134]. Its limitation is the very low spatial resolution (~micrometers) and the destructive nature of the method, where chemical etching is involved. Using synchrotron x-ray scattering, domain switching can be detected with ultra-high time resolution (< 1 ps)[129]. The spatial resolution of this technique, however, is limited by the size of the x-ray probe (~ 50 nm). In PEEM, secondary electrons emitted from a sample in response to the absorption of synchrotron x-ray radiation are used to make an image of ferroelectric domains[130]. Consequently, a high time resolution (< 1ns) can also be achieved in time-resolved PEEM, and its spatial resolution is generally no less than tens of nanometers.

	X-ray scattering	PEEM	PFM	In situ TEM	Aberration-corrected TEM
Spatial resolution	~50 nm	~50 nm	5 – 10 nm	< 1 nm	< 0.1 nm
Time resolution	< 1 ps	< 1 ns	seconds	~30 ms	--

Table 1.1 Techniques used to study ferroelectrics
Spatial and time resolution that are currently available for different methods used to study ferroelectric domain structures and polarization switching.

Compared to the other techniques, PFM has become the predominant method to study ferroelectric polarization configuration and domain switching in recent years[2,5,131-133]. As a contact-mode scanning probe microscopy (SPM) technique, PFM works by electrically biasing a conductive SPM tip and measuring the local surface displacements via the converse piezoelectric effect. It can be easily done in conjunction with other scanning probe microscopy, such as atomic force microscopy (AFM) and conductivity mapping, allowing a number of physical parameters to be explored complementarily[37,64,135]. Today a deep knowledge exists about the cantilever-ferroelectric surface interaction[2,5], and the spatial resolution of PFM can generally reach an order of 5-10 nm. At such scale, the static domain patterns, or any change of them upon polarization switching, can be unambiguously determined in most situations. However, the local microscopic structures of defects that commonly exist in ferroelectrics, which could be just 1-2 unit cells (~ 1 nm) in dimension but may be critical in controlling the polarization configuration and the switching dynamics, are still missing. On the other hand, the time resolution of PFM and other SPM based techniques has been limited by the scanning speed of the probe. As a result, in most cases only stable domain configuration before and after switching can be easily captured by PFM, and the detection of intermediate stages of domain evolution that occur at short time scales (less than a few seconds) remains impossible by now.

The revolution in studies of the structure and switching of ferroelectric domains and domain walls occurred with recent advances in transmission electron microscopy (TEM)[136]. Atomic-scale high-resolution TEM (HRTEM) or scanning transmission electron microscopy (STEM) allow direct imaging of atomic columns with sub-angstrom

resolution to determine the exact polarization structures in ferroelectric crystals. *In situ* TEM enables a real-time observation of the domain evolution under an electrical bias with simultaneous both high spatial (< 1 nm) and temporal (30 ms) resolution, in which the critical role of interfaces and different types of defects can be fully accounted for. In addition, a wide range of advanced TEM techniques, including energy-dispersive spectroscopy (EDS) and electron energy-loss spectroscopy (EELS), can be employed, making it possible to determine chemical composition and electronic structure with atomic resolution. Combining all these techniques within a single TEM instrument, a direct correlation can be established between the properties of ferroelectrics and the underlying physical microstructures. This provides a fundamental understanding of complex phenomena in ferroelectric materials.

1.4 Bismuth ferrite ($BiFeO_3$)

$BiFeO_3$ is an extremely rare case of a single-phase room-temperature multiferroic, exhibiting coupled ferroelectric ($T_C \sim 1{,}103$ K) and antiferromagnetic ($T_N \sim 650$ K) order[137,138]. Its bulk crystal has a rhombohedral structure (Fig. 1.3a), which can also be envisioned as two pseudocubic (PC) perovskite unit cells connected along the body diagonal, with the two oxygen octahedra in the connected perovskite units rotated clockwise and counterclockwise around this axis by 13.8°[138]. Structures of epitaxial $BiFeO_3$ films with tensile or moderate compressive (< ~4.5%) misfit strain imposed by underlying substrates are monoclinically distorted, but closely resemble the bulk rhombohedral phase, and are therefore usually referred to as "*rhombohedral*-like (*R*-like)" structures[139]. In pseudocubic unit cells of the *R*-like structure (Fig. 1.3b left), the

oxygen octahedra and the central Fe cation are displaced from their respective positions at the face and body centers, giving rise to a large spontaneous polarization (~100 μC cm^{-2}) along the $<111>_{PC}$ directions**.** Rotations between polarization variants in the *R*-like $BiFeO_3$ can be 71° (ferroelastic-ferroelectric), 109° (ferroelastic-ferroelectric), or 180° (ferroelectric), yielding three types of domain walls. Under a large compressive epitaxial strain exceeding ~4.5%, $BiFeO_3$ can also be stabilized into a monoclinic structure that is "*tetragonal*-like" (*T*-like)[139]. In the *T*-like structure (Fig. 1.3b right), the Fe atom is five-coordinated, forming an oxygen square-pyramidal that is displaced from the center of the pseudocubic unit cell. This gives rise to a giant polarization (~150 μC/cm^2) oriented along the $[001]_{PC}$ direction.

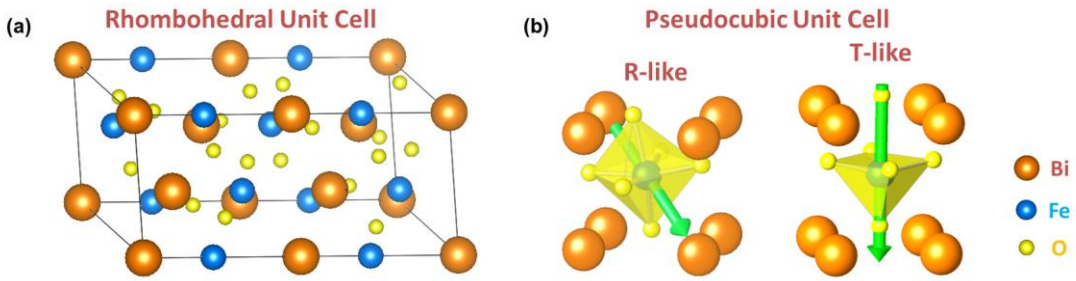

Fig. 1.3 Atomic structure of $BiFeO_3$
(a) Atomic model of the rhombohedral structure of $BiFeO_3$. **(b)** Atomic models of the pseudocubic structures of *R*-like and *T*-like $BiFeO_3$. Polarizations are shown by green arrows.

The *R*-like and *T*-like $BiFeO_3$ thin films are now being widely studied, and have been found to possess numerous functional properties, such as switchable ferroelectric conductivity[33-35], photo-electricity[33,62,63], large piezoelectricity[50-52], and domain wall conductivity[64,65,67,68]. To understand the physics of these emergent properties, a microscopic study of the ferroelectric domains in $BiFeO_3$ thin films using the state-of-the-art TEM techniques is required. The discovered domain formation mechanism and

domain switching dynamics in the study of $BiFeO_3$ thin films could also be also be applicable to a large group of ferroelectric materials.

CHAPTER 2

Transmission Electron Microscopy on Ferroelectrics

2.1 Preparation and artifacts of TEM specimen

Preparing a high-quality TEM specimen is of paramount importance for TEM experiment. Since the TEM specimen must be electron transparent and representative of the material, it should be thin, from several nanometers to a hundred nanometers in thickness, uniform and with little damage of the structure. The specimen of a thin-film heterostructure can be prepared either into a cross-sectional view, with its growth direction perpendicular to the incident electron beam; or into a planar view, with the growth direction parallel to the electron beam. Compared to planar-view TEM specimens, cross-sectional specimens are much more commonly used to study ferroelectric oxides, because it is especially advantageous to resolve polarization structures, interfaces, and defects buried in the bulk films, which are not easily accessible by conventional surface probes.

A number of methods have been developed to prepare a high-quality TEM specimen and the preparation process is now becoming more and more specialized and sophisticated[8,140-142]. One of the most commonly used methods for preparing specimens of ferroelectric oxides, however, remains to be the very conventional one, with general processes consisting of cutting, mechanical polishing, and ion-beam milling. The major advantage of this method is that it allows preparation of high-quality sample with easy

operation at low cost. In recent years, along with the development of the focused ion beam (FIB) microscope, various FIB based TEM-specimen preparation techniques have become well established[141,143]. These FIB-based methods enable the preparation of large, uniformly thick, and site-specific samples. They are especially useful for certain systems where the conventional TEM-specimen preparation method (cutting, mechanical thinning and ion-beam milling) is not applicable. These systems include, for example, samples that are very hard to be cut and polished, samples that are too fragile and tend to crack during mechanical thinning, or samples that need to be prepared to fit the dimensions of specially designed TEM holders.

As the preparation of TEM specimen involves thinning the sample to electron transparent, this process can lead to various artificial effects. A number of studies of ion-beam milling effect on TEM specimens point out that the ion-beam not only leads to material removal on the specimen surface by the sputtering process, but also in some cases can result in a surface layer with unwanted structural changes that may extend up to several tens of nanometers into the material[144,145]. More specifically, depending on the applied energy of ion milling (usually within 0.1 – 5 keV) and the physical properties of the specimen, the energetic ion-beam could induce artifacts such as vacancies, amorphization, lattice damage or transformation, re-deposition, and ion implantation. It may also cause thermal effects due to milling induced temperature arising or electrical charging effects. To minimize the artifacts induced by the ion-beam milling, general recipes for the milling process are developed for different materials, and for both conventional and FIB based methods. And specially designed low-energy, low-angle argon ion milling instruments, such as NanoMill, have also been recently available for

further removing the damaged layer and final thinning of conventionally prepared or FIB prepared TEM specimens. As a result of the well established procedures of the thinning processes, the prepared TEM specimens are in most cases with only little ion-beam-induced artifacts and well representative of the material of interest.

Other than ion-beam induced artifacts, TEM specimens may also undergo a structural relaxation during the thinning process. This relaxation can be significant in certain systems. Fox example, when the cross-sectional TEM specimen of a highly strained $BiFeO_3$ thin film grown on $LaAlO_3$ substrate is thinned to be ~ 50 nm thick along the beam direction, a transition of $BiFeO_3$ structure from the mixed rhombohedral-tetragonal phase that resembles the 'morphotropic phase boundary' to a pure stress-relaxed rhombohedral-like phase is observed[146]. However, a phase transition has been rarely found for specimens of single-phase ferroelectric thin films with moderate or little strain. On the other hand, it is also well known that when the thickness of a ferroelectric thin film is below a critical value, its spontaneous polarization may undergo a significant reduction or eventually annihilate. This may also apply to the TEM specimen along its thinned dimension. The reported critical thicknesses of 2~5 nm for polarization suppression[118,147-149], however, are usually far below the thickness of a TEM specimen, typically ranging from 20 to 100 nm. Therefore, in most TEM specimens such polarization relaxation effect is negligible as well.

2.2 Diffraction-contrast imaging of ferroelectric domains

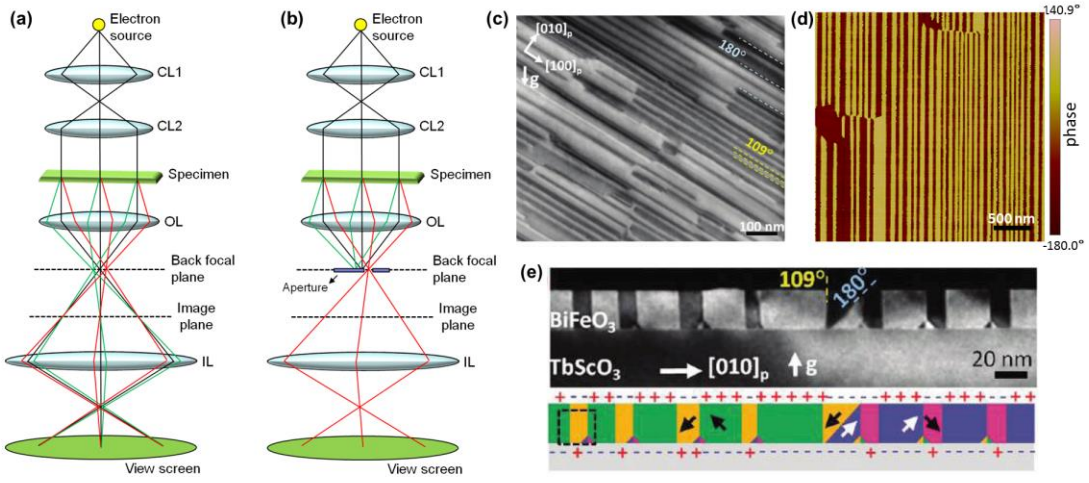

Fig. 2.1 Diffraction-contrast TEM imaging
(a) Ray diagram of normal TEM imaging with parallel illumination, which incorporates two condenser lens (CL1 and CL2), objective lens (OL), and intermediate lens (IL) to image the specimen. Colored ray traces follow specific diffraction angle from each region. **(b)** Ray diagram of diffraction-contrast TEM imaging whereby an aperture is inserted into the back focal plane. In this case, only the red traces are selected to form a dark-field diffraction-contrast image. Alternatively, the black traces can be selected to form a bright-field diffraction-contrast image. **(c)** Bright-field diffraction-contrast image of a planar-view specimen of $BiFeO_3$ thin film grown on $TbScO_3$ substrate, showing striped domain patterns[89]. **(d)** PFM phase image of the same $BiFeO_3$ thin film, showing similar striped domain patterns. **(e)** Dark-field diffraction-contrast image of a cross-sectional specimen of the same $BiFeO_3$ thin film, showing not only striped domain structures but also arrays of small triangular domains at the $BiFeO_3/TbScO_3$ interface[89].

One of the most commonly used imaging modes in TEM studies of ferroelectrics is the diffraction-contrast imaging, which is also known as "dark-field/bright-field" imaging. Compared to normal TEM imaging (Fig. 2.1a), where the image contrast consists of signals from the transmitted beam (black traces in Fig. 2.1a) as well as the diffracted beams (green and red traces in Fig. 2.1a), a dark-field image is generated via only using selected diffracted beams by carefully tilting the TEM specimen and putting an appropriate aperture at the back focal plane (Fig. 2.1 b). In an oversimplified picture, the diffracted beams could be viewed as reflections by different crystal planes; and each plane carries certain structural information of orientation and symmetry. Consequently, in the dark-field image, only the domains with structural information corresponding to these

selected diffracted beams will appear bright, while the other domains remain to be dark. Alternatively, a bright-field image can be generated by only selecting the transmitted beam when the TEM specimen is tilted, and in this case the domain contrast is reversed compared to the dark-field image. Such bright-dark contrast of ferroelectric domains in the dark-field/bright-field imaging can be resolved with a spatial resolution up to ~1 nm. In addition, this imaging mode also leads to distinct contrast to defects such as dislocations, which is useful for observing their interactions with the domain structures.

An example of a bright-field planar-view image of a $BiFeO_3$ thin film sample is shown in Fig. 2.1c[89]. This planar-view TEM image is made in comparison with a PFM image (Fig. 2.1d) of the same $BiFeO_3$ sample; and they both show stripe-like domain configurations, revealing the ability of TEM diffraction-contrast image to probe ferroelectric domains. In a dark-field cross-sectional TEM image of this sample (Fig. 2.1e), the stripe-like domain structures are also shown; and more detailed structure information, *i.e.*, small triangular domains induced by the build-in fields at the ferroelectric/substrate interface[89], which are absent in the planar-view TEM and PFM images, are observed as well. This indicates that, compared to conventional surface-probe PFM methods, the cross-sectional diffraction-contrast TEM imaging is advantageous for studying the interface effect of ferroelectrics.

2.3 Atomic-scale imaging and polarization mapping

To explore the atomic-scale mechanism underlying the properties of ferroelectrics, advanced aberration-corrected HRTEM or STEM imaging with sub-angstrom resolution is required. HRTEM imaging is also known as phase-contrast

imaging, in which the ray diagram generally adopts the normal configuration shown in Fig. 2.1a; and the phase change information of the electron beam wave-front, as a result of its interaction to local atomic potentials within the TEM specimen, is employed to generate the image. The recently developed "negative spherical-aberration (C_S) phase-contrast imaging" has been effectively used to resolve cation columns as well as oxygen[150,151]. In more general case of HRTEM imaging, however, due to its coherent nature, the phase contrast is not necessarily related to real atomic structure and the interpretation of such contrast is complex. Furthermore, only a slight variation of sample thickness or orientation, or aberrations in the objective lens, will dramatically affect the image contrast, making the imaging condition and specimen preparation for HRTEM quite demanding.

Compared to HRTEM, STEM is much more widely used to study ferroelectric materials, due to its easier operation and the fact that its image contrast may be readily related to local atomic structures. In STEM imaging a fine electron probe is focused and scanned sequentially on the specimen and a detector is placed below the specimen to form the image (Fig. 2.2a). The contrast of the STEM image depends on the detector's geometry. In most applications, dark-field and bright-field detectors are combined to obtain dark-field and bright-field STEM images. The dark-field STEM image, especially the high-angle angular dark-field (HAADF) image, is currently the most commonly used STEM method for quantitative studies of ferroelectric microstructures, because of its unsurpassed advantages. First, the intensity contrast (C) of the HAADF image is directly proportional to the atomic number (Z) as ($C \sim Z^{1.7}$)[152], and therefore the image can be easily interpreted as a direct mapping of atoms. Second, HAADF image is robust to slight

variation in sample thickness and small deviations of the sample zone axis with respect to the direction of the incident electron beam. However, in HAADF images a direct observation of light elements with low atomic numbers, e.g. hydrogen, nitrogen, carbon and oxygen, are quite challenging[153]. Another powerful STEM method developed recently is the annular bright-field (ABF) imaging technique[154,155]. Although its image contrast is very sensitive to the sample thickness or orientation, and may not be directly related to the atomic numbers, its capability of imaging both light elements and heavy ones simultaneously makes measurement of all ions' positions in a ferroelectric oxide possible.

In atomic-resolution HRTEM/STEM images, the position of each atomic column can be measured by fitting the atomic columns as two-dimensional (2D) Gaussian peaks with a precision up to several picometers[89,156,157]. Based on such measured positions, the strain distribution can be directly mapped by calculating the lattice parameters of each unit cell; and local polarization vectors may also be determined by calculating the atomic displacements between different ions[96,163]. Although the absolute polarization value is not directly achievable unless the positions of oxygen atoms are measured, the polarization direction, for a material with a structure already known, can be determined unambiguously from the heavy cations only. In $BiFeO_3$, for instance, the polarization can be determined from HAADF imaging (Fig. 2.2b,c), where the Bi columns appear as the brighter dots, the Fe columns show weaker contrast, and the oxygen atoms are not visible. A vector in the image plane, $\boldsymbol{D_{FB}}$, can be defined as the atomic displacement of the Fe cation from the center of the unit cell formed by its four Bi neighbors[89,158]. This $\boldsymbol{D_{FB}}$ vector, as the dominant manifestation of the ferroelectric polarization in $BiFeO_3$,

points towards the center of the negative oxygen charges and is exactly opposite to the polarization in the image plane. Therefore, $-\boldsymbol{D_{FB}}$ vectors can be used to estimate the polarization of $BiFeO_3$ and are called "polarization vectors". This polarization mapping technique based on HAADF STEM image has been used as a main approach to study the atomic-scale polarization structures of nanodomains and domain walls in $BiFeO_3$ thin films in this work.

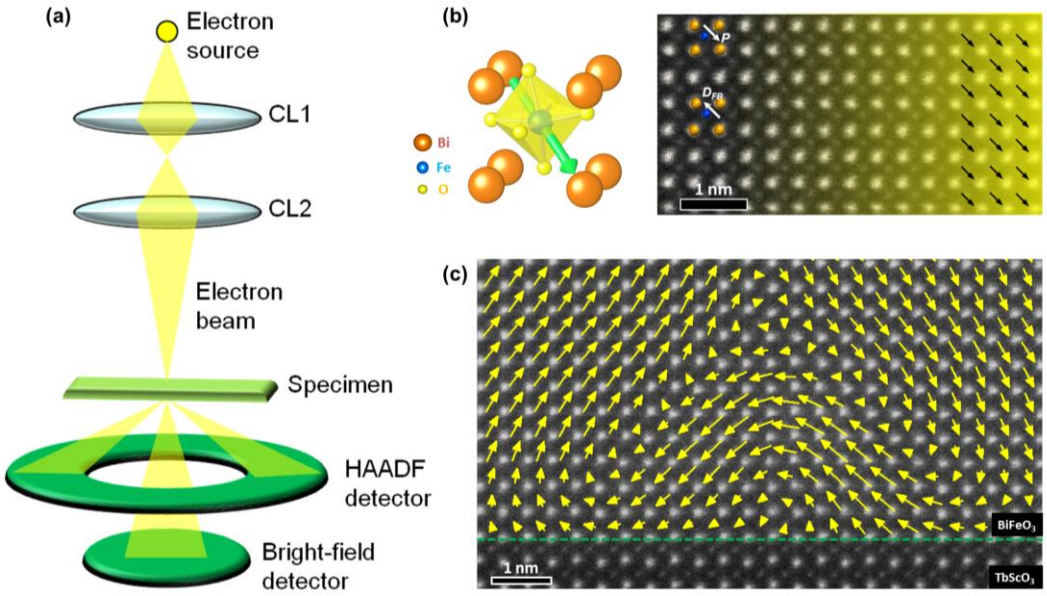

Fig. 2.2 STEM imaging and quantitative mapping of polarization
(a) Ray diagram of STEM imaging in which a convergent beam is focused by condenser lens (CL) system, here shown by CL1 and CL2, and scanned sequentially on the specimen. This technique incorporates various specialized detectors placed below the specimen to measure specific specimen-electron interaction signals. Here a high-angle annular dark-field (HAADF) detector and a bright-field detector are used. **(b)** Polarization mapping techniques based on HAADF STEM imaging. In the pseudocubic unit cell of $BiFeO_3$ (left), the polarization (marked by the green arrow) is caused by an offset of the oxygen octahedron and the central Fe cation from the body-center of Bi cation sub-lattices, and Fe is displaced relative to Bi along the same direction as the oxygen octahedron. Therefore, the polarization ($\boldsymbol{P}$) can be determined by measuring the atomic displacements ($\boldsymbol{D_{FB}}$) between the heavy Bi and Fe cations in a HAADF image (right). The black vectors overlaid on the right side of the HAADF image mark the polarization directions. **(c)** Spatial distribution of polarization vectors ($-\boldsymbol{D_{FB}}$) overlaid on a HAADF STEM image of a vortex-domain structure forming at a 109° domain boundary by addition of a pair of 180° triangle domains right above a $BiFeO_3/TbScO_3$ interface.

2.4 *In situ* TEM on ferroelectric domain switching

As ferroelectric domains and their evolution can be readily observed by several different imaging modes in a standard TEM, an *in situ* TEM experiment on ferroelectric switching only requires an electric field to be applied across the TEM specimen. Applying such electric field, however, usually needs the specially designed sample configurations and *in situ* TEM holders. In early *in situ* TEM studies of ferroelectric switching, the electric field can only be applied parallel to the electron-beam direction by using two parallel TEM copper grids (Fig. 2.3a)[159-161]. In this configuration the magnitude of the actual field applied to the imaging area of the specimen is difficult to estimate due to the presence of vacuum gaps between the copper grid electrodes and the specimen. Along with recent advances in miniaturization of the electrical system for the *in situ* TEM holder, a number of alternative approaches have been developed, allowing the application of an electric field perpendicular to the beam direction and the quantification of the actual applied electric field. For example, Tan *et al.* directly deposited gold films on the TEM specimen surface to generate an electric field (Fig. 2.3b)[162-164]. Alternatively, Sato *et al.* cut a small piece of specimen out from the single crystal of lead magnesium niobate-lead titanate and attached it between two parallel electrodes on a specially designed TEM grid, by using the FIB "lift-out" method (Fig. 2.3c). The TEM grid was then loaded on an electrical biasing specimen holder and an electric field was applied through the sample[165].

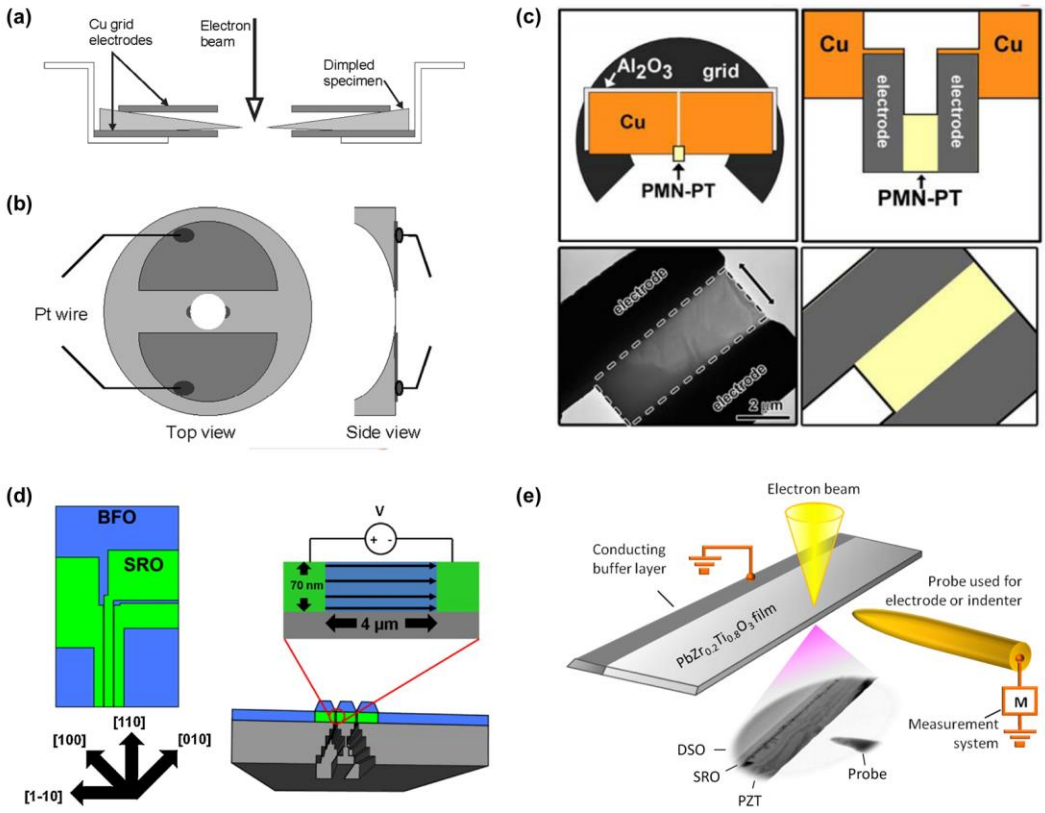

Fig. 2.3 Methods to apply an electric field in *in situ* TEM
(a) Two parallel copper grid electrodes are used to apply an electric field parallel to the electron beam[159-161]. **(b)** Two half-circle shaped gold electrodes are directly deposited on the surface of the TEM specimen to generate an electric field across the region of interest in TEM observations -- the electron transparent areas at the two small dark sites at the edge of the central perforation[162-164]. **(c)** A specially designed *in situ* TEM grid[165]. Here, a small piece of lead magnesium niobate-lead titanate (PMN-PT) specimen is cut and attached between the two parallel electrodes by using the FIB "lift-out" method. Top left and right panels show the whole view and the enlargement around the specimen part. Bottom left and right panels show the low-magnification image of the TEM specimen and the corresponding schematic. In the bottom left panel, the electric field is applied between the two electrodes along the direction indicated by the arrow, and the dotted square indicates the region of interest in TEM observations. **(d)** A specially designed heterostructure sample for *in situ* experiments: left and right panels show a planar-view and a side-view of the $BiFeO_3$ (BFO, blue) / $SrTiO_3$ (STO, grey) heterostructure with epitaxial planar-electrodes of $SrRuO_3$ (SRO, green)[166,167]. **(e)** Integration of scanning probe into an *in situ* TEM specimen holder[176]. Here, the beam is incident to the cross-sectional specimen of $PbZr_{0.2}Ti_{0.8}O_3$ (PZT) grown on $DyScO_3$ (DSO) substrate, an epitaxial back electrode of $SrRuO_3$ (SRO) is grounded, and the probe is the mobile electrode.

Thanks to the advanced techniques of growing high-quality thin films with precisely controlled hetero-structures and interfaces, epitaxial electrodes that are in direct contact with ferroelectric thin films have now also been widely used to apply electric field inside the *in situ* TEM. Winkler *et al.* prepared samples by growing an epitaxial

electrode $SrRuO_3$ layer on $SrTiO_3$, followed by lithography and a precise ion-milling step to define the complex planar-electrode structure, and a second growth of an epitaxial $BiFeO_3$ layer on top of the device structure (Fig. 2.3d)[166,167]. However, this method only permits the application of an in-plane electric field rather than the out-of-plane electrical field, which is more commonly used in practical applications involving ferroelectric thin film materials. The recent integration of scanning probe into a TEM specimen holder allows easy application of out-of-plane electrical fields to switch the ferroelectric film[53,136,168,169]. Using such an *in situ* holder, an electric field along the normal of the film can be introduced by applying a voltage between the scanning surface probe and a planar epitaxial bottom electrode, as is depicted schematically in Fig. 2.3e. The results of the *in situ* TEM studies presented in this work were obtained with these probe-type *in situ* holders.

CHAPTER 3

Ferroelectric Charged Domain Walls in $BiFeO_3$

3.1 Background

Enhanced conductivity observed at ferroelectric domain walls opens the door for the development of novel applications in logic and memory nanodevices using ferroelectrics[64-68,71,73]. Most observed domain walls are, however, nearly charge-neutral due to a minimization of the electrostatic energy. At such uncharged domain walls, only thermally activated conductivity with very low current has been shown[64-68], which impedes the potential applications. Charged domain walls (CDWs), on the other hand, are electronically active due to the accumulation of bound charge, which may gather compensating free charges, allowing higher conductivity than uncharged domain walls[71,73,158,170-172].

In general, two types of CDWs can be found in proper ferroelectrics[73]. The first type forms when the equilibrium configuration of an uncharged domain wall is perturbed during polarization switching or domain wall bending caused by an external field. These CDWs are weakly charged and show transient, enhanced conductivity 10 to 10^3 times that of the bulk[71]. They are usually unstable and tend to relax to low-energy, uncharged orientations after removal of the external field[170]. Although defect pinning can increase the stability of such CDWs, this mechanism relies critically on the local defect microstructure, making these CDWs impractical for reliable, reconfigurable devices. In

contrast, the second type forms as a result of direct “head-to-head” or “tail-to-tail” polarization configurations and is stabilized through the compensation of accumulated free charge carriers without defect pinning[73,158,171,172]. These CDWs are therefore strongly charged and are referred to as strongly charged domain walls (sCDWs). Recent experimental investigations have demonstrated that a quasi-two-dimensional electron gas (q-2DEG) can form at these sCDWs, leading to steady metallic conductivity 10^9 times that of the bulk[73]. Consequently, the sCDWs hold more promise for device applications.

SCDWs have so far been explored in only a few works in ferroelectric thin films using conventional surface probes such as PFM and conductive AFM (c-AFM)[72,74]. Contrary to the dramatically enhanced steady metallic conductivity (10^9 times that of the bulk) measured at sCDWs in bulk crystals of $BaTiO_3$[73], the observed conductivity at the sCDW in the thin films is only slightly or moderately enhanced (10 to 10^3 times that of the uncharged domains)[72,74]. One possible cause is that the sCDWs observed by PFM may be in fact only present at the top surface and do not penetrate to the bottom interface of a film, as a result of the formation of small nanodomains associated with the sCDW beneath the surface. Therefore, a study of the structures and dynamic behaviors of sCDWs in the cross-section view is critical to understanding the film properties at the local region. Moreover, different types of sCDWs buried beneath the surface[156,158,173,174] have also been observed by cross-sectional TEM, but a direct manipulation of them remains impossible by conventional surface approaches.

Here, with a combination of atomic-resolution STEM, *in situ* TEM[136,175], and phase-field simulations, a systematic study on the atomic-scale polarization structures and switching dynamics of nanoscale sCDWs is performed in cross-sectional $BiFeO_3$ thin

films. The results show that, while the bulk domains in $BiFeO_3$ possesses a *R*-like structure, the sCDW is *T*-like; and a reversible switching of the sCDW can be induced by an applied electric field. During the switching process, a dramatic resistive switching is observed as the length of the sCDW surpasses a critical value. This leads to the highest resistance changes (off/on ratio ~ 10^5) ever reported in ferroelectric memories, including ferroelectric tunneling junctions[37,39,40] and switchable ferroelectric diodes[33,35].

3.2 Experimental and theoretical methods

Film growth: $(001)_{PC}$ oriented 20 nm and 5 nm thick $BiFeO_3$ films, and 20 nm thick $BiFeO_3$ films with the additional 20 nm thick epitaxial $La_{0.7}Sr_{0.3}MnO_3$ bottom electrodes, were grown on single crystal $(110)_O$ $TbScO_3$ surfaces by the same molecular-beam epitaxy method described elsewhere[89] (subscripts PC and O are used to indicate pseudocubic and orthorhombic indices, respectively).

TEM experiments: TEM specimens were prepared by mechanical polishing followed by argon ion milling. The specimen was firstly polished to a thickness of ~20-30 μm in wedge shape using a tripod polisher. Then it was further milled to electron transparency by Gatan Precision Ion Polishing Systems, with an ion-gun voltage of 4 kV and incidence angle of ±4°. At the final step of ion milling, a voltage of 0.1 kV was used to remove amorphous material on the surface. Diffraction-contrast imaging was performed using a JEOL 3011 operated at 300 kV, in which the TEM specimen was tilted slightly off the zone axis and aligned in the two-beam condition. Atomic-resolution HAADF STEM imaging was performed using the TEAM 0.5 microscope at the National Center for Electron Microscopy in Lawrence Berkeley National Laboratory. The

accelerating voltage, convergence angle of the incident electrons, and the collection angle for HAADF imaging are 300 kV, 29 mrad and 79-200 mrad, respectively. The HAADF images were further processed, following the methods described in Chapter 2.3, to get accurate mapping of the lattice parameters and polarization vectors (-$\boldsymbol{D_{FB}}$). Local domain switching was performed by *in situ* TEM using a JEOL 3011 operated at 300 kV, with a custom-designed Nanofactory TEM holder with a piezo-driven probe. Electrical voltage was applied between a biased movable tungsten tip and the conductive buffer layer $La_{0.7}Sr_{0.3}MnO_3$ bottom electrode, which was connected to the holder ground using silver paint.

*PFM and scanning spreading resistance microscopy (SSRM)***:** PFM and SSRM measurements were carried out on an NT-MDT Spectra scanning probe microscope using Budget Sensor Pt/Cr-coated tips. The PFM AC signal was applied to the sample with the tip held at ground, and the PFM response was collected near the tip-sample resonance to improve the signal to noise ratio. For switching, a fixed DC bias was applied to the tip during scanning. Spreading resistance was measured immediately after switching.

Phase-field simulations: $BiFeO_3$ thin-film domain structures were simulated using the phase field approach that has been described extensively in previous publications[176-178]. Domain structures were modeled as continuous distributions of the three polar components, P_i, while the antiferromagnetic behavior of $BiFeO_3$ was neglected[179]. Starting from an initial polarization distribution to describe an experimentally observed domain structure, the polarization components were evolved toward a local minimum in the total system free energy, F, by solving the time dependent Ginzburg-Landau equation:

$$\frac{\partial P_i}{\partial t} = -L\frac{\delta F}{\delta P_i} \quad (i = 1, 2, 3) \qquad \text{(Eq. 3.1)}$$

where L is a constant related to the domain wall mobility that is taken to have a value of one in the simulations. Here, total free energy consisted of contributions from the bulk free energy of $BiFeO_3$, electrostatic energy of interactions between polarization bound charges, mechanical energy from long range elastic interactions and gradient energy associated with domain walls. The bulk free energy of $BiFeO_3$ (f_{bulk}) was described by a fourth-order Landau polynomial with respect to the polarization

$$f_{bulk} = \alpha_1(P_1^2 + P_2^2 + P_3^2) + \alpha_{11}(P_1^4 + P_2^4 + P_3^4) + \alpha_{12}(P_1^2P_2^2 + P_2^2P_3^2 + P_3^2P_1^2) \qquad \text{(Eq. 3.2)}$$

for the stress-free bulk material utilizing phenomenological constants from prior publications[176,179,180]. These coefficients, in SI units, were $\alpha_1 = 4.9(T - 1103) \times 10^5$, $\alpha_{11} = 6.50 \times 10^8$, and $\alpha_{12} = 1.0 \times 10^8$ [176]. The simulation used room temperature of $T = 298$ K.

Electrostatic and mechanical energy were included through long-range electric and elastic stress fields in the system. Expressions for these contributions to the energy are described in previous publications[178,181]. The distribution of the electric potential in the system was found for a given polarization distribution by solving the Poisson equation using the background dielectric constant[182] assumed to be 10. This portion of the dielectric constant does not include the changes in electrical displacement due to the polarization, which was included explicitly in the model. Only polarization bound charge was considered in the model and any free charges were neglected in the calculation of the electrical energy. For the solution to the Poisson equation we assumed ideally compensating electrodes that fixed the potential at the top and bottom film surfaces, which were both assumed to be grounded. These electrodes were specified through the

boundary condition on the Poisson equation as explained in previous publications[181].

Stress and strain fields associated with spontaneous strains in the film due to the ferroelectric transition[183] were found by solving the equations for mechanical equilibrium, $\sigma_{ij,j} = 0$, with boundary conditions appropriate to thin films as described in previous publications[177,184]. For this simulation the electrostrictive constants in Voigt notation, Q_{ij}, leading to the spontaneous strain from the cubic parent phase were $Q_{11} = 0.032\ C^{-2}\ m^4$, $Q_{12} = -0.016\ C^{-2}\ m^4$ and $Q_{44} = 0.02\ C^{-2}\ m^4$. Similarly, the elastic constants used in the model were $C_{11} = 300.$ GPa, $C_{12} = 162$ GPa and $C_{44} = 69.1$ GPa[176]. These constants reflect the symmetry of the parent paraelectric phase[184].

The domain wall energy was incorporated into the model by adding an energy associated with gradients in the polarization. For simplicity, an isotropic domain wall energy was modeled with the expression

$$f_{DW} = \frac{1}{2} G P_{i,j}^2 \qquad \text{(Eq. 3.3)}$$

where G is the gradient energy coefficient that is related to the Landau coefficients and characteristic system length[177] of 1.0 nm. This constant was assumed to have a value of 1.1×10^{-10} C^{-2} m^4 N, which resulted in estimated domain wall energies in the model of about 110 mJ m^{-2}, 260 mJ m^{-2}, and 70 mJ m^{-2} for non-charged 71°, 109°, and 180° domain walls, respectively. These results are in reasonably good agreement with previous theoretical estimations based on density functional theory that have estimated the 71°, 109° and 180° domain wall energies ranging between 128 and 360 mJ m^{-2}, 33 and 205 mJ m^{-2}, and 98 and 829 mJ m^{-2} for the 71°, 109° and 180° domain wall energies, respectively[94,146,185].

The thin film was simulated on a quasi-two dimensional grid of $256\Delta \times 1\Delta \times$

80Δ where the grid spacing, Δ, was assumed to be 0.5 nm. Periodic boundary conditions were assumed in the first two dimensions, while non-periodic boundary conditions described above were assumed along the third, out-of plane dimension. A film thickness of 19 nm was used, with a 10 nm thick layer of substrate allowed to relax beneath the bottom of the film[177]. The remaining points were included as padding for numerical stability. In the $BiFeO_3/TbScO_3$ system lattice matching between the substrate and thin film results in only a small biaxial strain[89] and the phase field model reflected this by assuming that the biaxial coherency strain imposed by the substrate was 0.0%. This led to a system in which the substrate constrained the overlying thin film, but did not apply a compressive biaxial strain that may have led to a transition to the tetragonal phase in the thin film. The solution to the model was found by iteratively solving Eq. 3.1, where the temporal derivative was approximated with a finite difference with a time step of $t/t_0 = 0.01$.

3.3 Atomic-scale structure changes induced by charged domain walls

The domain structure of a 20 nm thick $BiFeO_3$ film grown on $TbScO_3$ substrate is shown in a cross-sectional dark-field TEM image (Fig. 3.1a). The domain configuration is depicted schematically below the TEM image, where the polarization orientations were confirmed by mapping $-\boldsymbol{D_{FB}}$ based on HAADF STEM images. As it has been shown that only r_1/r_4 ferroelastic structures exist in such films[89,102] and that specific domain walls are constrained within specific planes[95], it can be determined that the vertical boundaries are 109° domain walls and the inclined boundaries are 180° domain walls. Typically, the 180° domain walls appear paired with 109° ones to form triangular 109°/180° domain

wall junctions, located either at the $BiFeO_3/TbScO_3$ interface (Fig. 3.1b) or near the free surface (Fig. 3.1c). Surprisingly, the latter junctions are usually located below the surface and thus create 71° sCDWs with "head-to-head" polarization arrangements.

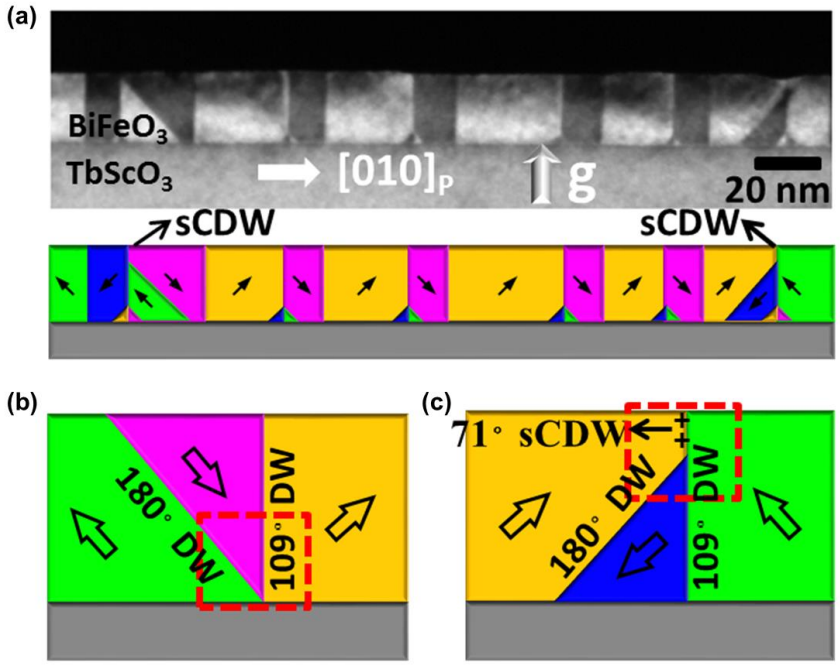

Fig. 3.1 Triangular 109°/180° domain wall junctions in a 20 nm $BiFeO_3$ thin film
(a) Cross-sectional dark-field TEM image showing the domain structure of a 20 nm thick $(001)_{PC}$ $BiFeO_3$ film on $(110)_O$ $TbScO_3$ substrate. A schematic of the corresponding domain configuration is shown below the TEM image. Schematic domain configurations of triangular 109°/180° domain wall junctions located **(b)** at the $BiFeO_3/TbScO_3$ interface without a sCDW and **(c)** near the free surface with a sCDW.

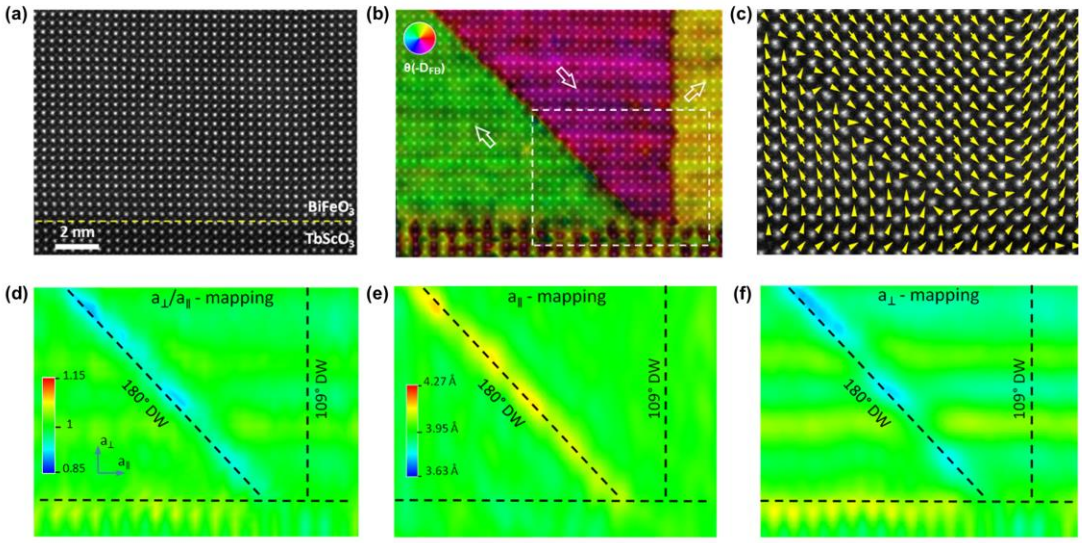

Fig. 3.2 Distribution of polarization and strain at a triangular domain wall junction at the $BiFeO_3/TbScO_3$ interface
(a) HAADF STEM image of a triangular 109°/180° domain wall junction at the $BiFeO_3/TbScO_3$ interface without a sCDW, similar to the highlighted region in Fig. 3.1(b), with the corresponding **(b)** color map of the direction of $-\boldsymbol{D_{FB}}$, and **(c)** the spatial distribution of the $-\boldsymbol{D_{FB}}$ vectors for the rectangular highlighted part in (b), and color maps of **(d)** the $a_\perp/a_\parallel$ ratio, **(e)** the in-plane lattice parameter $a_\parallel$, and **(f)** the out-of-plane lattice parameter $a_\perp$.

The atomic scale structure and polarization configuration at the 109°/180° domain wall junctions were examined by atomic-resolution HAADF STEM imaging. Fig. 3.2a shows a HAADF image of domain walls terminating at the $BiFeO_3/TbScO_3$ interface. A color map in Fig. 3.2b shows the direction distribution of $-\boldsymbol{D_{FB}}$. Fig. 3.2c shows the corresponding spatial distribution of the $-\boldsymbol{D_{FB}}$ vectors for the highlighted region in Fig. 3.2b. Fig. 3.2d shows the out-of-plane lattice parameter ($a_\perp$) / in-plane lattice parameter ($a_\parallel$) ratio $a_\perp/a_\parallel$ mapping of the HAADF STEM image shown in Fig. 3.2a, suggesting that the $a_\perp/a_\parallel$ ratio at the 180° domain walls is reduced compared with that of the bulk domain. This might be caused by the fact that domain walls in *R*-like $BiFeO_3$ tend to adopt an in-plane orientated polarization as an intermediate state[185,186]. In an inclined 180° domain wall, such polarization favors a lattice distortion with an increased in-plane lattice parameter and a reduced out-of-plane lattice parameter, as shown in Fig. 3.2e and

f, respectively. As the 109° domain wall is orientated vertically, however, the lattice distortion is forbidden by the clamping effect of the surrounding domains.

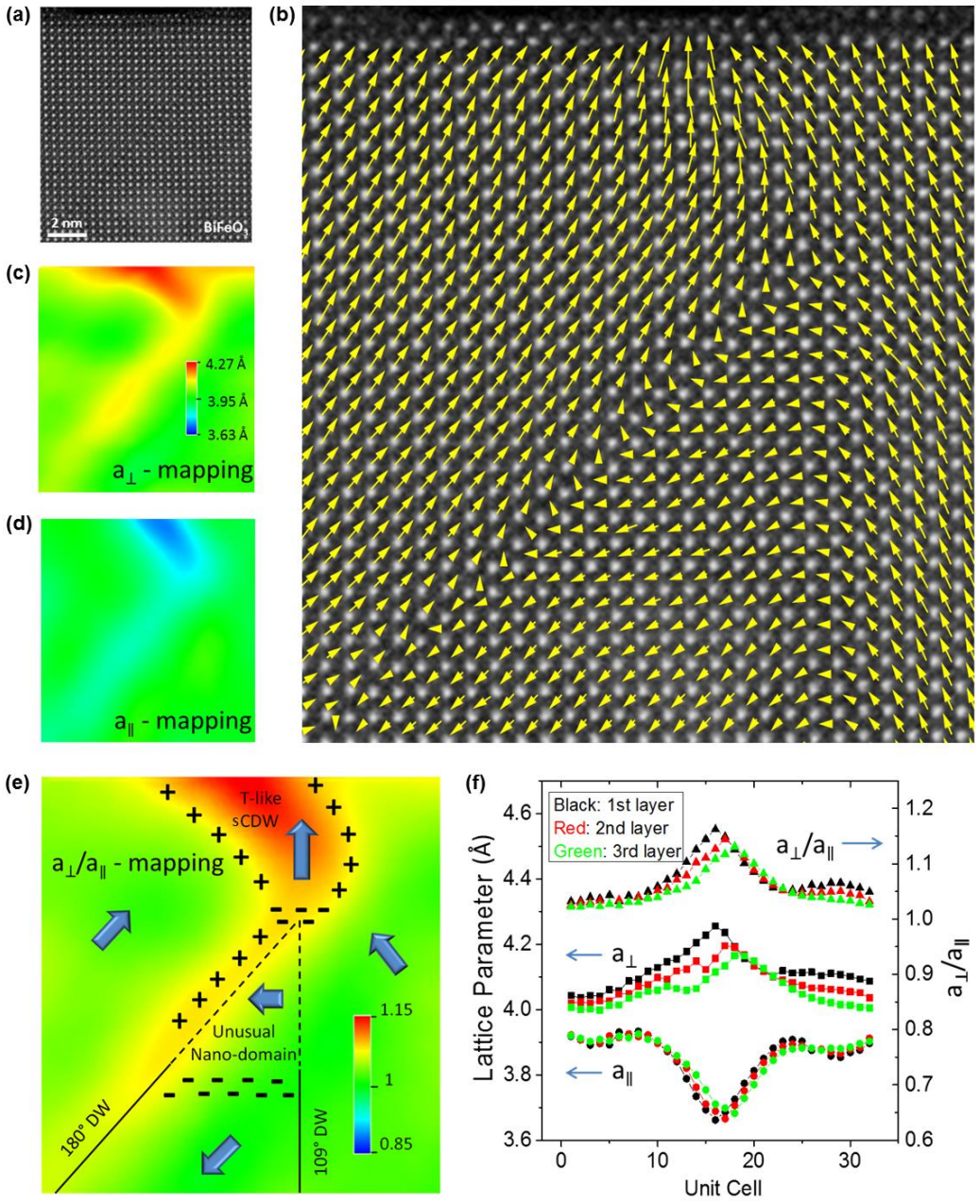

Fig. 3.3 Distribution of polarization and strain at a triangular domain wall junction near the free surface

(a) HAADF STEM image of the triangular 109°/180° domain wall junction associated with a sCDW near the free surface, similar to the highlighted region in Fig. 3.1(c), with the corresponding **(b)** spatial distribution of the $-\boldsymbol{D}_{FB}$ vectors and color maps of **(c)** the out-of-plane lattice parameter $a_{\perp}$, **(d)** the in-plane lattice parameter $a_{\parallel}$, and **(e)** the $a_{\perp}/a_{\parallel}$ ratio. The polarization orientation and bound charge are indicated schematically in (e), suggesting formation of a *T*-like sCDW and an unusual nano-domain. **(f)** The $a_{\perp}$, $a_{\parallel}$, and $a_{\perp}/a_{\parallel}$ changes across the sCDW in the first three lattice layers below the surface.

Fig. 3.3a shows a HAADF STEM image of a 109°/180° domain wall junction near the free surface of the same $BiFeO_3$ film. The spatial distribution of the $-\boldsymbol{D_{FB}}$ vectors is shown in Fig. 3.3b, revealing the formation of a sCDW above the junction of the 180° and 109° domain walls. It is clearly shown that this polarization configuration does not result in a direct "head-to-head" boundary. In fact, the polarization rotates gradually from the $<111>_{PC}$ direction in the domains on both sides to the out-of-plane direction at the sCDW. The crystal structure also changes gradually across the sCDW. Mapping of the lattice parameters (Fig. 3.3c-e) shows that a decrease of the in-plane lattice parameter and an increase of the out-of-plane lattice parameter result in a high $a_\perp/a_\parallel$ ratio (~1.15) in the vicinity of the sCDW. All these results suggest the formation of a localized *T*-like structure at the sCDW, while the surroundings remain in possession of *R*-like structure. Using the data from the top three lattice layers, the change of lattice parameters and $a_\perp/a_\parallel$ ratios across the sCDW is plotted in Fig. 3.3f, suggesting that the *R*-like to *T*-like then back to *R*-like structure transformation occurs over a distance of ~20 unit cells.

The formation of the *T*-like structure at the sCDW can reduce the electrostatic energy by avoiding the formation of the direct "head-to-head" polarization configuration at the sCDW. The coexistence of the *T*-like and *R*-like structures results in not only positive bound charge, but also compensating negative bound charge at the sCDW, releasing some of the electrostatic energy, as shown schematically in Fig. 3.3e. This is quite different from the well-known mixed *R*-*T* structures in strained $BiFeO_3$ thin films grown on $LaAlO_3$ substrates[50,51,53,96,97,187,188], where the driving force is the highly compressive epitaxial strain. Due to the different formation mechanism, the *R*-*T* mixed

structure observed here shows unique characteristics compared with that observed in the strained $BiFeO_3$ films grown on $LaAlO_3$. Firstly, the *R*-*T* structure mixing in the $BiFeO_3/LaAlO_3$ system is limited to films thicker than 50 nm since it depends on relaxation of the epitaxial misfit strain. In contrast, in $BiFeO_3$ films on $TbScO_3$ substrates the dimension of the mixed *R*-*T* region is much finer, with the *R*-like and *T*-like domains as small as several nanometers in width. Secondly, unlike the strain driven mixed phase, where the in-plane lattice parameter of $BiFeO_3$ is constrained by the substrate lattice parameter and only changes slightly between the two phases (less than 3%), a significant decrease of the in-plane lattice parameter is observed in the *T*-like structure at the sCDW, and the in-plane lattice parameters of the *T*-like structure at the sCDW and the neighboring *R*-like domains differ by ~8%.

The bound charge at the *T*-like sCDWs also affects the polarization configuration in the region below the domain wall junction. As shown in Fig. 3.3b and e, the tip region of the triangular domain below the sCDW is found to possess an unexpected ferroelectric state, as its $a_\perp/a_\parallel$ ratio is close to 1.00, but its polarization is suppressed in magnitude and has rotated from the $<111>_{PC}$ direction to the in-plane direction. This avoids a direct "tail-to-tail" configuration at the triangular tip and thus releases some of the electrostatic energy. Due to the unique polarization state of this nanoregion, the rotation angle of polarization across the domain walls formed with the neighboring domains is no longer 180° or 109°, although they do return to those angles in the region far below the *T*-like sCDW. The inclined wall (on the left side) of the triangular domain near the triangular tip becomes charged itself, adopting an out-of-plane polarization as an intermediate state with respect to the two nearby domains (Fig. 3.3b), and thus has an increased $a_\perp/a_\parallel$ ratio

(Fig. 3.3e), which is exactly opposite to that of the uncharged 180° domain wall shown in Fig. 3.2d. Moving down to the bottom interface, the polarization of the triangular domain returns to the $<111>_{PC}$ direction. As a result, the inclined 180° domain wall becomes neutral with a smaller $a_{\perp}/a_{\parallel}$ ratio.

For sufficiently thin films, an increased *T*/*R* ratio and sCDWs traversing the full thickness of the film can be achieved. Arrays of charged and uncharged junctions of 180° and 109° domain walls were found in 5 nm thick $BiFeO_3$ films grown on $TbScO_3$ substrates (Fig. 3.4a). The formation of the T-like sCDW is also demonstrated in the atomic-resolution HAADF STEM image (Fig. 3.4b) and the corresponding spatial distribution of the $-\boldsymbol{D_{FB}}$ and $a_{\perp}/a_{\parallel}$ ratio mappings in Fig. 3.4c and 3.4d, respectively. As the triangular domain is much smaller in the 5 nm thick film, the whole triangular domain adopts a suppressed in-plane polarization, and the entire domain walls become unconventional, like those near the tip of the triangular domain in the 20 nm film, since the electrostatic driven force for these two regions is similar. Due to the effect of charges, the *T*-like sCDWs and the unconventional sCDWs of the unusual triangular domains can provide conducting channels running through the whole ferroelectric film.

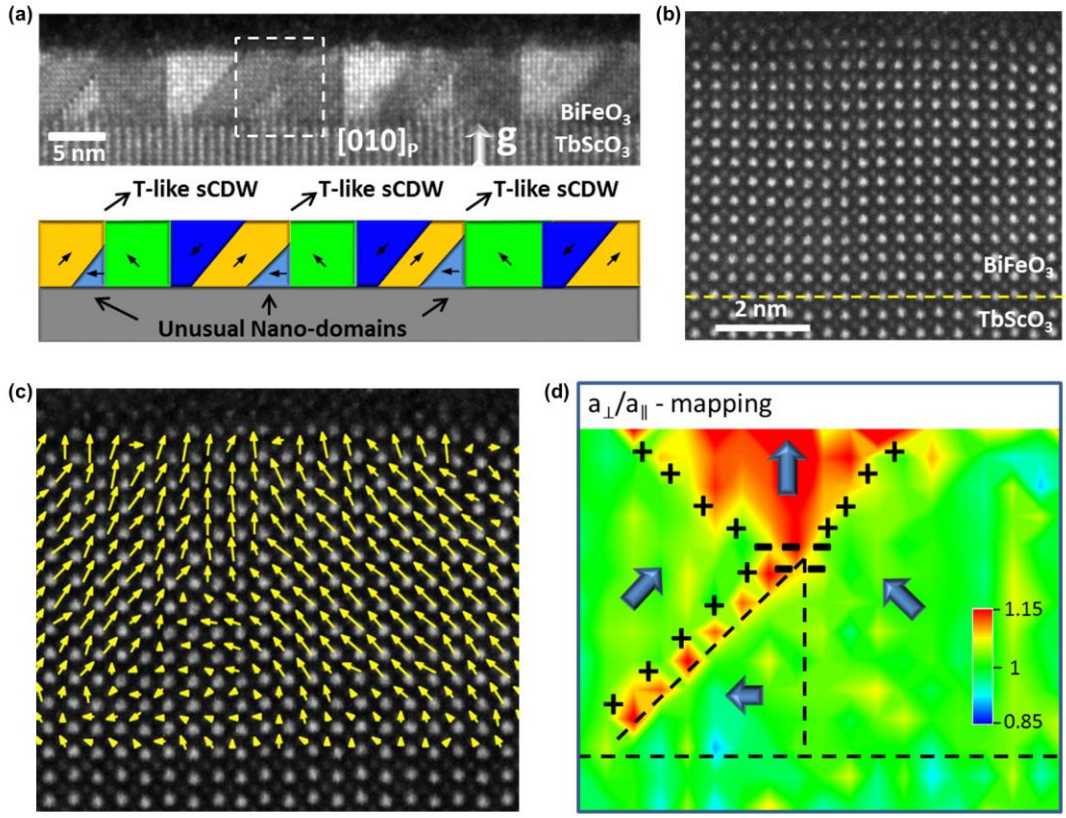

Fig. 3.4 Triangular domains and sCDWs in a 5 nm $BiFeO_3$ thin film
(a) Cross-sectional dark-field TEM image revealing the domain patterns of a 5 nm thick $(001)_{PC}$ $BiFeO_3$ film on a $(110)_O$ $TbScO_3$ substrate. Arrays of *T*-like sCDWs and unusual nano-domains are evident. **(b)** HAADF STEM image of the rectangular highlighted part in (a), and the corresponding **(c)** spatial distribution of the $-\boldsymbol{D_{FB}}$ vectors and **(d)** color map of the $a_\perp/a_\parallel$ ratio. The polarization orientation and bound charge are indicated schematically in (d), suggesting a conductive sCDW channel can form traversing the $BiFeO_3$ film.

Although the formation of a *T*-like structure at the sCDW can provide self-compensating bound charges, the energy of such a sCDW should still be higher than uncharged domain boundaries. The energetic driving force for the formation of the sCDW must be further considered. Whether the formation of a sCDW is favorable depends on the minimization of the total domain wall energy: $E_{total} = E_{109} \cdot S_{109} + E_{180} \cdot S_{180} + E_{sCDW} \cdot S_{sCDW}$, where E_{109}, E_{180}, E_{sCDW}, S_{109}, S_{180}, and S_{sCDW} are the energies per unit area and domain wall area of the 109° and 180° domain walls and the charged 71° domain wall (Fig. 3.1c), respectively. When two 180° and 109° domain walls

intersect with a junction below the free surface, adsorbed ions could provide free charge, compensating some of the bound charge at the sCDW[89,189]. This results in a lowered E_{sCDW}, comparable in energy to E_{109} and E_{180}[172,190]. The system will thus favor the formation of a sCDW to decrease E_{total} by decreasing both S_{109} and S_{180}. When a sCDW extends deeply in the $BiFeO_3$ film, however, E_{sCDW} increases greatly as the free surface can no longer compensate the bound charge. As a result, sCDWs are restricted to the near-surface region.

3.4 Giant resistive switching via control of charged domain walls

A sCDW can also be stabilized near the bottom interface of a $BiFeO_3$ thin film when there is a bottom electrode, since the bound charge of the sCDW can then be screened by free charge carriers from the electrode. By applying a bias between such bottom electrode and a tungsten surface probe, the sCDW can be reversibly switched (Fig. 3.5a). A cross-sectional dark-field TEM image of a system with a stable sCDW in a $BiFeO_3$ thin film grown on $TbScO_3$ substrate with a $La_{0.7}Sr_{0.3}MnO_3$ bottom electrode is shown in Fig. 3.5b. The polarization configuration was determined through mapping - $\boldsymbol{D_{FB}}$ vectors using HAADF STEM imaging[158], as shown in Fig. 3.5d-g. As the tip of the triangular domain is located above the $BiFeO_3/La_{0.7}Sr_{0.3}MnO_3$ interface, a 71° sCDW with "head-to-head" polarization is created there. Similar to the phenomena observed at the sCDW just below top surface, the polarization at the sCDW above the $BiFeO_3/La_{0.7}Sr_{0.3}MnO_3$ interface has also rotated into the out-of-plane direction (Fig. 3.5g), forming a local *T*-like structure; and the bulk domains remain to be *R*-like, with polarization pointing along the body diagonal of the $BiFeO_3$ lattice (Fig. 3.5d-f). This

structural change is also reproduced by phase-field simulation of the sCDW configuration (Fig. 3.5h). On the other hand, the system can also be stable without a sCDW as shown in the TEM image (Fig. 3.5c) and the corresponding simulated result (Fig. 3.5i), where the 109° and 180° domain walls are separated by sufficient distance so that their interaction is weak. From these two sets of observations and simulations we conclude that the system is bistable and can exist either with or without a sCDW.

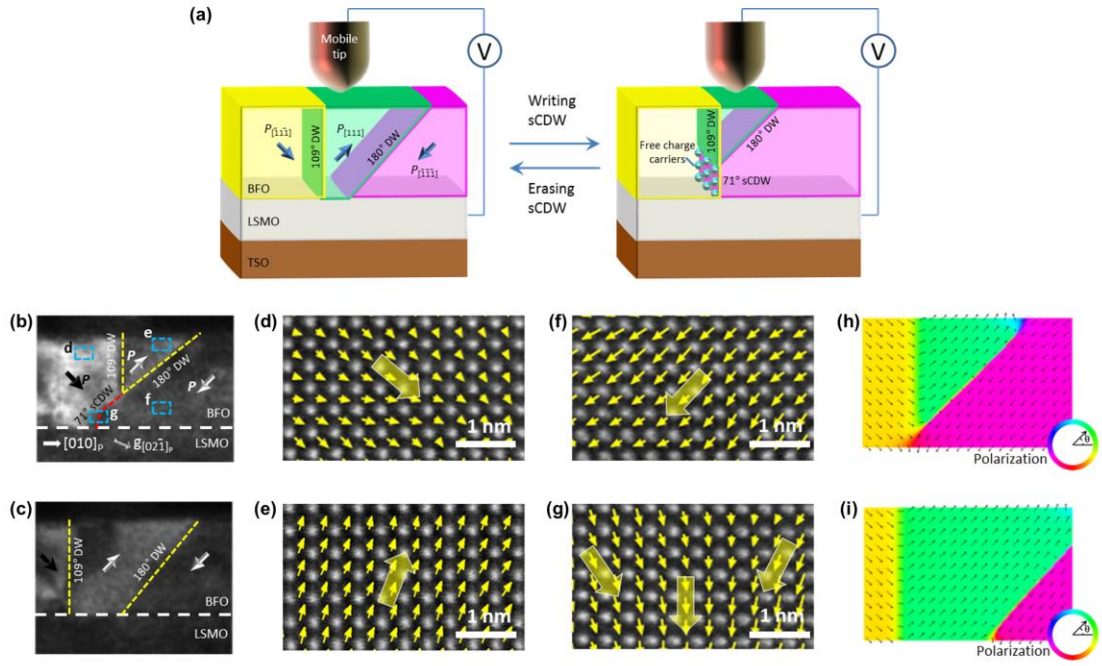

Fig. 3.5 Bistability of the system associated with a sCDW in a $BiFeO_3$ thin film
(a) Schematic of experimental set-up: a $BiFeO_3$ (BFO) thin film was grown on $La_{0.7}Sr_{0.3}MnO_3/TbScO_3$ (LSMO/TSO), and a mobile tungsten tip acts as one electrode for electrical switching with the LSMO layer being grounded. Through the application of electrical bias, sCDW can be wrote and erased in the BFO film. **(b)** Cross-sectional dark-field TEM image showing a triangular 109°/180° domain wall (DW) junction with a 71° sCDW. **(c)** TEM image showing domain configuration of separated 109° and 180° domain walls, without a sCDW. Note that ***P*** denotes polarization directions in the domains. For scale, the BFO film thickness in (b) and (c) is 20 nm. **(d-g)** Atomic-resolution HAADF STEM image of four different regions highlighted by the rectangles in (b)**.** Vectors indicate the polarization direction across these regions described. **(h)** Phase field simulation of polarization distribution of the stable domain structure with a sCDW in BFO film. **(i)** Simulated polarization distribution of the stable domain structure of the system without a sCDW. The arrows mark the polarization orientations. For scale, the BFO film thickness in (h) and (i) is 19 nm.

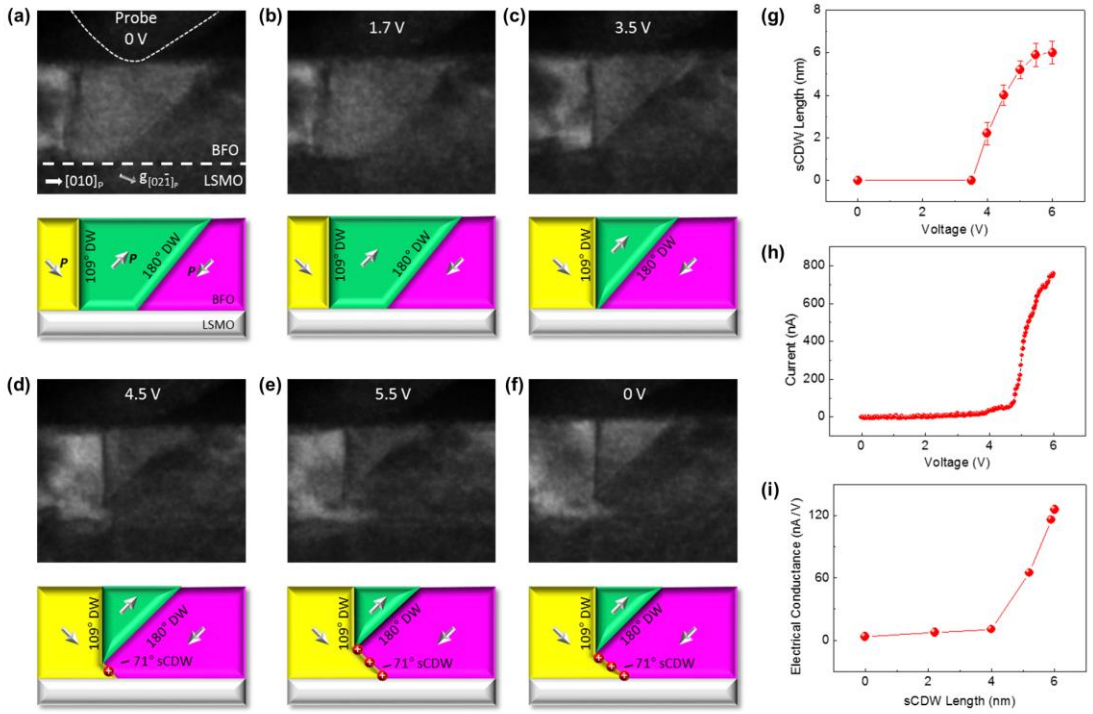

Fig. 3.6 Creation of a sCDW caused by applying a positive ramp bias using *in situ* TEM
(a) The original stable state without a sCDW in $BiFeO_3$ (BFO) film. **(b)** At the critical bias, the domain wall (DW) started to move. **(c)** The 109° and 180° domain walls intersect at the substrate interface as a result of domain wall motion. **(d,e)** Formation and growth of a sCDW as a result of upward motion of the tip of the triangular 180°/109° domain wall junction. **(f)** After removal of the bias, the sCDW relaxed to be shorter than that observed in (e). For scale, the BFO film thickness is 20 nm. **(g)** The measured length of the sCDW as function of the applied voltage. **(h)** *In situ* measured current during the creation of the sCDW. **(i)** The measured local electrical conductance of the film as function of the sCDW length.

A sCDW can be created by applying a bias, as shown in the chronological series of images presented in Fig. 3.6a-f. The bias was linearly increased from 0 to 6.0 V over 50 seconds. The initial stable structure (Fig. 3.6a) contained 109° and 180° domain walls separated by 10 nm at the substrate interface. The onset of domain wall motion occurred at a critical applied bias of 1.7 V (Fig. 3.6b). As larger biases were applied, a two-stage switching process occurred. During the first stage, the two 109° and 180° domain walls moved toward each other until they intersected (Fig. 3.6c). During the second stage, further shrinkage of the triangular domain led to upward motion of the triangular domain

tip and resulted in the formation and elongation of a sCDW (Fig. 3.6d,e). The measured length of the sCDW, which is defined as the distance from the triangular domain tip to the $BiFeO_3/La_{0.7}Sr_{0.3}MnO_3$ interface, is plotted as function of applied voltage (Fig. 3.6g). After the bias was removed, the system relaxed to a stable state and the length of the sCDW remained ~5 nm (Fig. 3.6f).

By measuring the *in situ* current during the switching process (Fig. 3.6h), we are able to correlate the domain wall configuration and film conductivity in real time. When the applied voltage is lower than 3.5 V, the film showed almost no conductivity (current < 10 nA, which is approaching the resolution limit of the *in situ* apparatus), corresponding to domain configurations without a sCDW (Fig. 3.6a-c). When the voltage reaches 4.5 V, the film showed little conductivity (current ~ 50 nA), corresponding to domain configurations with only a relatively short sCDW (length ~ 4nm). However, further increasing the bias caused the sCDW to elongate, leading to dramatically increased conductivity measurements. Significant conduction with strongly enhanced currents of 640 to 760 nA occurred at voltages higher than 5.5 V. The resistive switching also shows good repeatability at multiple spots where the same type of sCDW exists (Fig. 3.7) and is absent during the switching process at local monodomain regions without a sCDW in the same film (Fig. 3.8). Previous studies have shown a resistive switching in ferroelectric films can occur via the effect of a switchable Schottky-to-Ohmic interfacial contact between the electrode and the semiconducting ferroelectric film, and the switching occurs as the sign of polarization bound charge at the interface is reversed.[35,63] In the local region where a sCDW is present in our system, during the resistive switching observed at 4.5 ~ 5.5 V (Fig. 3.6d and e), the top $BiFeO_3$/probe interface and the bottom

$BiFeO_3/La_{0.7}Sr_{0.3}MnO_3$ interface both have positive polarization bound charge and no change of the sign of the bound charge is observed, excluding a switching between the Schottky and Ohmic contacts at the interface. Since the positive bound charge would attract accumulated compensating electrons (free carriers in n-type $BiFeO_3$) and lead to downward band bending, both the interfaces of the local film with a sCDW would be Ohmic contacts[35,63]. Therefore, the conductivity of the system is primarily dependent on the bulk of the semiconducting $BiFeO_3$ film rather than the interfaces. Upon the elongation of the sCDW at 4.5 ~ 5.5 V (Fig. 3.6d and e), a very high charge state can be created at the local region, causing the observed significant change of the film conductivity. Combining the measured sCDW length (Fig. 3.6g) and *in situ* current (Fig. 3.6h) during the switching process, a direct correlation between the electrical conductance of the local film and the sCDW length can be made, as shown in Fig. 3.6i. This correlation shows a nonlinear relation and a substantial enhancement of film conductivity when the sCDW penetrates more than a critical value in length (~4 nm in this case).

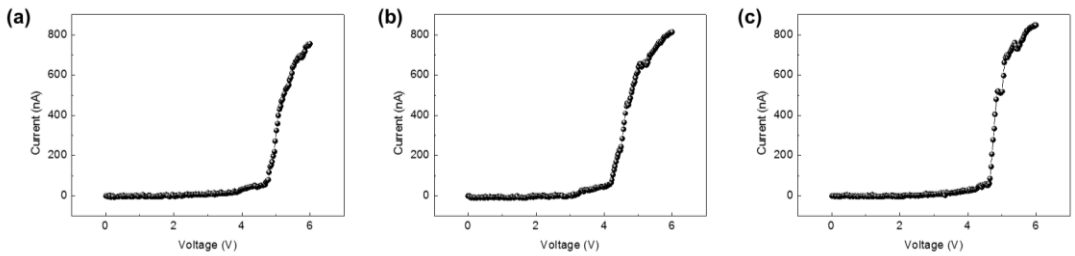

Fig. 3.7 Repeatability of the sCDW assisted resistive switching
(a-c) Three repetitive I-V curves showing the resistive switching measured in *in situ* TEM, at different spots of the same $BiFeO_3$ thin film where the same type of sCDW exists.

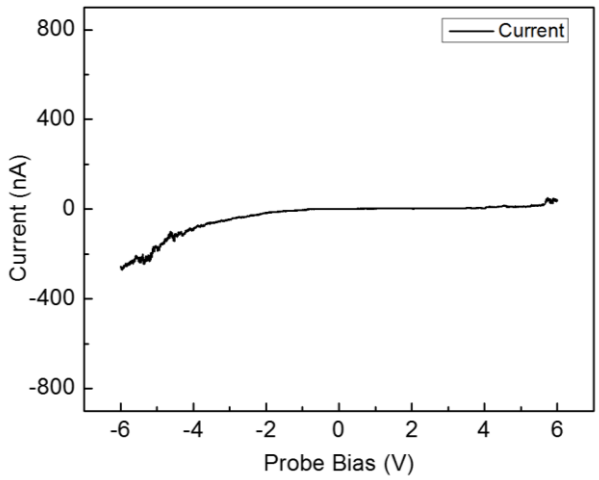

Fig. 3.8 Absence of resistive switching at a local region in the $BiFeO_3$ thin film without a sCDW I-V curve taken *in situ* by applying a bias between the tungsten surface probe and the buffer $La_{0.7}Sr_{0.3}MnO_3$ electrode in a region that is originally monodomain. For the positive branch, the polarization switching occurred at V = ~ 2.0 V. This switching did not cause any detectable current change.

To better understand the formation of the conductive state caused by the sCDW, phase-field modeling of the epitaxial $BiFeO_3$ thin film was employed (Fig. 3.9). Polarization distributions of three characteristic domain structures, shown in Fig. 3.9a-c, closely resemble the experimentally observed domain configurations shown in Fig. 3.6c-e. In this simulation, Fig. 3.9b, a small *T*-like sCDW above the bottom interface was found to be the most stable domain configuration. Domain structures starting from either closely spaced 109° and 180° domain walls in which no *T*-like sCDW exists (Fig. 3.9a) or from a large sCDW state (Fig. 3.9c) were allowed to relax towards the equilibrium configuration (Fig. 3.9b).

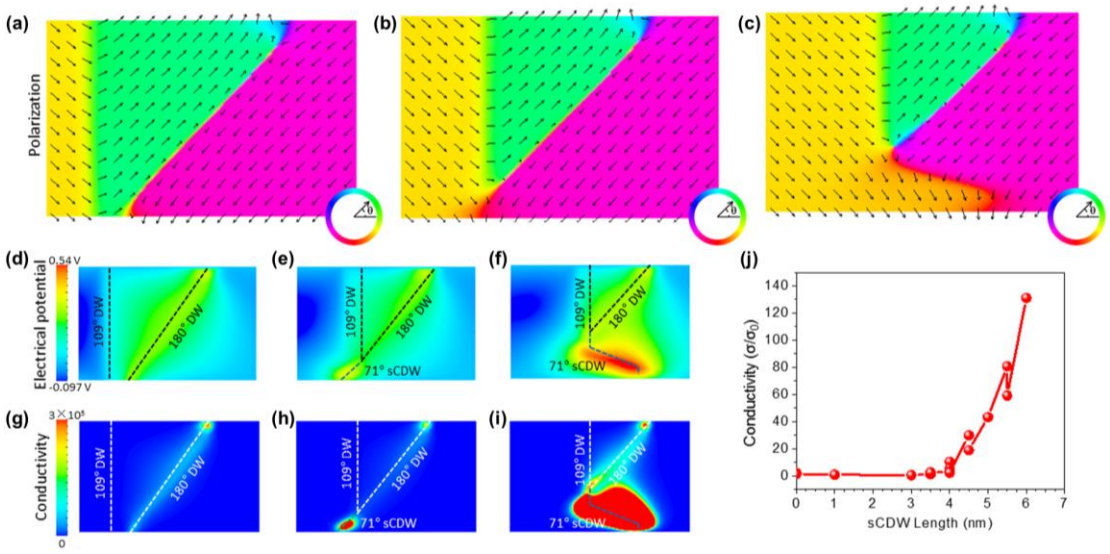

Fig. 3.9 Phase-field simulations of electrical state around a sCDW in the $BiFeO_3$ thin film Polarization distributions for metastable domain structures with **(a)** two closely spaced domain walls with no sCDW; **(b)** a small separation between the triangular domain and electrode with a limited sCDW; and **(c)** a larger sCDW resulting from a large separation between the triangular domain and electrode. The arrows mark the polarization orientations. **(d-f)** Electrical potential distribution calculated from the polarization bound charges in domain structures (a)-(c), respectively. **(g-i)** Normalized thin film conductivity around domain structures (a)-(c). **(j)** Total calculated normalized conductivity of the $BiFeO_3$ thin film around the domain structure for a series of charged domain wall lengths (defined as distances between the triangular domain tip and bottom electrode). For scale, the film thickness is 19 nm.

The corresponding calculated electrical potential distributions around the domain walls resulting from the polarization bound charge are shown in Fig. 3.9d-f. For the case of closely separated domain walls (Fig. 3.9a,d), the sharper change in the polarization at the nominally charge neutral 180° domain wall leads to a very small electrical potential there, as a result of the thin film boundary conditions. When the sCDW forms (Fig. 3.9b,e), the electrical potential at the boundary is increased due to the larger polarization bound charge. As the sCDW further elongates (Fig. 3.9c,f), the bound charge around the sCDW is significantly increased leading to a distributed area of high electrical potential in the thin film. Although the sCDW only penetrates less than half of the film thickness, enhanced potential is observed within a much broader region in the film, including a widened region along the inclined 180° domain wall. This observed enhanced potential

would attract free charge carriers at local areas, leading to enhanced conductivity not only at the sCDW but also along the 180° domain wall in the upper portion of the film above the sCDW. As a result, a significant increase of conductivity through the film is achieved by the creation of lower resistance paths through the film along the sCDW and 180° domain wall. These paths along the domain walls effectively act as short-circuit routes for flow of the electrical current.

We used the simulated electrical potential to calculate the expected relative electrical conductivity of the $BiFeO_3$ thin films around the sCDW. Since the defect chemistry of $BiFeO_3$ is poorly understood, it is difficult to predict the major charge carriers. Previous studies, however, have shown that conductivity at CDWs is typically strongest at "head-to-head" domain walls with positive bound charge, suggesting that, in some films at least, negative charge carriers dominate conduction[72]. Following this assumption, we estimate the negative charge carrier density around the domain walls using Boltzmann statistics and assume the density of positive charge carriers to be negligibly small. The local conductivity is then estimated as

$$\sigma = \sigma_0 \exp\left(-\frac{e\varphi}{k_b T}\right) \quad \text{(Eq. 3.4)}$$

and

$$\sigma_0 = N_0 e\mu \quad \text{(Eq. 3.5)}$$

where e is the charge on an electron, φ is the electrical potential, k_b is Boltzmann's constant, T is the absolute temperature, N_0 is the background carrier density and μ is the carrier mobility. The calculated normalized local conductivities are shown in Fig. 3.9g-i. These results show the sCDW is expected to have very large conductivity. This arises from the high carrier concentrations, which can be 10^6 times larger than the background

carrier concentration.

The total estimated conductivity through the film around the sCDW and the triangular domain structure was calculated by summing the contributions from all the individual grid points in the simulated film (from the top surface to the bottom interface), as plotted in Fig. 3.9j. Here we calculated the relative conductivity of the film assuming the simulated film is placed in a capacitor arrangement with conducting electrodes covering the entire top and bottom of the film. Although this simulation approach estimates the total effect of the domain structure change on the conductivity of the film over a larger volume of the film rather than only under a local electrode, we only allow a change of the sCDW and the triangular domain structure and restrict all other domain structures to be constant during the simulation. Therefore, any calculated change of conductivity should be caused by the local switching of the sCDW. For this analysis it was assumed that the grid points in lines parallel to the substrate conducted in parallel (inverse resistances add) while grid lines along the thickness were in a serial configuration during conduction (resistances add). To find the total film conductivity we first summed each row of grid points that conducted in parallel and then summed the results, which conducted in series. While the order of this operation changed the magnitude of the expected conductivity, it had no effect on the trends in the normalized results. Total calculated normalized film conductivity as a function of the length of the sCDW, which is defined as the distance of the triangular domain tip from the bottom electrode, is plotted in Fig. 3.9j. Initially, the conductivity of the thin film is very small for small separations between the electrode and triangular domain tip, corresponding to limited formation of the sCDW. For larger sCDW, however, the conductivity is clearly

seen to increase rapidly, in good agreement with the experimental results shown in Fig. 3.6i.

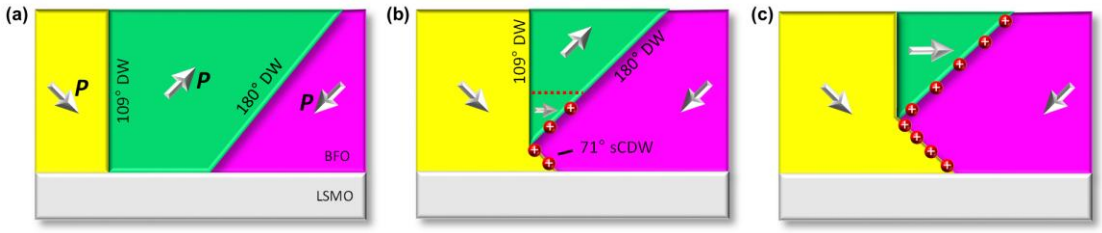

Fig. 3.10 Conductivity enhancing induced by polarization rotation during the sCDW switching **(a)** Domain structure without a sCDW. **(b)** Domain structure with a short sCDW below the triangular domain. The polarization at the tip region of the triangular domain has rotated into the in-plane orientation, and a charged segment has been stabilized on the inclined 180° domain wall. **(c)** Domain structure with a long sCDW below the triangular domain. Here, the polarization within the whole triangular domain has rotated into the in-plane direction. For scale, the film thickness is 20 nm.

In addition to the conductivity enhancing mechanism supported by the phase-field simulations, a possible dynamic process of polarization rotation within the triangular domain during the sCDW switching could further increase the conductivity of the local film, as demonstrated by the schematics in Fig. 3.10. In the initial stable structure without a sCDW (Fig. 3.10a), the nominally charge neutral 109° and 180° domain walls should lead to regular *R*-like polarization structures in the triangular domain. When the sCDW forms (Fig. 3.10b), however, the accumulated positive bound charge at the sCDW would cause the polarization at the tip region of the triangular domain to rotate into in-plane orientations, stabilizing a charged segment on the inclined 180° domain wall (see Fig. 3.3, 3.4 and the corresponding discussion for details). As the sCDW further elongates (Fig. 3.10c), such polarization rotation phenomena could extend deep into the triangular domain and elongate the charged segment on the 180° domain wall. This could further increase the electrical potential at the domain wall, and thus enhance the conductivity at the local film.

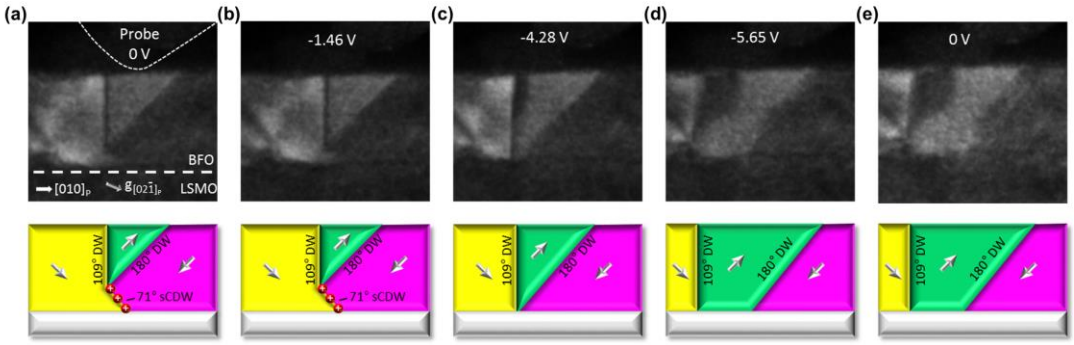

Fig. 3.11 Erasure of a sCDW caused by a negative ramp bias using *in situ* TEM
(a) The original stable state with a sCDW. **(b)** At the critical bias, the domain wall started to move. **(c)** The sCDW was annihilated as a result of the expansion of the triangular domain. **(d)** The system went back to the state without a sCDW. **(e)** After removal of the bias, this state remained stable. For scale, the film thickness is 20 nm.

The sCDW can also be erased by reversing the applied voltage (linearly decreasing it from 0 to -6.0 V over 50 seconds), as shown in Fig. 3.11. The critical bias to induce domain wall motion in this case (-1.46 V, as shown in Fig. 3.11b) was similar in magnitude to that in the sCDW writing process. Switching occurred by growth of the triangular domain (Fig. 3.11c), exactly reversing the domain shrinkage in the creation process. Finally, the system was returned to the original stable domain structure without a sCDW (Fig. 3.11d). This state remained stable after removal of the bias (Fig. 3.11e).

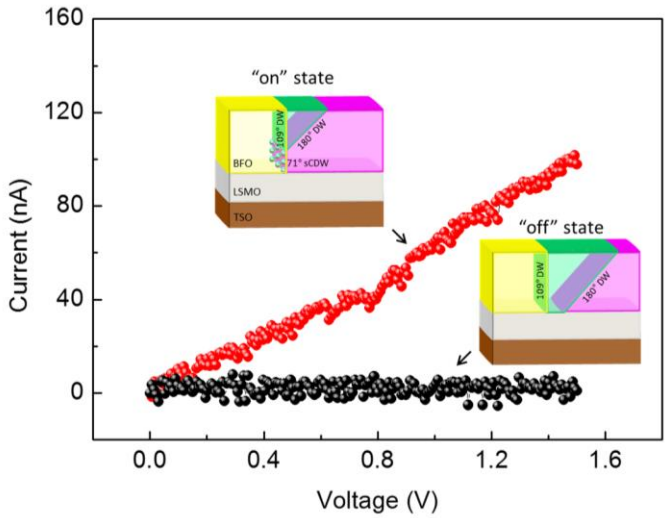

Fig. 3.12 Conductivity comparison of the "on" and "off" states in the $BiFeO_3$ thin film
In situ measured readout current of the system with ("on" state) and without ("off" state) a sCDW when applying a positive bias ramp from 0 to 1.5 V. The insets show schematic of the domain configurations of the "on" and "off" states. During the measurement, domain wall motion was not observed. Notice that no current except noise was detected for the "off" state.

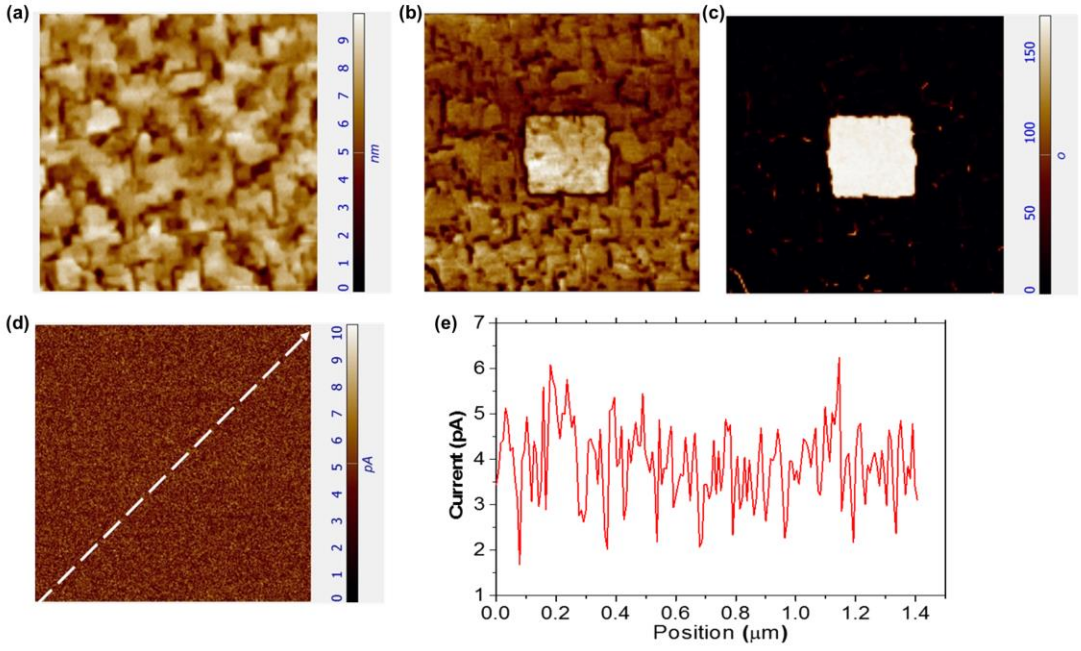

Fig. 3.13 Conductivity of bulk domains and uncharged domain walls in the $BiFeO_3$ thin film
(a) Topography, PFM **(b)** amplitude and **(c)** phase images of a square domain written with a tip bias of -5 V. **(d)** SSRM measurement at 1.5 V tip bias, showing that the current through bulk domains and uncharged domain walls is lower than several picoamperes. **(e)** Line profiles of SSRM current over the dashed line in (d). For scale, the size of the scanned region is 1um×1um.

The high stability and the large conductivity difference of the two states examined above, which are interconvertible through reversible switching of the sCDW, enables non-destructive resistive readout with a large off/on ratio. To demonstrate this we applied a "readout" bias sweep, linearly increasing from 0 to 1.5 V, and measured the readout currents for each of the two states (Fig. 3.12). This voltage is less than the critical voltage required to move the domain walls and does not change the domain structure of the $BiFeO_3$ thin film. The readout I-V curve current for the "on" state with a sCDW shows an Ohmic behavior, further supporting the conclusion of Ohmic contacts at the both interfaces of the local film where a sCDW is present. While readout current for the "on" state reached up to ~100 nA at V = 1.50 V, the readout current for the "off" state without a sCDW appeared to be effectively zero, as any current was less than the noise level (several nanoamperes) of the *in situ* apparatus. As the "off" state mainly conducts through bulk electrical transport and uncharged domain walls, its readout currents can be estimated by using scanning spreading resistance microscopy (SSRM) with better current resolution. The measured currents of uncharged domain walls and bulk domains in the same film between a surface probe and the $La_{0.7}Sr_{0.3}MnO_3$ bottom electrode are lower than a few picroamperes (Fig. 3.13), consistent with previously published results for $BiFeO_3$ thin films[64,65,68]. Consequently, the off/on ratio of the switchable resistivity in the system is determined to be about 10^5.

In conclusion, a local structure transition at nanoscale strongly charged domain walls (sCDWs), and a reversible switching of the sCDW, have been demonstrated in ferroelectric $BiFeO_3$ thin films. Since the "head-to-head" sCDW in *R*-like $BiFeO_3$ thin films observed here possess a *T*-like structure, the process of creating or erasing a sCDW

in the film would involve a dynamic transition between different lattice symmetries induced by an applied electric field. Significant resistive switching is observed at the local film as the length of the sCDW surpasses a critical value. The pronounced conductivity produced by the sCDW is several orders of magnitude higher than those of previously reported uncharged[64-68] or charged[71,72] domain walls. The resistive change enabled by the sCDW switching presents a much higher off/on ratio for the non-destructive readout than ferroelectric memories of other types, including ferroelectric tunneling junctions[37,39,40] and switchable ferroelectric diodes[33,35]. Using this effect, ultrahigh-density information storage based on sCDWs may be possible, as arrays of sCDWs with a spacing of 10 nm in films can already be produced, as shown by Fig. 3.4.

CHAPTER 4

Effect of Impurity Defects on Polarization Structures

4.1 Background

Nanoscale impurity defects, with structures different from host materials, are known to commonly exist in functional oxides as a result of slight stoichiometry fluctuations that occur during material growth. Local perturbations induced by these defects, such as charge, strain, and atomic interaction, could have a profound effect on the physical properties of oxides nanomaterials. A direct correlation of the defects to the material functionalities, however, is often hampered by the lack of a fundamental understanding of the microscopic mechanisms underlying the coupling between the defects and the host lattice. This is partially due to the difficulty of detecting the nanoscale defective structures buried in the bulk materials through conventional approaches such as X-ray diffraction and scanning probe microscopies. Here, using atomic-resolution STEM, atomically-thin impurity defects in $BiFeO_3$ thin films are directly resolved. In a combination of EELS, density-functional theory (DFT) and phase-field simulations, the effects of these impurity defects on ferroelectric properties of the thin films are explored. The results show that these defects can not only induce polarization enhancement and mixed-phase structures, but also create novel polarization states.

4.2 Experimental and theoretical methods

Film growth and TEM experiments: $BiFeO_3$ films on $TbScO_3$ substrates were grown by the same molecular-beam epitaxy method described in ref. 89. TEM specimen preparation and TEM imaging in different modes, including diffraction-contrast imaging, atomic-resolution HAADF STEM imaging, and *in situ* TEM, were performed using the same methods and the same instruments as those described in Chapter 3.2.

EELS experiments: STEM EELS experiments were performed with 300 kV electron beams and the convergence angle of ~22 mrad. The collection angle and energy dispersion for EELS acquisitions were 36 mrad and 1 eV/channel, respectively. For each pixel, a dwell time of 0.1 s was used to acquire the spectra. During the acquisition, both the zero-loss peaks and the core-loss spectra were recorded simultaneously in Dual-EELS mode. The post-processing of the spectra, *i.e.* alignment of spectra by zero-loss peaks and removal of the backgrounds in core-loss spectra, was carried out in the software package Digital-Micrograph.

DFT calculations: DFT calculations were carried out to study the interaction between surface defects and ultrathin $BiFeO_3$ films, using Vienna Ab-initio Software Package (VASP)[191] within the framework of PAW[192] and LSDA+U[193]. A symmetrical slab consisting of 5 $BiFeO_3$ lattice layers was built on top of 6 layers of $TbScO_3$ $(1\bar{1}0)_O$. The supercell was chosen to be $(\sqrt{2} * \sqrt{2})$ of the pseudocubic unit cell and the in-plane lattice constant was fixed to the experimental value of $TbScO_3$ (a=5.47 Å, b=5.73 Å). The k-points were sampled using a 5×5×1 Monkhorst-Pack mesh[194], with the plane-wave cut-off energy set to 500 eV and U and J parameters were chosen as $U_{eff} = U - J = 2$ eV[195]. To avoid spurious electric fields due to the slab configuration, a 15 Å vacuum

region was used to separate the periodic slabs, and the dipole correction was turned on during the calculation. A larger vacuum separation of 20 Å was tested as well and the total energy difference was only ~1 meV. The system is first relaxed by a force criterion (< 0.005 eV/Å), which reproduces the rhombohedral ferroelectric phase and *G*-type antiferromagnetic ground state of $BiFeO_3$. After the structure relaxation, a stoichiometric Bi_2O_3 monolayer defect was added on top of the relaxed $BiFeO_3$ slab and further relaxations were performed until the maximum force is <0.005 eV/Å. The relaxed structure is insulating. The Born effective charges (BEC) were calculated by finite difference of Berry-phase polarizations[196]. The calculated BECs are +4.56, +3.3 and -2.62 for Bi, Fe and O atoms, respectively.

Phase-field simulations: To simulate the domain structures stabilized by the surface defects, two sets of order parameters are considered, namely spontaneous polarization P_i (i = 1, 2, 3) and spontaneous oxygen octahedral rotation θ_i (i =1, 2, 3). The evolution of order parameters is governed by the time-dependent Ginzburg-Landau (TDGL) equations:

$$\frac{\partial P_i(\vec{r},t)}{\partial t} = -L_1 \frac{\delta F}{\delta P_i(\vec{r},t)} \quad (i = 1, 2, 3) \qquad \text{(Eq. 4.1)}$$

$$\frac{\partial \theta_i(\vec{r},t)}{\partial t} = -L_2 \frac{\delta F}{\delta \theta_i(\vec{r},t)} \quad (i = 1, 2, 3) \qquad \text{(Eq. 4.2)}$$

where $\boldsymbol{r}$ is the spatial position vector, t is the evolution time step, L_1 and L_2 are the kinetic coefficients for polarization and octahedral rotation, respectively. F is the free energy of the system which is the volume integration of Landau, elastic, electric and gradient energy densities:

$$F = \int \left(f_{\text{Landau}} + f_{\text{elastic}} + f_{\text{electric}} + f_{\text{gradient}} \right) \mathrm{d}V \qquad \text{(Eq. 4.3)}$$

The bulk Landau energy density has the contribution from polarization and octahedral rotation, namely:

$$f_{\text{Landau}} = f_{\text{polarization}} + f_{\text{rotation}} \qquad \text{(Eq. 4.4)}$$

Detailed expressions of the energy density as well as method of solving the phase-field equations can be found in literatures[177,181], and all the parameters are taken from literatures[197,198]. A quasi-2D simulation with system size of $64\Delta x \times 4\Delta y \times 25\Delta z$ is performed. The grid spacing is chosen as 0.4 nm, *i.e.*, $\Delta x = \Delta y = \Delta z = 0.4$ nm. The system consists of 10 grids of substrate layer, 5 grids of $BiFeO_3$ and 10 grids of air from the bottom to the top along the thickness direction. Mixed electric boundary condition is used, where the dielectric displacement is zero at the bottom of the film and the electric potential is fixed at the film top. A bias of -1.3V is added at specific locations on top of the film to simulate the effective fields induced by the surface defects[199], whereas the bias at all the other top areas are fixed to zero to account for the charge compensation from air. Periodic boundary condition is assumed along the in-plane dimensions, while a superposition spectral method is used along the out-of-plane direction (film growth direction)[200].

To simulate the domain structures stabilized by the charged defects, only one set of order parameters is considered, *i.e.*, the spontaneous polarization P_i (i = 1, 2, 3). The evolution of the spatial polarization as a function of time is described by the time-dependent Ginzburg-Landau equation shown in Eq. 4.1 and 4.3. A 2D simulation in the x-z plane with a system size of 51.2 nm × 50 nm was performed, where the thicknesses of the substrate and the film was 8 nm and 40 nm, respectively. The elastic boundary

condition was chosen to be traction free on the top surface of the film, and zero displacement at the bottom substrate (bottom of the simulation region). Open circuit electric boundary condition was used, in which the electric displacement was fixed at 0 at the film/substrate interface and film surface. For most simulations, except for those shown in Fig. 4.12e,f, the initial condition is set to random noise; for the simulations in Fig. 4.12e,f, in order to study the interaction of the bulk domain wall and the charged defect, the initial condition included a 109˚ domain wall (Fig. 4.12e) or a 180˚ domain wall (Fig. 4.12f) terminated at the defect.

4.3 Defect induced polarization enhancement in ultrathin films

The integration of ferroelectric thin films into nanoscale devices has led to an upsurge of interest in enhancing the functional properties of ferroelectrics at reduced dimensions. This development, however, has been hindered by the long-standing issue concerning the inevitable suppression of ferroelectric polarization in the ultrathin films with a thickness of a few nanometers, due to the strong depolarization effect arising from the incomplete screening at a surface or interface[154-156]. Interestingly, recent experimental work has suggested that a reduction in size to a scale of a few nanometers can lead to the emergence of weak room-temperature ferroelectricity in an otherwise non-ferroelectric $SrTiO_3$ film, as a result of electrically induced alignment of polar nanoregions due to Sr vacancies[201]. Another study using atomistic simulations demonstrated a mechanism for producing an overall enhancement of ferroelectricity in ultrathin ferroelectric capacitors by controlling the chemical environments at the metal/oxide interfaces[202]. Nonetheless, direct experimental observation of increased polarization at reduced dimensions of

common ferroelectrics has not been deterministically identified. Here, for the first time, a significant enhancement of the out-of-plane polarization is observed in ultrathin (2 nm) $BiFeO_3$ films. Such enhanced polarization arises from a strong coupling between the ultrathin film and the single-atomic-layer impurity defects on its surface. It is also correlated to a novel undulating mixed-phase nanodomain structure that may be useful for electromechanical applications.

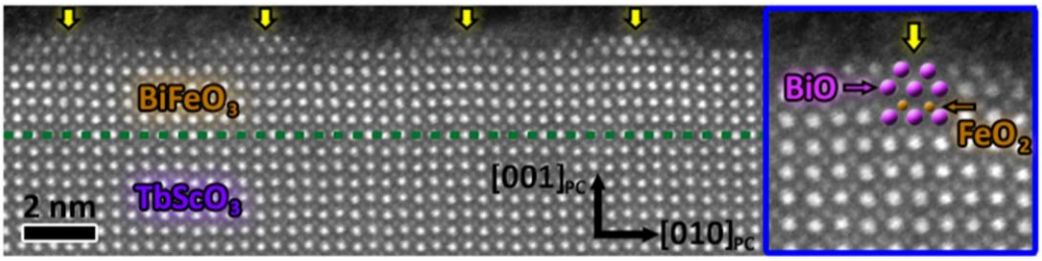

Fig. 4.1 Atomic structures of an ultrathin $BiFeO_3$ film
Cross-sectional HAADF STEM image of a 2 nm thick $BiFeO_3$ film grown on $TbScO_3$ viewed along the $[100]_{PC}$ zone axis, where the interface is indicated by the green dashed line. The yellow arrows indicate the unique monolayer defects on the surface, below which there are local lattice dilations along the out-of-plane direction. For a better view of the surface structure, see the inset for a magnified image.

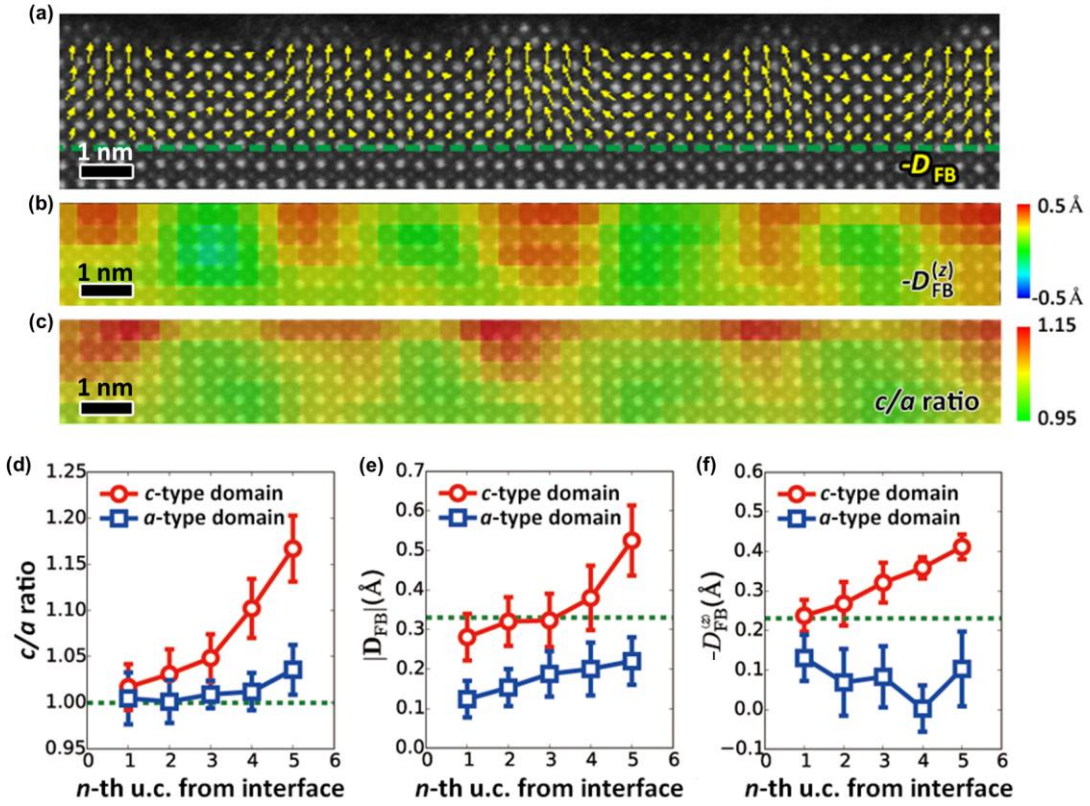

Fig. 4.2 Distribution of polarization and strain in the ultrathin $BiFeO_3$ film
HAADF STEM image of the ultrathin $BiFeO_3$ film overlaid with **(a)** $-\boldsymbol{D_{FB}}$ map, **(b)** $-\boldsymbol{D_{FB}}^{(z)}$ map, **(c)** *c*/*a* ratio map of the film, and plot of **(d)** *c*/*a* ratio, **(e)** $|\boldsymbol{D_{FB}}|$, and **(f)** $-\boldsymbol{D_{FB}}^{(z)}$ of the *c*-/*a*-type domains as a function of distance from the interface. The green dashed line in (a) mark the position of the $BiFeO_3$/$TbScO_3$ interface. The green dash lines in (d)-(f) indicate the *c*/*a* ratio, $|\boldsymbol{D_{FB}}|$ and $-\boldsymbol{D_{FB}}^{(z)}$ of bulk $BiFeO_3$, respectively.

Fig. 4.1 shows an atomic-resolution HAADF STEM image of a 2 nm $BiFeO_3$ film grown on $TbScO_3$ substrate, in which two remarkable structural features are present. First, the $BiFeO_3$ film is not homogeneous but characterized by a rumpled structure, with periodic out-of-plane lattice dilations at local regions indicated by the yellow arrows. Second, right above the film surface of each of these regions, there exist a monolayer impurity defect, which is several unit-cells in length along the $[010]_{PC}$ direction. These unusual structural features are also correlated to interesting domain patterns in the $BiFeO_3$ film, as evident by mapping the $-\boldsymbol{D_{FB}}$ vectors (Fig. 4.2a). Unlike the regular *R*-

like structure composed of 71°, 109°, or 180° domains in most other $BiFeO_3$ films grown on $TbScO_3$, the polarizations in this film are either very large in magnitude pointing in the out-of-plane $[001]_{PC}$ direction forming *T*-like "*c*-type" domains, or significantly attenuated with multiple directions forming "*a*-type" domains. And at the transition regions between the *c*-type and *a*-type domains, *R*-like structures with polarization pointing to the diagonal of the pseudocubic unit-cell can be observed. While the *c*-type domains are located right below the surface defects, the *a*-type domains exist at local regions without defects on the surface. This alternating *c*-/*a*-type domain structures can also be seen in the maps of the out-of-plane components of the $-\boldsymbol{D_{FB}}$ vectors ($-\boldsymbol{D_{FB}}^{(z)}$) (Fig. 4.2b) and the *c*/*a* ratios (Fig. 4.2c), where significantly enhanced out-of-plane polarizations and *c*/*a* ratios are observed in the *c*-type domains. By averaging the mapping data from each lattice layer within each individual domain type, the change of the *c*/*a* ratio, the magnitude of $-\boldsymbol{D_{FB}}$ ($|\boldsymbol{D_{FB}}|$), and $-\boldsymbol{D_{FB}}^{(z)}$ in the $BiFeO_3$ lattice can be plotted in Fig. 4.2d-f. In the *c*-type domain all these parameters increase substantially from the bottom interface to the top surfaces, whereas in the *a*-type domain they remain relatively constant with much smaller values.

The polarization value ($\boldsymbol{P_S}$) can also be estimated from the measured $-\boldsymbol{D_{FB}}$ parameters presented in Fig. 4.2e and f, based on an assumed linear relationship between the $\boldsymbol{P_S}$ and the $-\boldsymbol{D_{FB}}$ vectors[89]. Consequently, a giant polarization of ~136 μC/cm^2 is obtained at the top surface of *c*-type domains, and the out-of-plane polarization there is estimated to be ~109 μC/cm^2. In comparison, the estimated polarization of *a*-type domains is only about ~14-35 μC/cm^2 throughout the film. While the polarization suppression observed in the *a*-type domains is commonly expected in ultrathin

ferroelectric films due to the presence of a strong depolarization field, an anomalous polarization enhancement up to ~136 μC/cm^2 in the *c*-type domains is quite surprising. This value is even comparable to that of super-tetragonal $BiFeO_3$ films, in which a polarization up to ~150 μC/cm^2 is induced by a large compressive epitaxial strain[50]. The driving force of the as-observed enhanced polarization here, as well as the large lattice dilations, however, cannot be explained by the epitaxial strain applied by the substrate, since the lattice mismatch between $BiFeO_3$ and $TbScO_3$ is very small (< 0.14%). The one-to-one correspondence between the appearance of the *c*-type domains and the surface monolayer defects, on the other hand, may suggest a strong interaction between the polarization and the defects.

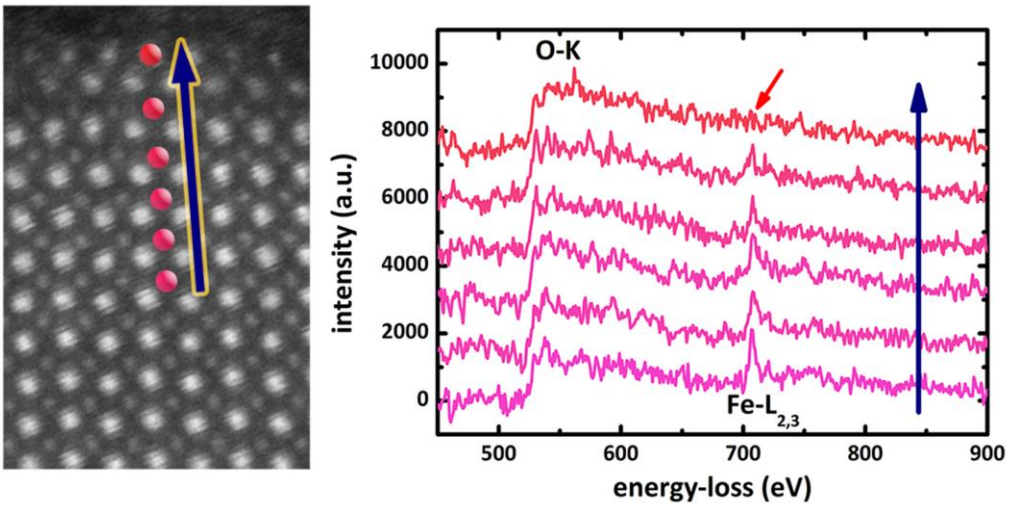

Fig. 4.3 Line scan profiles of Fe-$L_{2,3}$ and O-K energy-loss spectra in the ultrathin $BiFeO_3$ film **(a)** HAADF STEM image of the ultrathin $BiFeO_3$ film, on which the position of each point on the line scan is marked by the red circles, and **(b)** the corresponding EELS spectrum (from bottom to top). As indicated by the red arrow, the energy-loss peak of Fe-$L_{2,3}$ (~708 eV) vanishes at the surface layer, while that of O-K changes much less through the film.

In order to gain the chemical information of the defects, EELS line scans were carried out from the substrate to the surface. Six individual spectra, five for the $BiFeO_3$ film and one for the surface monolayer defect, are extracted from the line scan profile and

the processed spectra are displayed in Fig. 4.3. While the lower five spectra of the $BiFeO_3$ film all show the elemental O-K (~530 eV) and Fe-$L_{2,3}$ (~708 eV) energy-loss peaks, the surface defect is deficient in Fe. Meanwhile, the proportion of O changes much less. Direct evidence of Bi in the surface defect is difficult to be obtained straightforwardly from EELS due to its extremely high energy-loss (~2580 eV). But provided that there are no other elements introduced during the film growth and the HAADF image contrast of the surface defects is similar to that of the film, it is strongly inferred that the surface defect is primarily a compound of Bi and O atoms. The most probable candidate could be the nonstoichiometric Bi_2O_{3-x} (Fig. 4.4), since it has a small lattice mismatch (~2%) with $BiFeO_3$[203]. The formation of these surface defects is possibly due to certain surface reconstruction or relaxation processes[204,205], or through an outward migration of the lower BiO planes due to the volatility of Bi atoms.

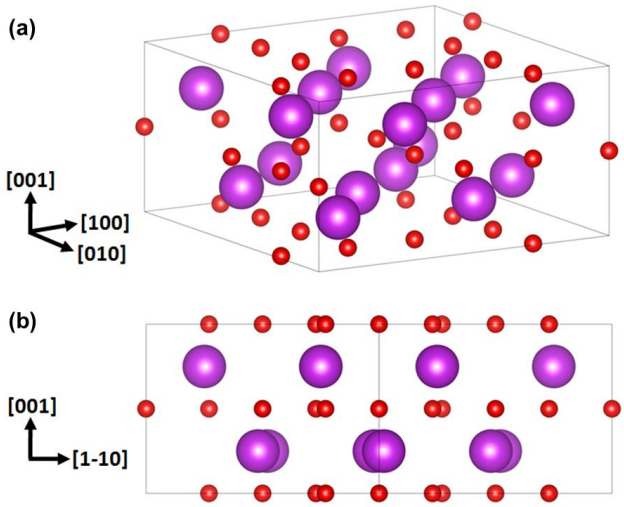

Fig. 4.4 Atomic structure of Bi_2O_3
(a) Atomic model of Bi_2O_3 and (**b**) its projection view along [110] direction.

The interaction of the defects and the ferroelectric polarization are explored by using DFT calculations, in which a single Bi_2O_3 layer was placed on top of a five-layer

$BiFeO_3$ ultrathin film. A full structural relaxation was performed in this system and in the relaxed structures a lattice dilation can be readily observed in the top $BiFeO_3$ layer (Fig. 4.5a). The measured *c*/*a* ratios and $|\boldsymbol{D_{FB}}|$ values of this simulated structure (Fig. 4.5b) match the experimental values very well. Local polarization can also be calculated from the simulated structure, based on the modern theory of polarization[196]:

$$\mathbf{P}_i = \frac{1}{\Omega_i}\sum_j Z^*_{i,j}\delta\mathbf{u}_{i,j} \qquad \text{(Eq. 4.5)}$$

where $\mathbf{P}_i$ and Ω_i are the polarization and the volume of unit cell i , respectively; and $Z^*_{i,j}$ and $\delta\mathbf{u}_{i,j}$ are the Born effective charge tensor and relative displacement of j-th atom, respectively. The calculated total polarization in each layer of the $BiFeO_3$ lattice and their in-plane and out-of-plane components are shown in Fig. 4.5c, in which the depicted trend of polarization increasing is in good agreement of the experimental observations in the *c*-type domain. And at the top Bi_2O_3/$BiFeO_3$ surface the values of the total polarization (~140 μC/cm^2) and its out-of-plane component (~86 μC/cm^2) also match the experimental results very well. The DFT simulation therefore concludes that the polarization enhancement in the ultrathin $BiFeO_3$ film should be induced by the surface defects.

Such strong interaction between the surface defects and the polarization can be attributed to the change of the ionic charge of the Bi atoms at the surface, as shown by the Bader charge analysis[206] (Table 4.1) of Bi and O atoms for the simulated structure. These results show that, although the ionic charge of Bi in $BiFeO_3$ is +1.87 (close to the +2 oxidation state), its value at the $BiFeO_3$/Bi_2O_3 interface reduces to +1.64 and in Bi_2O_3 layer it is only +1.27. The lower ionic charge of Bi atoms in Bi_2O_3 weakens the attraction between Bi and O atoms and increases their bond length. Consequently, the imbalance

between the weaker Bi-O bonds in the vicinity of the surface defects and the stronger ones in the underlying $BiFeO_3$ layers leads a strong effective field pointing to the surface, which counteracts the depolarizing field and causes the enhancement in polarization.

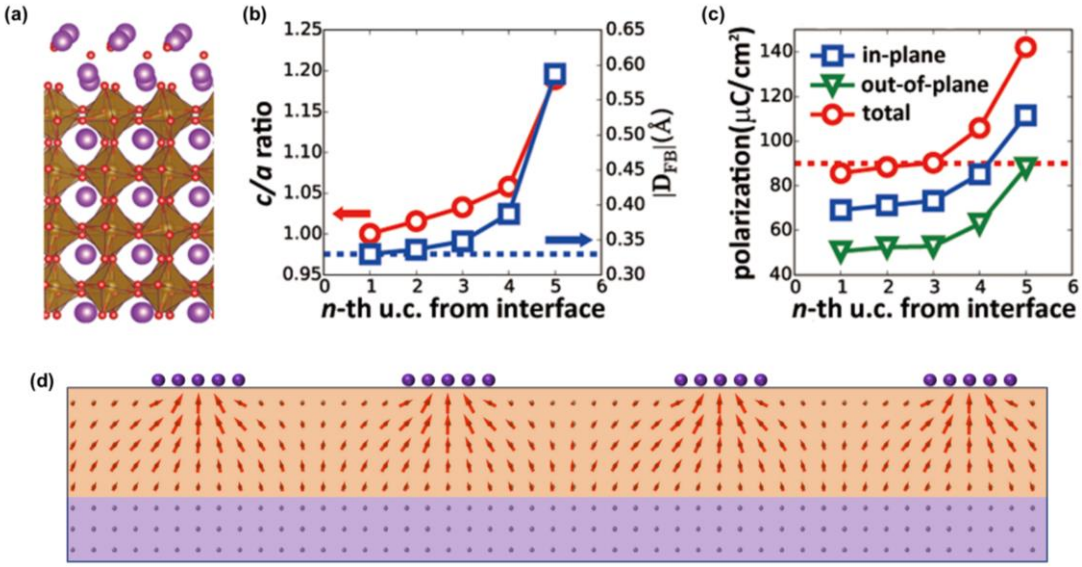

Fig. 4.5 Simulations of the interaction between the surface defects and the ultrathin $BiFeO_3$ film **(a)** DFT simulated atomic structure after structural relaxation, and the corresponding **(b)** *c*/*a* ratio and $|\boldsymbol{D_{FB}}|$, and **(c)** ferroelectric polarization measured in this structure. The blue and red dash lines indicate $|\boldsymbol{D_{FB}}|$ and total polarization of bulk $BiFeO_3$, respectively. **(d)** Phase field simulation of polarization structures in the ultrathin film stabilized by the surface defects. The arrows show the polarizations. The purple circles mark the positions of the surface defects. The red and purple background color represent the $BiFeO_3$ film and the $TbScO_3$ substrate, respectively. For scale, the film thickness is 2 nm.

	Bi	Fe	O
surface Bi_2O_3 layer	+1.27	-	-1.14
1st BiO layer	+1.64	-	-1.16
1st FeO_2 layer	-	+2.72	-1.18
2nd BiO layer	+1.87	-	-1.20
2nd FeO_2 layer	-	+2.70	-1.19
3rd BiO layer	+1.87	-	-1.19
3rd FeO_2 layer	-	+2.70	-1.19
4th BiO layer	+1.87	-	-1.19
4th FeO_2 layer	-	+2.70	-1.19
5th BiO layer	+1.87	-	-1.19
5th FeO_2 layer	-	+2.70	-1.19

Table 4.1 Bader charge analysis results of the $BiFeO_3$ film and the surface Bi_2O_3
The Bi and O atoms at the surface have relatively lower oxidation state, while the oxidation state of Fe atoms is less affected. Into $BiFeO_3$ film, the Bader charge of Bi, Fe and O atoms quickly converges to their bulk values.

The domain formation mechanism in the ultrathin $BiFeO_3$ film was further studied by incorporating the effective fields induced by the surface defects into the phase-field simulation. In this simulation an effective built-in potential of -1.3V[199] is applied on the local surface where there should be a defect, whereas the potential at other surface areas are fixed to zero to account for the charge compensation from air. The simulated domain pattern (Fig. 4.5d) generally reproduces the experimental observation of the undulating *c*-/*a*-type domains with mixed-phase structures, where the polarization below the surface defects is *T*-like, the polarization at the local regions without surface defects is attenuated, and the polarization at the transition regions is *R*-like. These results therefore confirm that the surface defects can stabilize the underlying *c*-/*a*-type domain structures.

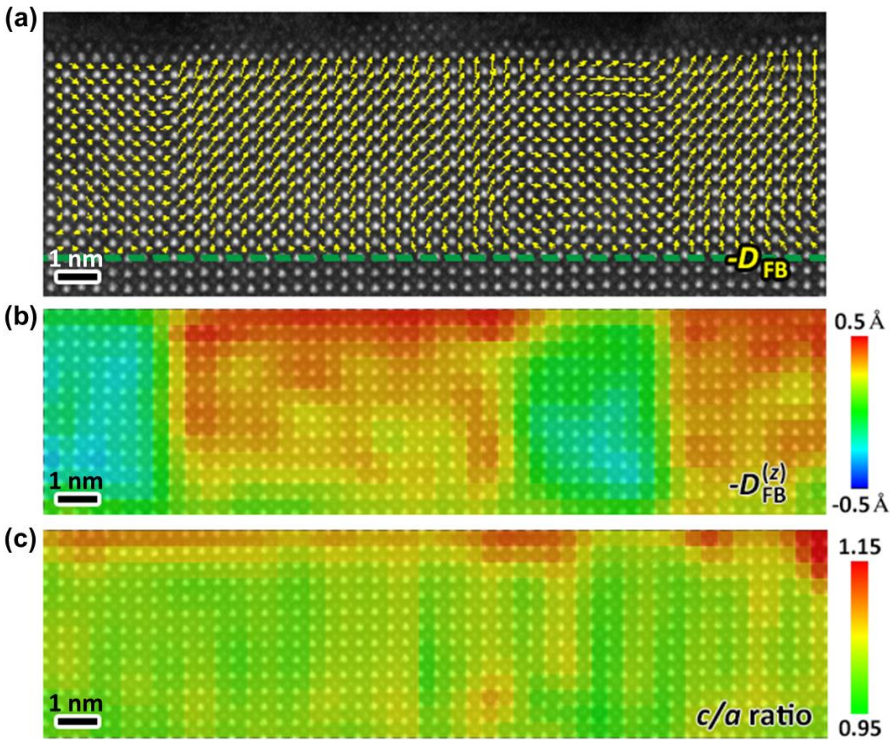

Fig. 4.6 Distribution of polarization and strain in a 5 nm $BiFeO_3$ thin film
HAADF STEM image of a 5 nm $BiFeO_3$ film grown on $TbScO_3$ overlaid with **(a)** $-\boldsymbol{D_{FB}}$ map, **(b)** $-\boldsymbol{D_{FB}}^{(z)}$ map, **(c)** *c*/*a* ratio map of the film. The green dashed line in (a) mark the position of the $BiFeO_3/TbScO_3$ interface.

As a matter of fact, the unique surface defects of Bi_2O_{3-x} monolayers could be ubiquitous in $BiFeO_3$ films, and their effects can become less prominent with the increase of the film thickness. Fig. 4.6 displays the mapping results for a 5 nm $BiFeO_3$ film grown on $TbScO_3$. Although the same type of Bi_2O_{3-x} defects are still observed at the surface of this 5 nm film, the underlying domain structures are very different from the undulating domains observed in the 2 nm film, and they are much alike the regular stripe-patterns with *R*-like polarization in most regions. The defects are primarily located on the upward polarized domains and have induced enhanced polarization and *c*/*a* ratios in the top several lattice layers below them. In the downward polarized domains without defects on the surface, the polarization is suppressed throughout the thickness as a result of the depolarization field; increased *c*/*a* ratios, however, are still observed in the top several layers. Such increased *c*/*a* ratios in the downward polarized domains could be caused by a clamping effect of the neighboring upward polarized domains, since the upward domains are much wider than the downward ones. For sufficiently thick films, for example, a 20 nm $BiFeO_3$ film as shown in Fig. 4.7, the effects of both the surface defects and the depolarization field on the bulk domains become negligible. As a result, the film is composed of conventional 109° stripe domains and the polarization vectors across the 109° domain wall are *R*-like and symmetric.

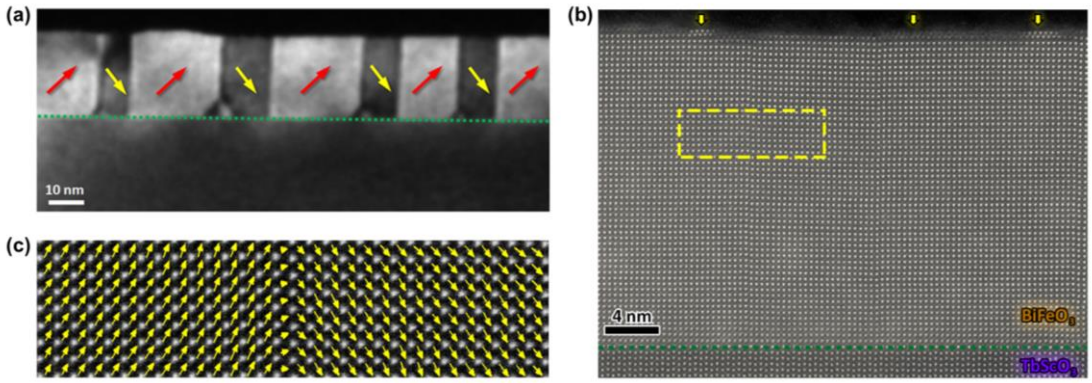

Fig. 4.7 Domain and polarization structures in a 20 nm $BiFeO_3$ thin film
(a) Dark-field TEM image of a 20 nm $BiFeO_3$ film grown on$TbScO_3$, in which the interface is indicated by the green dashed line. The red and yellow arrows indicate the polarization direction of each domain. **(b)** Cross-sectional HAADF STEM image of same film. The interface is indicated by the green dashed line. The yellow arrows indicate the surface monolayer defects. (**c**) -$\boldsymbol{D_{FB}}$ mapping of the local region highlighted by the yellow rectangle in (b).

In conclusion, the combined experimental and theoretical studies demonstrate that the surface defects can play a critical role in controlling structures and properties of ferroelectric ultrathin films. The defect-introduced giant polarization in the ultrathin film could be utilized to enhance the functionalities of ferroelectric nanodevices, such as ferroelectric tunneling junctions. The defect-induced mixed-phase structures with large polarization gradient and strong strain variant may produce giant piezoelectricity and thus could be used for electromechanical applications. Furthermore, as it has been well known that surface relaxation and reconstruction are very common in a variety of ferroelectric oxides, the finding of the critical role of surface defects suggests that boundary-condition engineering through precise control of surface defective structures may offer a new dimension to tailoring properties of ferroelectric ultrathin films, which would impel the minimization of ferroelectric nanodevices.

4.4 Defect induced hedgehog polarization states

Topological structures in ferroics, owing to the unique properties they can possess, hold great promise for the development of future nanoelectronic devices[207]. Examples include ferroic domain walls, magnetic skyrmions, and magnetic/ferroelectric vortices. Domain walls are the most widely studied ferroic topologies due to their abundance in as grown materials and the fact that, they can be easily created, erased, and reconfigured by external electric, magnetic or strain fields. Numerous novel functionalities have been found at these 2D boundaries. For example, it has been discovered that domain boundaries in non-polar materials can be ferroelectrically polarized[208]; ferromagnetic domain walls can exist in antiferromagnetic or paramagnetic materials[209,210]; and ferroelectric domain walls can possess novel properties such as enhanced conductivities[64] and photovoltaic effects[69] (see chapter 1.1 for more details).

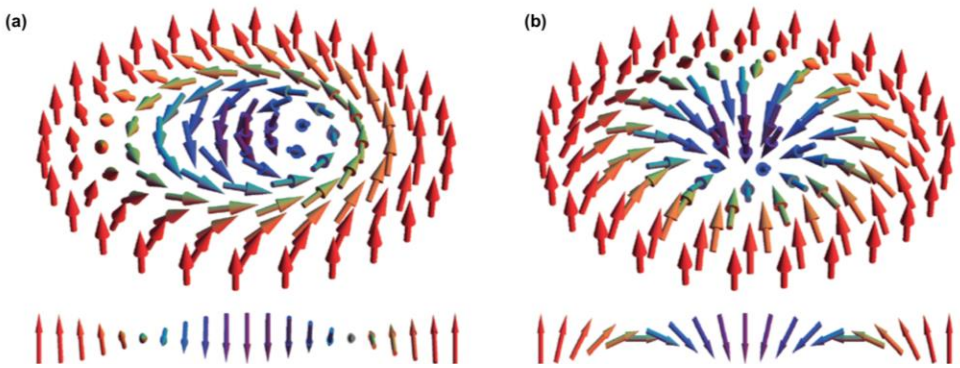

Fig. 4.8 Spin textures of magnetic skyrmions
(a) Vortex-like skyrmions with Bloch-type spin rotations. **(b)** Hedgehog-like skyrmions with Neel-type spin rotations[211].

Magnetic skyrmions are topologically protected spin configurations that can be stabilized by Dzyaloshinskii-Moriya interactions[212]. Two types of spin textures, *i.e.*, vortex-like and hedgehog-like patterns, can form at magnetic skyrmions. The vortex-like

skyrmions have been observed in chiral magnets[213,214], where the spin vectors rotate in the tangential planes that is perpendicular to the radial directions, forming Bloch-type rotations[211] (Fig. 4.8a). In contrast, the hedgehog-like skyrmions can be observed in non-chiral magnets and their spin rotations are Neel-type, restricted in the radial planes[211] (Fig. 4.8b). The gradual spin-rotation patterns of skyrmions usually occur within diameters of 20–90 nm and these patterns can produce emergent electromagnetic fields, allowing the skyrmions to be efficiently manipulated[215,216]. Magnetic skyrmions can also be highly mobile, driven by a spin-transfer torque mechanism at ultralow current densities[217], and this makes skyrmions as promising candidates for current-driven memory devices. Moreover, atomic-scale 2D lattices of magnetic skyrmions have been stabilized in monolayer Fe films[215], indicating the potential application in high-density magnetic memories.

Vortex topologies occur when the magnetization or polarization continuously rotate about one point, forming flux-closure structures to reduce the magnetic or electric fields. In magnetic vortices, in-plane spin vectors circulate around the center of the core, where the magnetization is forced out of plane[218]. In ferroelectrics, however, the flux-closure structure doesn't necessarily involve the polarization rotation from in-plane to out-of-plane direction from the periphery to the core[219]; and it can be composed of quadrant domains with reversed out-of-plane polarizations[89]. The use of ferroelectric vortices as functional elements in nanodevices is particularly attractive, since they can be manipulated by electric fields and they are very small, only singles of nanometers in diameters[220], as a result of the strong electrostriction in ferroelectrics (coupling between the polarization and the lattice). This is in contrast to magnetic vortices, which have much

larger dimensions (tens or hundreds of nanometers) due to relatively weak magnetostriction in ferromagnetics. Recent advances in the synthesis of thin-film heterostructures have enabled the creation of arrays of polarization vortices[89,105,220] in ferroelectric $PbTiO_3$ and $BiFeO_3$ thin films. These vortex domains could be switchable and thus give rise to an unusually high density of bits for storage.

Here, a new ferroic topology in addition to the well-known skyrmions and vortices, that is, hedgehog/antihedgehog polarization states, is observed in $BiFeO_3$ thin films. These hedgehog/antihedgehog states are comprised of nanodomains that present exotic polarization rotation patterns and form mixed-phase structures; and they can also be coupled with polarization vortices. Their novel properties could be useful for nanoelectronic and electromechanical applications. They are stabilized by nanoscale non-stoichiometric impurity defects inserted into the $BiFeO_3$ matrix, indicating a potential new route for control of polarization topology by using defects as nano-building-blocks.

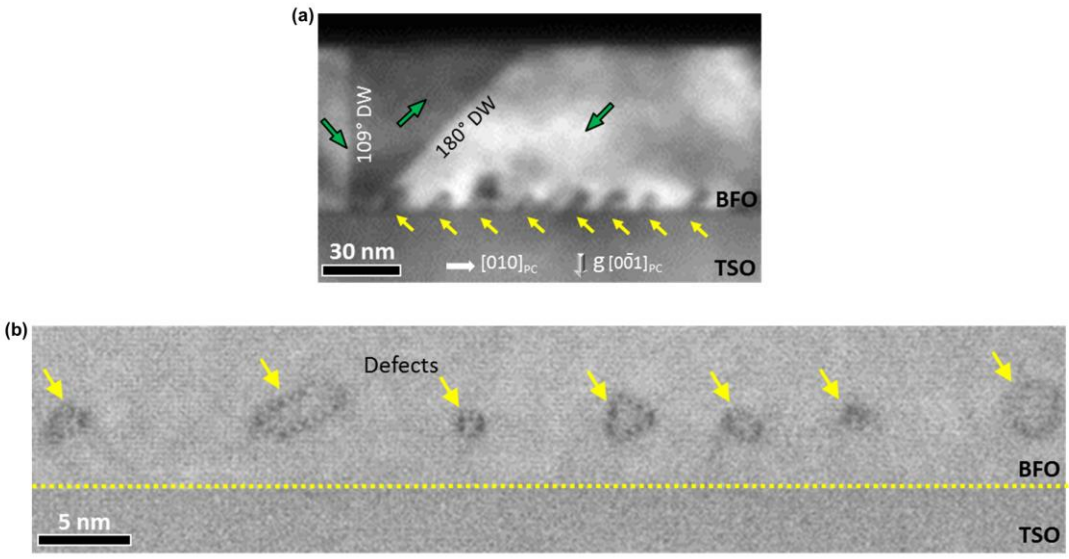

Fig. 4.9 Domain structure and defects in a $BiFeO_3$ thin film
(a) Cross-sectional dark-field TEM image of a $BiFeO_3$ thin film grown on a $TbScO_3$ substrate, showing a triangular 109°/180° domain wall (DW) junction in the bulk film and a high-density array of nanodomains (indicated by the yellow arrows) above the $BiFeO_3/TbScO_3$ interface. **(b)** HAADF STEM image of the $BiFeO_3/TbScO_3$ interfacial region, where the interface is indicated by the yellow dashed line and an array of defects are observed at a uniform height of 3 nm above the interface.

The domain structure of a 60 nm thick $BiFeO_3$ film grown on $TbScO_3$ substrate is shown in a cross-sectional dark-field TEM image (Fig. 4.9a), where the overlaid green arrows mark the polarization orientations derived from mapping the $-\boldsymbol{D_{FB}}$ vectors based on HAADF STEM images. A typical structure of paired 109° and 180° domain walls is observed in the bulk film. Within the matrix of the bulk domains, a high-density array of nanodomains are also observed just above the $BiFeO_3/TbScO_3$ interface. While the previous study has reported arrays of flux-closure triangular nanodomains observed at the intersection of the 109° domain walls and the $BiFeO_3/TbScO_3$ interfaces, which are induced by non-uniform depolarization fields present at the boundaries[89]; the nanodomains observed here show different characteristics: they have a much higher density than the striped 109° or 180° domain walls in the bulk film, and can exist in the middle of a single domain where the depolarization field is generally uniform. Moreover,

using high-resolution HAADF STEM imaging (Fig. 4.9b), an array of defects are observed and each defect is found to be right above the nanodomain structures. This array of defects may cause local variations in free energy and stabilize the observed nanodomains.

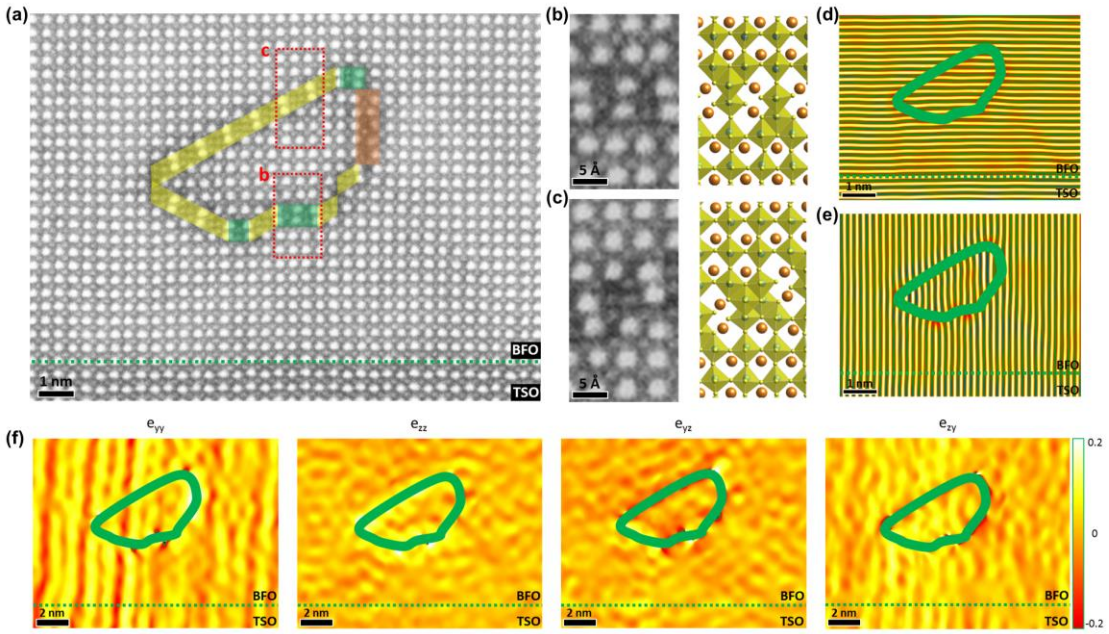

Fig. 4.10 Atomic structure associated with a semicircular loop defect in the $BiFeO_3$ thin film **(a)** HAADF STEM image of the $BiFeO_3/TbScO_3$ interfacial region containing one typical semicircular loop defect. The defect is composed of a vertical segment (highlighted in brown) with distorted pseudocubic perovskite lattices and non-stoichiometric planar (highlighted in green) and stepped (highlighted in yellow) structural units. **(b)** Magnified image of the non-stoichiometric planar unit in the defect (red rectangular highlighted region "b" in (a)) and a model of its corresponding atomic structure on the right. **(c)** Magnified image of the non-stoichiometric stepped unit in the defect (red rectangular highlighted region "c" in (a)) and a model of its corresponding atomic structure on the right. **(d)** The same HAADF STEM image filtered in Fourier space by including only the $00h_{PC}$ diffraction frequencies. **(e)** The same HAADF STEM image filtered in Fourier space by including only the $0h0_{PC}$ diffraction frequencies. **(f)** Geometric phase analysis (GPA) of the same HAADF STEM images reveals the strain in the $BiFeO_3$ lattice surrounding the semi-circular loop defect. Note that the striped patterns in the GPA image of e_{yy} are caused by scanning noise in the STEM image.

To present the atomic-scale structures of the defects, a magnified HAADF image of an interfacial region containing one typical semi-circle loop defect in the $BiFeO_3$ matrix is shown in Fig. 4.10a. As there are no other elements introduced during film growth, the defect should also be composed of Bi, Fe, and O atoms, with the brighter dots

in the HAADF image corresponding to the heavier Bi columns and the weaker dots corresponding to the lighter Fe columns. This defect is generally composed of two parts: a short vertical segment on the right (brown highlighted) with a distorted pseudocubic perovskite lattice, where an apparent lattice expansion is observed along the horizontal direction; and a long curved/inclined segment on the left (yellow and green highlighted) with a non-stoichiometric structure. Furthermore, the non-stoichiometric segments are composed from two structural units -- planar units (green highlighted) and stepped units (yellow highlighted). While the planar unit is oriented on the horizontal $(001)_{PC}$ plane and adopts the structure of one pair of Bi atoms alternating with one pair of Fe atoms; the stepped unit has an inclined orientation and is formed from one pair of Bi atoms alternating with two pairs of Fe atoms.

The same type of planar and stepped structural units have also been observed in previous studies of Nd and Ti doped antiferroelectric $BiFeO_3$ by MacLaren *et. al.*[221,222]. Their detailed structural study suggests that the Fe atoms within the defects are coordinated by 6 oxygens in the form of edge-sharing oxygen octahedra, forming the planar and stepped structural units shown schematically in Fig. 4.10b and c, respectively. As a result, there is an excess of anions (more oxygen) at the defect, with a net local negative charge density of -1.4 C/m^2 at the planar unit, and -1.1 C/m^2 at the stepped unit. Another feature associated with the defects is an atomic shift of one half of a pseudocubic unit cell of the $BiFeO_3$ lattice across the planar units in the $[001]_{PC}$ direction, and a shift of one half of a pseudocubic unit cell of the $BiFeO_3$ lattice across the stepped units in both the $[010]_{PC}$ and $[001]_{PC}$ directions, as evident in the Fourier-filtered images shown in Fig. 4.10d,e. These shifts, however, do not induce obvious strain in the $BiFeO_3$ matrix,

as shown by the quantitative analysis of the high-resolution HAADF images using geometric phase analysis (GPA) in Fig. 4.10f. The shift in the lattice occurs mainly through atomic rearrangement within the defects and the shifted lattices are separated, accommodating the strain and forming an isolated nanoregion enclosed by the loop defect.

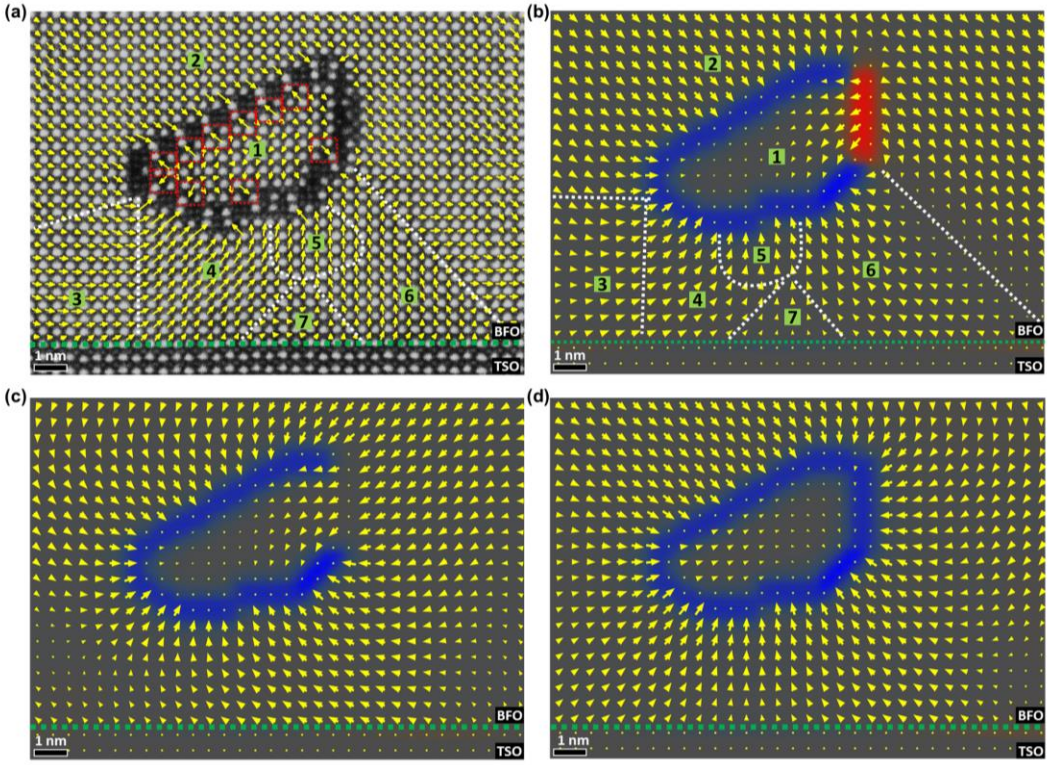

Fig. 4.11 Polarization map of the nanodomains surrounding the semicircular loop defect
(a) The same HAADF STEM image as Fig. 4.10a overlaid with the polarization vectors (-$\boldsymbol{D_{FB}}$). The white dashed lines represent the positions of domain walls. **(b-d)** Phase field simulation of polarization distribution in the image plane of the domain structure stabilized by a charged defect with configuration similar to the experimental observation, but with different charge distributions. The polarization vectors are overlaid on a color map of the charge distribution, where the red, blue, and gray colors represent positive (+1.1 C/m^2), negative (-1.1 C/m^2), and zero charge densities, respectively.

The polarization distribution in the $BiFeO_3$ lattice adjacent to the defect was determined by mapping of the -$\boldsymbol{D_{FB}}$ vectors (Fig. 4.11a). Within the region enclosed by the semi-circle defect (marked as region "1"), a hedgehog polarization state can be identified. While the polarization vectors of each unit cell in the middle of this region are

attenuated and oriented along multiple directions, the unit cells that are in contact with the defects at the boundary (red rectangular highlighted unit cells) show significant lattice distortions with enhanced polarization pointing outward towards the defect. In contrast, the $BiFeO_3$ lattice outside of the defect presents a continuous rotation of polarization, with polarization vectors generally pointing inward towards the defect, except for the right-side region where the polarization vectors are pointing outward. This arrangement leads to the formation of six different nanodomains (marked as from "2" to "7") with mixed-phase structures surrounding the defect. The "2", "4", and "6" domains possess normal *R*-like structures with polarizations oriented along the body diagonal directions. However, the "3" and "5" domains adopt polarizations on $[010]_{PC}$ and $[001]_{PC}$ directions, respectively, resembling horizontal or vertical *T*-like structures[188]. Within region "7", significantly attenuated polarizations were observed. These observed mixed-phase structures are apparently more complicated than the previously reported mixed-phases driven by the large epitaxial strain in $BiFeO_3$ films grown on $LaAlO_3$ substrates, in which the phases are composed of alternating stripes of *R*-like and *T*-like domains[50,53]. Moreover, the $BiFeO_3/TbScO_3$ interface has very little strain due to a small lattice mismatch (<0.14%), and the GPA mapping (Fig. 4.10f) shows almost no difference of strain states between different nanodomains, excluding the possibility of strain as the main driving force for the formation of the observed mixed-phase structures.

Since the polarization directions are generally pointing toward the defects and most segments of the defects are negatively charged, a plausible mechanism is that the polarization distortions of the $BiFeO_3$ lattices are modified by the build-in fields induced by the charge on the defects. To gain further insight of the driving force for the formation

of the nanodomains, phase field simulations were employed to calculate the stable polarization configuration in the presence of a charged defect. In the simulated $BiFeO_3$ thin film, a defect was created with similar shape to what has been observed in the experiment, and then additional charge was applied at the defect, with no additional eigenstrain introduced by the defect from the lattice mismatch between the defect and the matrix, as the defect induced strain has a minimal effect on the polarization (see discussion below). For simplicity, a uniform charge density of -1.1 C/m^2 was applied to the left curved/inclined part of the defect, which was composed of planar and stepped units. For the right-side vertical segment of the defect with a distorted perovskite lattice, although its defect chemistry cannot be directly determined by STEM imaging, the lattice expansion along the horizontal direction could indicate a local accumulation of oxygen vacancies[223,224]. Therefore, a positive charge density of +1.1 C/m^2 was applied at the right-side vertical segment of the defect. For comparison, two more cases with negative (-1.1 C/m^2) and zero charge densities in this region were also considered. In each case, a random polarization distribution was set as the initial structure, and simulations repeated with different initial random polarization distribution in the system were found to be consistent.

Simulations of the polarization configuration around the defect for the three cases, positive, negative, and zero charge densities at the right-side vertical segment of the defect, are shown in Fig. 4.11b-d, respectively. In all three cases, attenuated polarization is observed within the semi-circle region enclosed by the defect (region “1”), with the exception of the very large polarization of a few unit cells at the region boundary. This could be a result of the exclusion of the experimentally observed distorted unit cells at the

region boundary (red rectangular highlighted unit cells in Fig. 4.11a) from the simulation. Nevertheless, simulated results with a positive charge density on the right-side vertical segment of the defect (Fig. 4.11b) reproduced almost all of the features in the polarization configuration outside of the defect captured in the experiment, including the polarization reorientation around the defect with the formation of six different polarized regions (region “2” to “7”), the change of lattice symmetries into *T*-like structures in region “3” and “5”, and the attenuated polarization in region “7”. In comparison, the stabilized polarization surrounding the defect in the cases with negative and zero charge densities at the vertical segment of the defect (Fig. 4.11c, d) present perfect antihedgehog configurations with the polarization vectors all pointing into the defect, which is inconsistent with experimental observations and suggests that the positive charge case is the most probable situation.

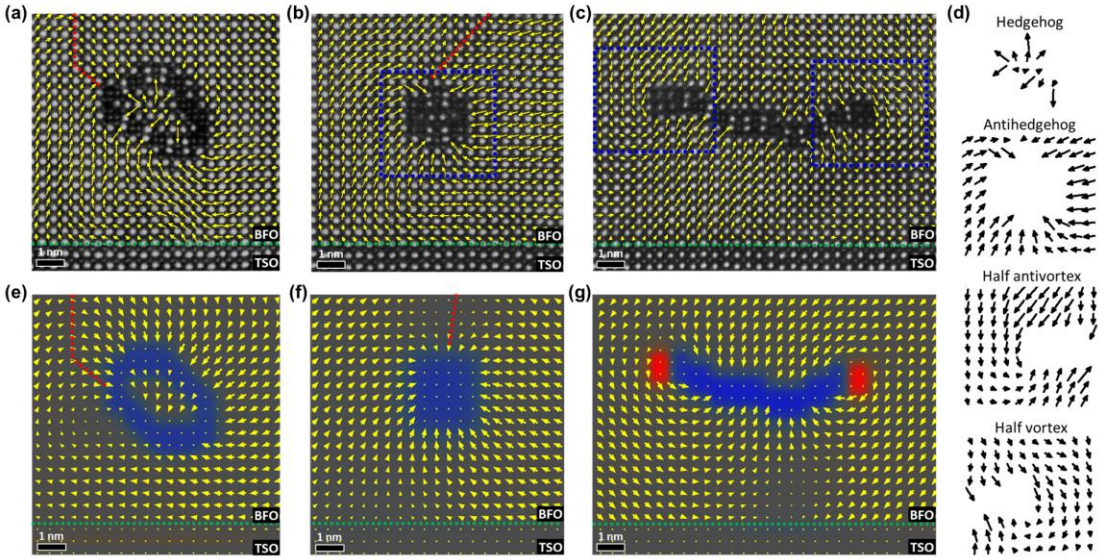

Fig. 4.12 Polarization maps of nanodomains induced by three different defects in the $BiFeO_3$ thin film

(a-c) HAADF STEM images of three different defects above the $BiFeO_3/TbScO_3$ interface, where the polarization vectors ($-\boldsymbol{D_{FB}}$) are overlaid on the $BiFeO_3$ lattice. The dashed red line marks the domain walls that penetrate to the top surface of the thin film. **(d)** Magnified map of the polarization vectors in the nanoregion enclosed by the loop defect in (a) and in the three different nanoregions highlighted by the blue rectangles in (b) and (c). **(e-g)** Phase field simulation of polarization distribution in the image plane of the domain structures stabilized by three different charged defects with configurations similar to the experimental observations in (a)-(c). The polarization vectors are overlaid on a color map of the charge distribution, where red, blue, and gray colors represent positive (+1.1 C/m^2), negative (-1.1 C/m^2), and zero charge densities, respectively.

The hedgehog/antihedgehog domains and the polarization rotation phenomena are ubiquitous around the defects in the $BiFeO_3$ thin films, and can also induce polarization vortices, as shown by three examples in Fig. 4.12a-c. Similar to the previous case shown in Fig. 4.10, these defects are mainly comprised of the same type of planar units and stepped units, with the same excess of oxygen and thus local net negative charge. Some additional variations were noted, for example, within the circle defect in Fig. 4.12a, an inclined segment on the right-side composed of five consecutive pairs of Fe atoms but no Bi atoms in between was observed. Examination of the polarization shows hedgehog/antihedgehog domains around the defects are also accompanied by the formation of multiple polarized regions and mixed-phase structures. In Fig. 4.12a, a tiny

hedgehog polarization state with a diameter of 4 unit cells was observed in the nanoregion circled by the defect. In both Fig. 4.12a and b, antihedgehog polarization states are stabilized at the shell regions encircling the defects; and within larger ranges outside the defects, the overall continuous polarization rotation patterns lead to flux-closure vortex structures. In Fig. 4.12c, a pair of polarization semi-vortex and semi-antivortex structures at the two edges of the linear defect are produced as a result of the formation of a "head to head" polarization configuration above and below the defect. These defects can also be associated with the termination of domain walls extending to the surface of the film. In Fig. 4.12a, a vertical 109˚domain wall (red dashed line) that penetrates to the top surface of the film is terminated at the circle loop defect; in Fig. 4.12b, an inclined 180˚ domain wall (red dashed line) is terminated at the rod-like defect.

Phase field simulations containing similar charged defects in the $BiFeO_3$ thin film matrix reproduce similar domain structures as shown in Fig. 4.12e-g, where charge densities of -1.1 C/m^2 or +1.1 C/m^2 were used. The simulated polarization structures surrounding the charged defects generally follow the experimental observations, forming antihedgehog states and vortex domains in Fig. 4.12e, f, and semi-antivortex at the left edge of the linear defect in Fig. 4.12g. The particular polarization rotation patterns at the simulated vortices, however, do not exactly match the experimental results. The differences could be attributed to the uniform charge density assumed in the simulation, as the charge distribution on the defects should be non-uniform in reality due to local charge compensation by the mobile carriers or oxygen vacancies at the defects. Such a non-uniform charge density should alter the polarization structures.

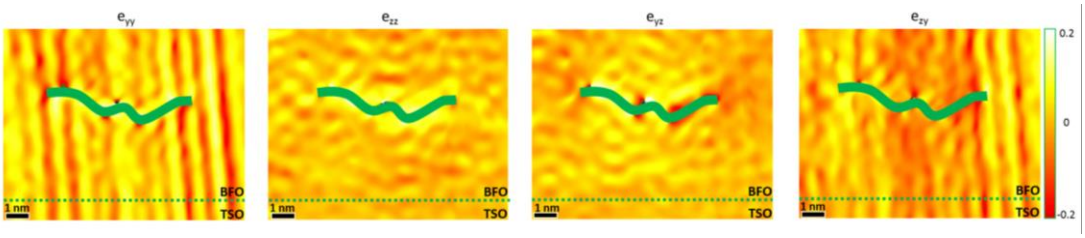

Fig. 4.13 Strain map of the $BiFeO_3$ lattice surrounding the linear defect
GPA mapping of the HAADF STEM images shows the lack of strain in the $BiFeO_3$ lattice surrounding the linear defect. Note that the striped patterns in e_{yy} and e_{zy} are caused by scanning noises of the STEM image.

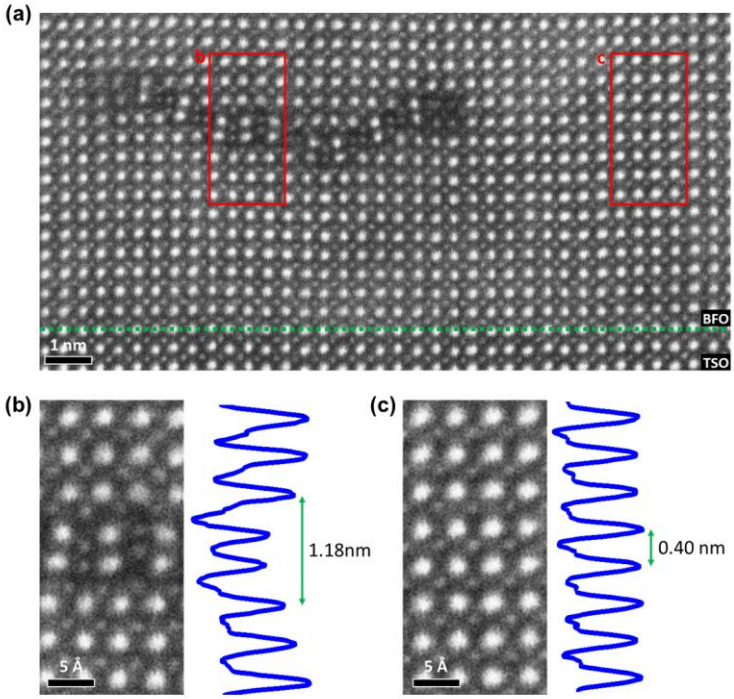

Fig. 4.14 Analysis of out-of-plain strain (e_{zz}) at the linear defect
(a) HAADF STEM image of the $BiFeO_3/TbScO_3$ interface region containing the linear defect. **(b)** Magnified image of the planar unit of the defect (red rectangular highlighted region "b" in (a)) and the corresponding averaged intensity line profile on the right. The measured thickness of the defect is 1.18 nm. **(c)** Magnified image of a nanoregion in the $BiFeO_3$ matrix and the corresponding averaged intensity line profile on the right. The measured out-of-plane lattice constant of $BiFeO_3$ is 0.40 nm. Since the defect is inserted into the $BiFeO_3$ matrix, replacing three pseudocubic unit cells, there should be a small compressive strain (e_{zz}~ -0.02) at the defect.

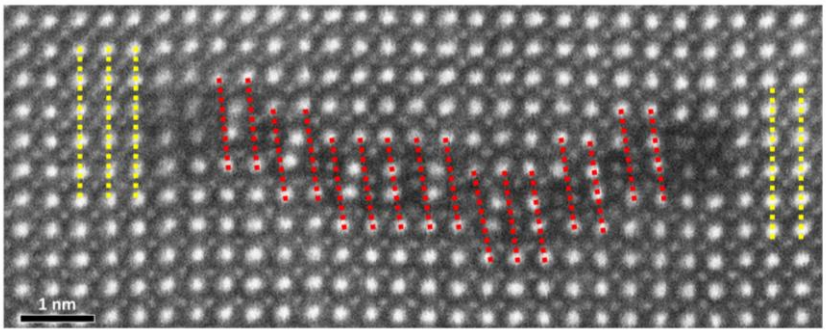

Fig. 4.15 Analysis of the shear strain (e_{yz}) at the linear defect
HAADF STEM image of the linear defect shows the atomic shifts of the $BiFeO_3$ lattice across the defect leads to a large shear strain (e_{yz} ~ -0.16) between the top and the bottom boundaries of the defect.

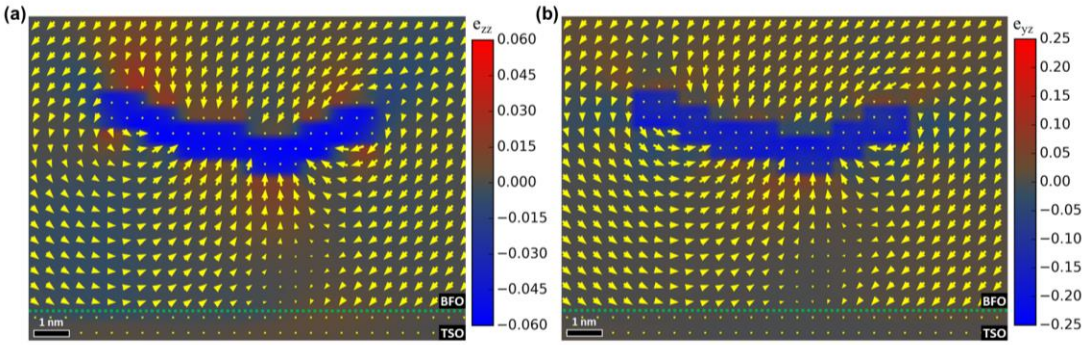

Fig. 4.16 Assessment of the influence of the defect-induced strain on the polarization distribution around the linear defect
Phase field simulation of the polarization distribution in the image plane of the domain structure stabilized by a charged defect with a configuration and charge distribution identical to the case in Fig. 4.12g, but with an added eigenstrain of **(a)** e_{zz} of -0.05 or **(b)** e_{yz} of -0.20. The color represents e_{zz} in (a) and e_{yz} in (b).

Taking the linear defect as an example, the effect of defect-induced strain on the polarization structures was further considered. Similar to the analysis of the case of the semi-circle defect shown in Fig. 4.10f, GPA mapping of the case of the linear defect in Fig. 4.13 also shows little strain in the $BiFeO_3$ matrix surrounding the linear defect. However, since the defect and $BiFeO_3$ have different atomic structures, GPA cannot be used to determine the strain at the defect or at the defect/$BiFeO_3$ boundary. Therefore, the defect induced strain was estimated by directly measuring the lattice spacing of the

atomic structures (Fig. 4.14 and 4.15). The measurements show a low compressive strain (e_{yy} ~ -2%) along the vertical direction at the defect (Fig. 4.14), and a large shear strain (e_{yz} ~ -16%) along the horizontal direction (Fig. 4.15). Phase field simulations to examine the effect of the strain on the polarization were performed, with additional compressive strain (e_{yy} ~ -5%) or shear strain (e_{yz} ~ -20%) applied to the same defect configuration with identical charge conditions as the case shown in Fig. 4.12g. The corresponding simulated polarization patterns are shown in Fig. 4.16a and b, respectively, where the polarization vectors are overlaid on the color map of strain distribution. The large shear strain at the defect is relaxed to less than 5% in the nearby $BiFeO_3$ lattice, consistent with the low strain measured in $BiFeO_3$ by the STEM imaging. The difference in the polarization distribution between the strained conditions (Fig. 4.16) and the zero strain case (Fig. 4.12g) is almost indistinguishable; suggesting that the defect induced strain has a negligible effect on the polarization state.

All these results shown above indicate that the charge on the defects should be the major driving force inducing the observed nanodomain structures, in which the gradient energy from the polarization rotation is counterbalanced by the corresponding reduction in overall electrostatic energy and a change of the charge states on the defects can produce different stable nanodomain patterns. Therefore, the observed nanodomains can only be stabilized after the formation of the defects, not vice versa. The formation mechanism of the defects, however, has not yet been fully understood. In previous studies, the same type of planar and stepped structural defects as those observed here are randomly distributed throughout the material, and rely on the excessive cation charge from doping as a proposed mechanism[221,222]. In the system observed here, however, no

doping procedure was performed during $BiFeO_3$ film growth, and the observed defects are only located at a uniform height along the film thickness, several unit cells above the bottom interface of the film. These suggest the defects could be kinetically trapped due to surface reconstructions or dynamic rearrangement of atomic structures, where stoichiometry fluctuations occurred on the certain level during the layer-by-layer growth.

The reported hedgehog/antihedgehog polarization topologies offer new opportunities to explore the complex interplay of spin, charge, orbital and lattice degrees of freedom in the strongly correlated systems. The hedgehog states can approach sizes down to several unit cells in diameter, which are much smaller than the previously discovered vortices and skyrmions. As the polarization component perpendicular to the hedgehog plane (image plane in this work) may be switchable, further study of the electrical properties and dynamics of the hedgehog states under applied fields may assist future development of nanoelectronic devices such as high-density memories. The mixed-phase structures associated with the antihedgehog states are reminiscent of the ferroelectric domains near a morphotropic phase boundary and therefore may exhibit properties such as giant piezoelectricity, making these states potentially attractive for electromechanical applications.

The observation of defect-induced structure changes in the $BiFeO_3$ thin films should stimulate efforts to design functional patterns of ferroelectric/multiferroic nanodomains or nanopolymorphs with focus on controlling the intrinsic defect structures, and motivate a search for similar mechanism in other functional oxides systems. While conventional chemical engineering methods (composition tuning) and interface engineering methods (boundary condition tuning) only produce structure changes

uniformly distributed within the whole material, defect engineering can generate functional structures at local nanoregions without disruption of the bulk structural patterns, which is desirable as the dimensions of individual elements in nanodevices continue to shrink. Further developments may allow the defects to be introduced in a controlled fashion within the host lattices during material synthesis, or allow the charge state of the defects to be modified by external charge injection methods, opening the door to fine control of nanodomain structures and the creation of new topological states through defect engineering.

CHAPTER 5

Ferroelectric Retention Failure Induced by Impurity Defects

5.1 Background

A long-standing issue that has to be resolved in order to realize ferroelectric applications has been that the switched polarization is sometimes unstable, and can relax to its original state through a spontaneous process of polarization back-switching. Such process, known as "retention failure", can lead to a loss of stored information in ferroelectric memories, and disable functionalities coupled with the switched polarization in multifunctional applications.

The process of retention failure is generally thought to be induced by the thermodynamic instability of the written polarization arising from boundary conditions at interfaces. Electrostatic boundary conditions correlated to the properties and structures of the ferroelectric/electrode interfaces could be the primary cause. For instance, strong depolarization fields can arise at uncompensated interfaces where interfacial dead-layer or non-switchable layers exist[225-227]; and the semiconductor/metal contact at the ferroelectric/electrode interface can generate a Schottky build-in field[7]. An imbalance between the electrostatic boundary conditions at the two interfaces of a ferroelectric film can impose an asymmetric free-energy landscape between the two opposite polarization states, and favor one state over the other, triggering the polarization back-switching. Elastic boundary conditions, *i.e.*, the substrate-induced strain, can also affect the domain

stability. For example, it has been suggested that the depolarization field and the Schottky built-in field at the ferroelectric/electrode interface could be strain-dependent[228]. Furthermore, the substrate-induced strain may be gradually released in ferroelectric films due to the formation of dislocations, resulting in a strain gradient. Such strain gradient can produce an effective build-in field through flexoelectric effects, and therefore can also alter the domain stability[229].

Defects, on the other hand, have been thought to play a secondary role during the process of polarization back-switching, acting as pinning centers hindering the domain wall motion. Previous experimental results have shown that domain walls can be pinned by vacancies[186,230], dislocations[231], phase boundaries[232], or pre-existing ferroelastic domains[233]. In most cases, these pinning centers would increase the stability of the written domains and thus prevent retention failure. However, the effects of impurity defects on the polarization switching and domain stability have been rarely explored.

Here, based on results of atomic-scale STEM and *in situ* TEM, a novel atomic-scale mechanism of impurity-defect-induced retention failure is proposed. The results explicitly show strong build-in fields can be induced by arrays of planar impurity defects located just above the substrate interfaces of $BiFeO_3$ thin films. This build-in field not only leads to head-to-head polarization configurations and polarization enhancement, but also can induce a polarization back-switching and destabilize written domains. The impurity defects therefore could play a dominant role in the control of ferroelectric properties.

5.2 Experimental methods

Film growth and TEM experiments: $BiFeO_3$ films on $LaAlO_3$ substrates were grown by the same pulsed-laser deposition method described in ref. 139. TEM specimen preparation and TEM imaging in different modes, including diffraction-contrast imaging, atomic-resolution HAADF STEM imaging, and *in situ* TEM, were performed using the same methods and the same instruments as those been described in Chapter 3.2.

AFM experiments: AFM was carried out on a Bruker Dimension Icon scanning probe microscope using platinum coated silicon cantilevers. Samples were mounted on standard AFM pucks using silver paint. The cantilever axis was aligned along the $[010]_{PC}$ axis of the $BiFeO_3$ film for imaging.

5.3 Atomic-scale mechanism of defect-induced retention failure

In a 50 nm thick $BiFeO_3$ film grown on $LaAlO_3$ substrate with a 8 nm $La_{0.7}Sr_{0.3}MnO_3$ buffer electrode, typical mixed-phase structures containing stripes of *R*-like domains embedded into *T*-like matrix are induced by the large epitaxial strain (~4.5%) (Fig. 5.1). This work mainly focuses on local regions within the *T*-like matrix, where arrays of planar defects with a length of 5 to 30 nm have been found just above the interfaces (Fig. 5.2a,b). Using HAADF imaging (Fig. 5.2c), the measurements of lattice parameters ($a_\perp$ and $a_{//}$) show that the $a_\perp/a_{//}$ ratio is ~ 1.06 for the majority of the films, which is much smaller than the value of ~ 1.25 measured by X-ray diffraction in the bulk film of *T*-like $BiFeO_3$ grown on $LaAlO_3$ substrate[139], suggesting a possible structural relaxation in the TEM specimen[146]. Nevertheless, mapping of the polarization vectors (-$\boldsymbol{D_{FB}}$) confirms that the majority phase is still *T*-like, since the polarization in most regions

is oriented along the $[00\text{-}1]_{PC}$ direction, with the exception of some interfacial regions below the defects as will be discussed later.

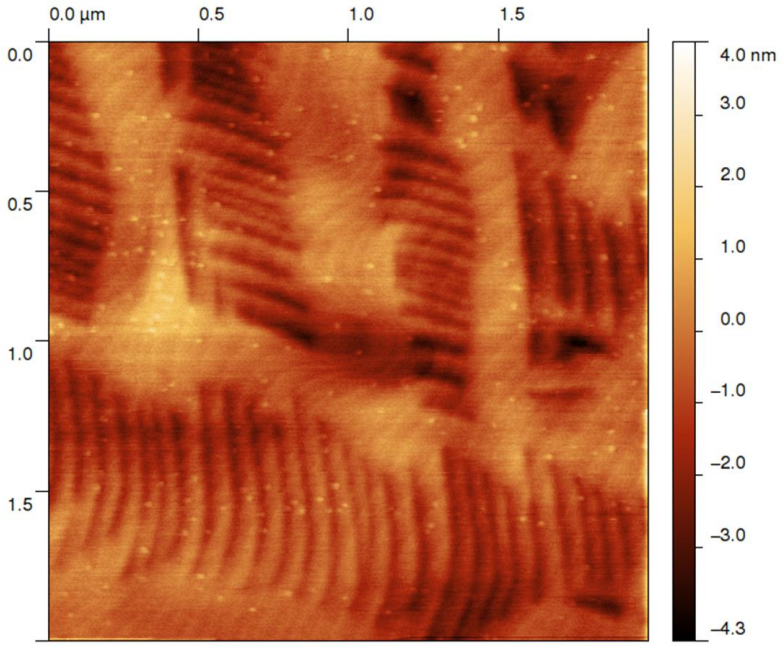

Fig. 5.1 Mixed-phase structures in a $BiFeO_3$ thin film
AFM image of a 50nm $BiFeO_3$ thin film grown on $LaAlO_3$ substrate with an 8 nm $La_{0.7}Sr_{0.3}MnO_3$ buffer bottom electrode. The patterns show the stripes of *R*-like domains embedded into *T*-like matrix in $BiFeO_3$.

A HAADF image of a region containing a planar defect in the $BiFeO_3$ matrix is shown in Fig. 5.2d. As there are no other elements introduced during film growth, the defect should also be composed of Bi, Fe, and O atoms, with the brighter dots in the HAADF image corresponding to the heavier Bi columns, the weaker dots corresponding to the lighter Fe columns, while O columns are not visible. The arrangements of Bi and Fe atoms within the defect closely resemble those in the Aurivillius phase materials, for example, Bi_2WO_6, which is built by alternating layers of Bi_2O_2 and pseudo-perovskite blocks[234]. Examining the defect, a form of Bi_2FeO_{6-x}, composed of a single FeO_6 octahedron sandwiched between two Bi_2O_2 layers as shown in Fig. 5.2f is reasonable,

though the exact stoichiometry of oxygen and the precise positions of oxygen atoms may differ. The same-type of Bi_2FeO_{6-x} impurity phase has also been observed in a previous study of $BiFeO_3$ thin films grown on $TbScO_3$ or on $SrTiO_3$ substrates. Their observations show much larger regions of the impurity phase, forming nanoparticles or nanopillars embedded in the $BiFeO_3$ matrix with a feature size of tens of nanometers[235]. In comparison, the impurity planar defects observed here are a few atomic layers in thickness and perfectly epitaxial along the film grown direction. Furthermore, the observations in Fig. 5.3 suggest that the impurity structures here may also adopt smaller dimensions, forming point defects in the thin films.

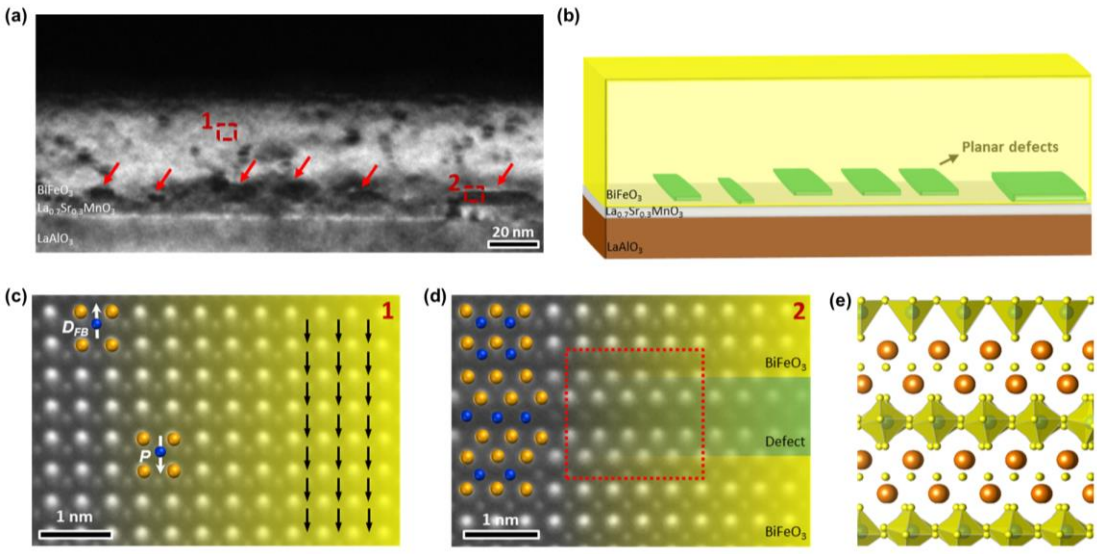

Fig. 5.2 Atomic structures and defects in the $BiFeO_3$ thin film
(a) Cross-sectional dark-field TEM image showing an array of planar defects just above the $BiFeO_3/La_{0.7}Sr_{0.3}MnO_3$ interface. The defects are indicated by the red arrows. **(b)** Schematic of the heterostructure in (a). **(c,d)** Averaged HAADF STEM images of the two different regions highlighted by the rectangles in (a). The overlaid brown and blue balls mark the Bi and Fe atom columns, respectively. The black arrows in (c) indicate a uniform downward polarization. **(e)** Atomic model of the defect highlighted by the rectangle in (d).

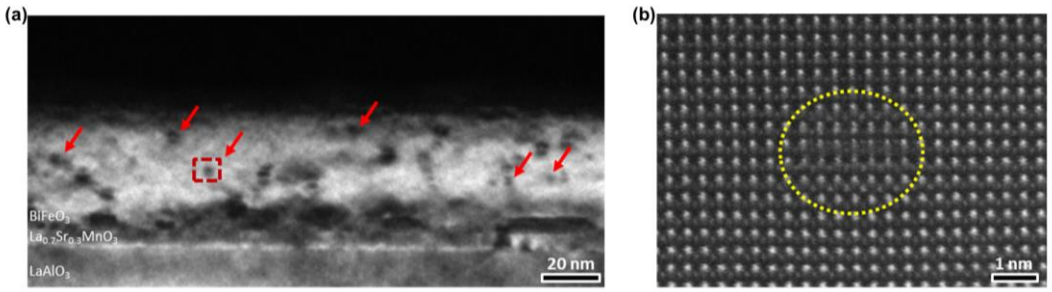

Fig. 5.3 Point defects in the $BiFeO_3$ thin film
(a) The same cross-sectional dark-field TEM image as Fig. 5.2a. The red arrows here indicate the impurity point defects randomly distributed in the $BiFeO_3$ film. **(b)** HAADF STEM image of the region highlighted by the rectangle in (a). As the contrast in the STEM image comes from the average of all unit cells along the beam direction, the small point defect buried in the film cannot be clearly resolved, but just imposes a perturbation on the image of the host lattice within the circle-highlighted region. This point defect should have minor effect on the ferroelectric properties of the film, as no obvious structure changes have been observed in the $BiFeO_3$ lattice surrounding it.

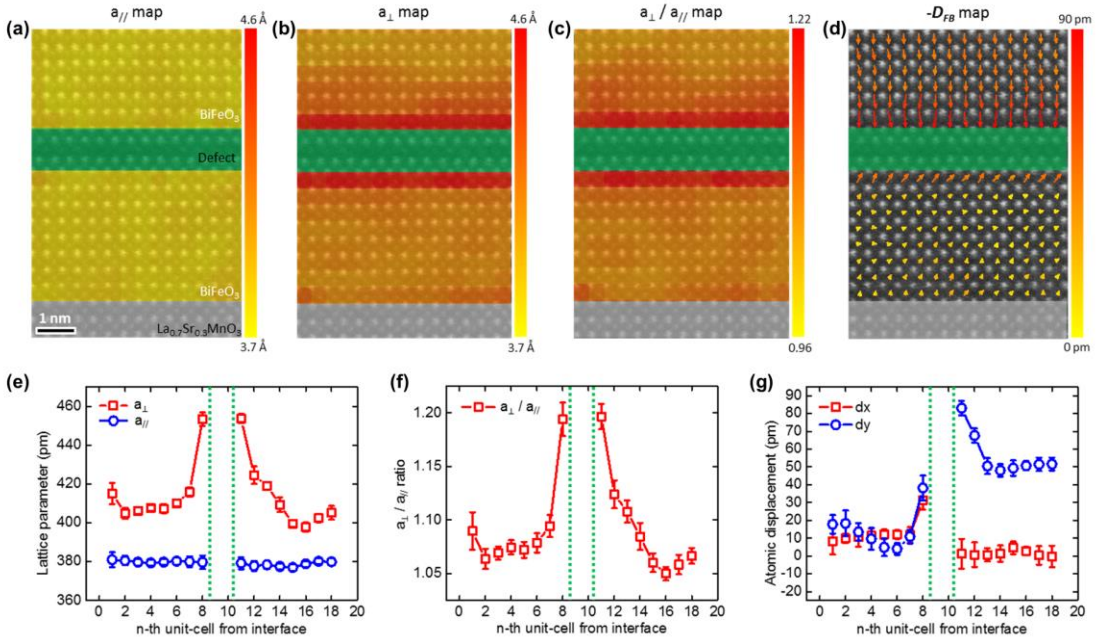

Fig. 5.4 Distribution of strain and polarization across a planar defect
Color maps of **(a)** the in-plane lattice parameter $a_{//}$, **(b)** the out-of-plane lattice parameter $a_{\perp}$, **(c)** the $a_{\perp}/a_{//}$ ratio, and **(d)** spatial distribution of the $-\boldsymbol{D_{FB}}$ vectors overlaid on a same HAADF STEM image, in which one planar defect is located above the $BiFeO_3/La_{0.7}Sr_{0.3}MnO_3$ interface. The defect and the $La_{0.7}Sr_{0.3}MnO_3$ substrate are overlaid with uniform green and silver colors, respectively. **(e-g)** Plot of the $a_{//}$, $a_{\perp}$, $a_{\perp}/a_{//}$ and $-\boldsymbol{D_{FB}}$ changes in the $BiFeO_3$ lattice across the defect. The green dashed lines mark the position of the defect. In (g), dx and dy represents the magnitude of the horizontal and vertical components of the $-\boldsymbol{D_{FB}}$ vector.

The strain and polarization distribution in the $BiFeO_3$ lattice adjacent to the planar defect was determined by mapping of the lattice parameters (Fig. 5.4a-c) and the polarization vectors (Fig. 5.4d). By averaging the data from each lattice layer, the change of the lattice parameters and the magnitude of the polarization vectors in the $BiFeO_3$ lattice across the defect can be plotted in Fig. 5.4e-g. The strain mapping results show that, while $a_{//}$ remains almost constant in the examined region (Fig. 5.4a and e), a sharp increase of $a_{\perp}$ occurred in the lattice layers that are in contact with the defect (Fig. 5.4b and e), resulting in a local high $a_{\perp}/a_{//}$ ratio of ~1.20 (Fig. 5.4c and f). Such a large change in the out-of-plane lattice parameter could be a result of the out-of-plane lattice mismatch between the defect and the $BiFeO_3$ matrix. Since a defect with a thickness of 10.2 Å is inserted into the $BiFeO_3$ lattice, replacing three pseudocubic unit cells with a thickness of 12.1 Å in the out-of-plane direction (Fig. 5.5), there should be a large compressive strain (e_{zz} ~ -0.16) at the defect; and this defect induced strain could induce the observed lattice expansion in the neighboring $BiFeO_3$ lattice layers.

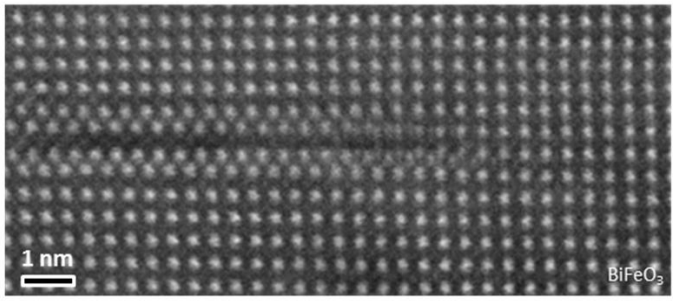

Fig. 5.5 Structure of the defect edge
HAADF STEM image showing the edge of a defect embedded in the $BiFeO_3$ lattice. This clearly shows the defect replaces three pseudocubic unit cells in the out-of-plane direction.

The map of the polarization vectors surrounding the planar defect generally shows a “head-to-head” polarization configuration (Fig. 5.4d). An enhancement in the magnitude of the polarization was also observed in the $BiFeO_3$ lattice in contact with the

defect (Fig. 5.4g), which could be associated with the local increase in tetragonality, *i.e.* the enhanced $a_{\perp}/a_{//}$ ratio in these layers. Furthermore, the polarization map shows an interesting change in the $BiFeO_3$ lattice symmetry in the two regions separated by the defect (Fig. 5.4d). While the lattice above the defect possesses a *T*-like structure with polarization oriented along [00-1] direction, the lattice below the defect is *R*-like, with mostly attenuated polarization oriented along the diagonal, pointing upward in the image plane. Such mixed-phase structures can be associated with the defect. As a previous study has shown, Bi_2O_2 layers existing at the substrate interfaces can induce the formation of *T*-like structures in moderately strained (~1.5%) $BiFeO_3$ films grown on $SrTiO_3$ substrates[236], the Bi_2O_2 layers within the defect observed here could also be the origin for the stabilization of the *T*-like phase above the local *R*-like structures. On the other hand, the upward polarization below the defect is opposed to a downward polarization enforced by the build-in field at the Schottky contact of the $BiFeO_3/La_{0.7}Sr_{0.3}MnO_3$ (n-type-semiconductor/metal) interface[136]. This suggests that a strong build-in field pointing towards the defect exists, and this field can flip the polarization adjacent to the defect. The stabilized upward polarization below the defect is further suppressed by the downward Schottky built-in field from the back electrode, resulting in the observed *R*-like structure with attenuated polarization.

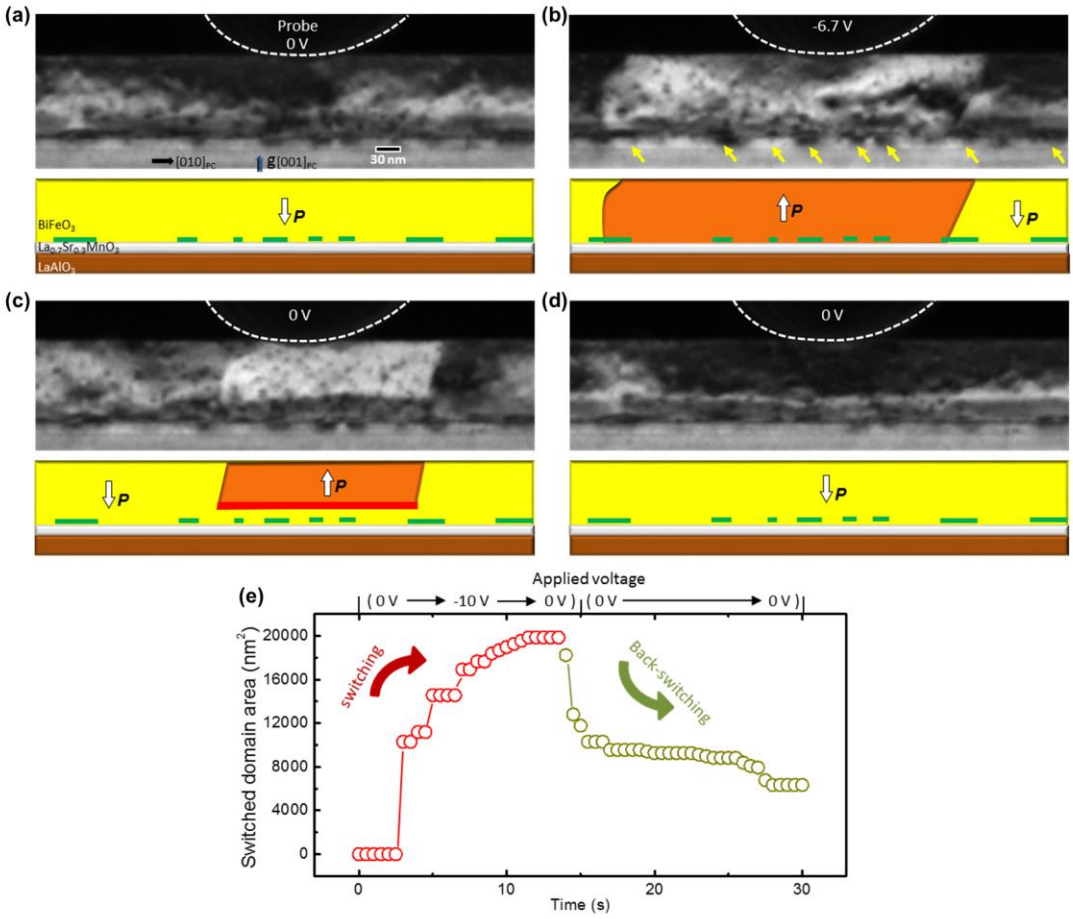

Fig. 5.6 Domain switching in presence of defects
Chronological TEM dark-field image series and corresponding schematics depicting the evolution of an upward polarized domain from a downward polarized matrix: **(a)** the original state, **(b)** switched domain under an applied voltage, **(c)** metastable domain state at 15 seconds after the voltage was removed, and **(d)** final stable state at 20 minutes after the voltage was removed. An array of planar defects at the $BiFeO_3/La_{0.7}Sr_{0.3}MnO_3$interface are indicated by the yellow arrows in (b) and are shown by the green lines in the schematics. In (c), a horizontal tail-to-tail charged domain wall is marked by the red line in the schematic. **(e)** The measured area of the switched domain as a function of time (bottom axis) and applied voltage (top axis).

A local domain switching event in the presence of an array of planar defects just above the $BiFeO_3/La_{0.7}Sr_{0.3}MnO_3$ interface was captured by *in situ* TEM (Fig. 5.6). The film was originally with a *T*-like downward polarization. A bias was applied between a tungsten surface probe and the $La_{0.7}Sr_{0.3}MnO_3$ bottom electrode and was linearly changed from 0 V to -10.0 V and then to 0 V over 15 s. As shown in a chronological series of TEM images (Fig. 5.6a-d), although a large domain with upward polarization can be

created with an applied voltage (Fig. 5.6b), the created domain shrank back to a smaller metastable state in 15 seconds after the voltage was removed (Fig. 5.6c). In both these domain states, the domain boundaries on both sides were not in the low-energy vertical orientation and instead presented inclined or curved configurations. This could be caused by domain wall pinning at various defects, such as the impurity defects or vacancies that commonly exist in the thin films. While the switched domain under the applied voltage (Fig. 5.6b) penetrated across the whole film thickness, the metastable domain after the removal of the applied voltage (Fig. 5.6c) only penetrated from the top surface to about 35 nm in depth, resulting in the formation of a horizontal tail-to-tail charged domain walls at the middle of the film. This suggests that, at this stage, a spontaneous back-switching only occurred at a thin sub-layer above the $BiFeO_3/La_{0.7}Sr_{0.3}MnO_3$ interface. A plot of the measured area of the switched domain as a function of time and applied voltage, in Fig. 5.6e, shows that the domain switching induced by the applied bias is affected by several pinning and field-assisted unpinning of domain walls, where the domain area remained constant until the applied voltage was large enough to trigger a sudden expansion in the area. Right before the applied voltage went to zero, partial spontaneous back-switching of the written domain occurred via a rapid shrinkage to the metastable state. After the applied voltage went to zero, this metastable state further relaxed to smaller sizes through slow thermodynamic processes, and eventually annihilated in 20 minutes (Fig. 5.6d).

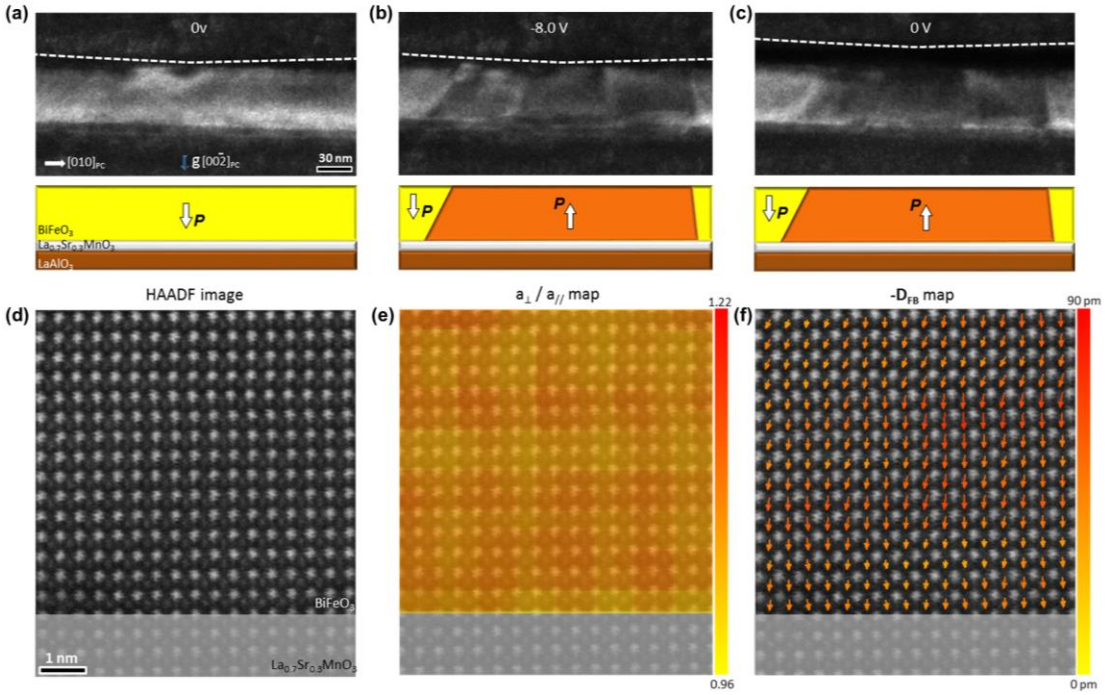

Fig. 5.7 Domain switching and structures in a $BiFeO_3$ thin film without defects
(a-c) Chronological TEM dark-field image series depicting the creation and stabilization of an upward polarized domain in a local $BiFeO_3$ film without planar impurity defects. **(d)** HAADF STEM image showing the $BiFeO_3/La_{0.7}Sr_{0.3}MnO_3$ interfacial region of the local film. **(e)** Color map of the $a_\perp/a_{//}$ ratio and **(f)** spatial distribution of the $-\boldsymbol{D_{FB}}$ vectors overlaid on the same HAADF STEM image.

The most likely cause for the observed retention failure phenomena in these $BiFeO_3$ films is a strong build-in field pointing downward through the film. The built-in field here would be a combination of the Schottky field from the back contact and the downward build-in field induced by the planar defects above them. The planar-defect-induced field is probably the dominant one. Firstly, it should be stronger than the Schottky field, as it is large enough to stabilize a polarization opposite to the Schottky field below the defect, forming a head-to-head polarization configuration that is usually considered unstable in ferroelectrics (Fig. 5.4d). Secondly, as observed in Fig. 5.6c, the early stage of the retention failure was accompanied by a back-switching at the interfacial sub-layer, suggesting the back-switching was initiated at local nanoregions adjacent to the planar defects. Finally, it is found at local regions in the same film where impurity

defects were not observed, a switched domain can be stable after the removal of the applied voltage (Fig. 5.7a-c). In these regions, maps of lattice parameters and polarization vectors based on HAADF STEM images show uniform *T*-like domain structures above the interfaces (Fig. 5.7d-f). In regions both with and without impurity defects, the films show good epitaxy at the $BiFeO_3/La_{0.7}Sr_{0.3}MnO_3$ interfaces without dislocations, excluding depolarization effects caused by interfacial non-ferroelectric dead-layers[225] or flexoelectric effects induced by strain gradients[229]. Therefore, the existence of the impurity defects should be crucial to the observed domain instability.

As $BiFeO_3$ film growth is very sensitive to the deposition parameters and pure-phase $BiFeO_3$ can only be obtained within narrow parameter combinations[235], the impurity defects observed in these thin films could have been be induced by slight stoichiometry fluctuations that occurred during the growth, either due to fluctuations of deposition parameters or inhomogeneity of the target. This suggests that, impurity defects, either of the Aurivillius phase or other types of structures, may be common in perovskite thin films. Such defects can strongly interact with the host materials. The observations of defect induced domain instability may help explain past disagreements regarding retention failure in some ferroelectric systems. Also, although these defects would destabilize written domains and would be less useful for ferroelectric memory devices, the finding of defect induced change of polarization structures suggests potential new routes of tuning ferroelectric properties. For example, by intentionally creating impurity defects into the film matrix during material growth, a strong build-in field can be introduced at the local nanoregions. This may lead to the stabilization of novel functional domain patterns that are not easily accessible through the conventional strain

engineering, such as the mixed-phase head-to-head polarization structure observed here. Engineering defects, therefore, open new avenues for control of nanodomain structures and the creation of new polarization states.

CHAPTER 6

Summary and Future Work

In this work, by using atomic-resolution scanning transmission electron microscopy (STEM) and *in situ* transmission electron microscopy (TEM), I presented a microscopic study of polarization structures and switching dynamics in ferroelectric $BiFeO_3$ thin films. In particular I have observed a local *rhombohedral*-like-to-*tetragonal*-like structure transition at the strongly charged domain walls (sCDWs); and I have created a dramatic resistive switching in the local thin film through electrical manipulation of the sCDW. These findings provide novel insight on the effects of polarization bound charge on the ferroelectric structures, and open up the possibility for the development of new device paradigms through control of sCDWs. I have also discovered a strong interaction between the ferroelectric polarization and nanoscale impurity defects that commonly exist in ferroelectrics. These defects can lead to polarization enhancement in ultrathin $BiFeO_3$ films, challenging the long-term understanding that the ferroelectric polarization is inevitably suppressed under reduced dimensions. They can also stabilize novel hedgehog/antihedgehog polarization topologies and different types of mixed-phase structures, both of which could be useful for nanoelectronic or nanoelectromechanical applications. In presence of these impurity defects, the stability of newly created domain can be dramatically altered as well. These results indicate that engineering impurity defects could be a new route for tuning

ferroelectric properties.

In next steps, a continuation of study on domain structures or switching phenomena associated with the sCDWs or the impurity defects can be further performed. These include, for example, probing the coupling between the stress and the polarization bound charge, and the possible mechanical switching of sCDW; or exploring the interaction between the bulk domain pattern and impurity defects with larger dimensions. Future work can also be made into detecting ferroelectric domain switching with improved spatial and time resolution. Currently, the spatial resolution (~1 nm) of the *in situ* TEM is practically limited by the fact that only low-magnification imaging modes are available due to the difficulty in tilting the TEM specimen arbitrarily using *in situ* TEM holders; and the time resolution (~30 ms) is restricted by the capability of the TEM imaging system including record cameras. Along with the progress made to improve the performance of TEM and *in situ* platforms, however, the very near future will undoubtedly see direct atomic-scale observation or ultrafast detection of ferroelectric switching events. This would lead to more fundamental understanding of the microscopic processes of domain nucleation and domain wall motion. In addition, refinements of *in-situ* methods, including new holders for application of electrical bias, force, and light, and even for control of liquid and atmosphere environment, open the door to examining the behavior of ferroelectric materials under many different conditions, all within the TEM. These developments provide wide opportunities for studying the properties and functionalities of ferroelectric materials, and facilitate development of ferroelectric-based devices in information and energy technologies.

APPENDIX

Contributions from others

For the results of charged domain walls presented in chapter 3, Alexander Melville and Carolina Adamo carried out the sample synthesis; Christopher Nelson, Peng Gao, Yi Zhang (older), and Sungjoo Kim contributed to prepare the TEM samples and take the TEM images. Jacob Jokisaari and Yi Zhang (younger) performed the experiments using the scanning probe microscopy, including PFM and SSRM. Jason Britson did the phase-field simulations.

In chapter 4, for the results of ultrathin $BiFeO_3$ films, the sample was synthesized by Colin Heikes; the original TEM images were taken by Christopher Nelson and Peng Gao; EELS experiments and DFT calculations was carried out by Lin Xie; and the phase-field simulation was performed by Zijian Hong. For the results of hedgehog/antihedgehog domains, the sample was synthesized by Carolina Adamo; the original TEM images were taken by Jacob Jokisaari and Peng Gao; and the phase-field simulation was performed by Xiaoxing Cheng.

In chapter 5, the films used in the study were grown by Christianne Beekman. The AFM experiment was done by Jacob Jokisaari.

BIBLIOGRAPHY

1 Scott, J. F. Applications of modern ferroelectrics. *Science* **315**, 954-959 (2007).

2 Kalinin, S. V., Morozovska, A. N., Chen, L. Q. & Rodriguez, B. J. Local polarization dynamics in ferroelectric materials. *Rep. Prog. Phys.* **73**, 056502 (2010).

3 Damjanovic, D. Ferroelectric, dielectric and piezoelectric properties of ferroelectric thin films and ceramics. *Rep. Prog. Phys.* **61**, 1267-1324 (1998).

4 Vonhippel, A., Breckenridge, R. G., Chesley, F. G. & Tisza, L. High Dielectric Constant Ceramics. *Ind. Eng. Chem.* **38**, 1097-1109 (1946).

5 Gruverman, A. & Kholkin, A. Nanoscale ferroelectrics: processing, characterization and future trends. *Rep. Prog. Phys.* **69**, 2443-2474 (2006).

6 Scott, J. F. & Dearaujo, C. A. P. Ferroelectric Memories. *Science* **246**, 1400-1405 (1989).

7 Dawber, M., Rabe, K. M. & Scott, J. F. Physics of thin-film ferroelectric oxides. *Rev. Mod. Phys.* **77**, 1083-1130 (2005).

8 D. B. Williams & C. B. Carter. Transmission Electron Microscopy: A Textbook for Materials Science. *Springer 2nd Ed.*

9 Rundqvist, P., Vorobiev, A., Kollberg, E. & Gevorgian, S. Large signal circuit model of parallel-plate ferroelectric varactors. *J. Appl. Phys.* **100**, 074101 (2006).

10 Gevorgian, S. S. & Kollberg, E. L. Do we really need ferroelectrics in paraelectric phase only in electrically controlled microwave devices? *IEEE Trans. Microw. Theory Techn.* **49**, 2117-2124 (2001).

11 Liu, S. T. & Maciolek, R. B. Rare-Earth-Modified $Sr_{0.5}Ba_{0.5}Nb_2O_6$ Ferroelectric-Crystals and Their Applications as Infrared Detectors. *J. Electron. Mater.* **4**, 91-100 (1975).

12 Muralt, P. Micromachined infrared detectors based on pyroelectric thin films. *Rep. Prog. Phys.* **64**, 1339-1388 (2001).

13 Cole, M. W., Geyer, R. G. & Nothwang, W. D. Unpatterned ferroelectric thin film measurements for optimization of perovskite oxide thin film based microwave devices. *Ferroelectrics* **342**, 83 (2006).

14 Lancaster, M. J., Powell, J. & Porch, A. Thin-film ferroelectric microwave devices. *Supercond. Sci. Tech.* **11**, 1323-1334 (1998).

15 DeFlaviis, F., Alexopoulos, N. G. & Stafsudd, O. M. Planar microwave integrated phase-shifter design with high purity ferroelectric material. *IEEE Trans. Microw. Theory Techn.* **45**, 963-969 (1997).

16 Ledermann, N. *et al.* {100}-textured, piezoelectric $Pb(Zr_x Ti_{1-x})O_3$ thin films for MEMS: integration, deposition and properties. *Sensor Actuat. a-Phys.* **105**, 162-170 (2003).

17 Ledermann, N. *et al.* Piezoelectric cantilever microphone for photoacoustic GAS detector. *Integr. Ferroelectr.* **35**, 1907-1914 (2001).
18 Udayakumar, K. R. *et al.* Ferroelectric Thin-Film Ultrasonic Micromotors. *Ieee Micro Electro Mechanical Systems*, 109-113 (1991).
19 Kingon, A. I. & Streiffer, S. K. Ferroelectric films and devices. *Curr. Opin. Solid St. M.* **4**, 39-44 (1999).
20 Jeong, D. S. *et al.* Emerging memories: resistive switching mechanisms and current status. *Rep. Prog. Phys.* **75**, 076502 (2012).
21 Han, S. T., Zhou, Y. & Roy, V. A. L. Towards the Development of Flexible Non-Volatile Memories. *Adv. Mater.* **25**, 5425-5449 (2013).
22 Scott, J. F. Device physics of ferroelectric thin-film memories. *Jpn. J. Appl. Phys.* **38**, 2272-2274 (1999).
23 Auciello, O., Scott, J. F. & Ramesh, R. The physics of ferroelectric memories. *Phys. Today* **51**, 22-27 (1998).
24 Ishiwara, H. Ferroelectric Random Access Memories. *J. Nanosci. Nanotechno.* **12**, 7619-7627 (2012).
25 Fujisaki, Y. & Ishiwara, H. Ferroelectric thin film depositions for various types of FeRAMs (Ferroelectric random access memories). *Materials and Processes for Nonvolatile Memories* **830**, 65-76 (2005).
26 Hoffman, J. *et al.* Ferroelectric Field Effect Transistors for Memory Applications. *Adv. Mater.* **22**, 2957-2961 (2010).
27 Sakai, S. & Takahashi, M. Recent Progress of Ferroelectric-Gate Field-Effect Transistors and Applications to Nonvolatile Logic and FeNAND Flash Memory. *Materials* **3**, 4950-4964 (2010).
28 Brondijk, J. J., Asadi, K., Blom, P. W. M. & de Leeuw, D. M. Physics of organic ferroelectric field-effect transistors. *J. Polym. Sci. Pol. Phys.* **50**, 47-54 (2012).
29 Asadi, K., Blom, P. W. M. & de Leeuw, D. M. Conductance switching in organic ferroelectric field-effect transistors. *Applied Physics Letters* **99**, 053306 (2011).
30 Zheng, Y. *et al.* Graphene Field-Effect Transistors with Ferroelectric Gating. *Phys. Rev. Lett.* **105**, 166602 (2010).
31 Hong, X., Posadas, A., Zou, K., Ahn, C. H. & Zhu, J. High-Mobility Few-Layer Graphene Field Effect Transistors Fabricated on Epitaxial Ferroelectric Gate Oxides. *Phys. Rev. Lett.* **102**, 136808 (2009).
32 Liu, X. Q., Liu, Y. L., Chen, W., Li, J. C. & Liao, L. Ferroelectric memory based on nanostructures. *Nanoscale Res. Lett.* **7**, 285 (2012).
33 Choi, T., Lee, S., Choi, Y. J., Kiryukhin, V. & Cheong, S. W. Switchable Ferroelectric Diode and Photovoltaic Effect in $BiFeO_3$. *Science* **324**, 63-66 (2009).
34 Jiang, A. Q. *et al.* A Resistive Memory in Semiconducting $BiFeO_3$ Thin-Film Capacitors. *Adv. Mater.* **23**, 1277-1281 (2011).
35 Hong, S. *et al.* Large Resistive Switching in Ferroelectric $BiFeO_3$ Nano-Island Based Switchable Diodes. *Adv. Mater.* **25**, 2339-2343 (2013).
36 Tsymbal, E. Y. & Kohlstedt, H. Applied physics - Tunneling across a ferroelectric. *Science* **313**, 181-183 (2006).
37 Garcia, V. *et al.* Giant tunnel electroresistance for non-destructive readout of ferroelectric states. *Nature* **460**, 81-84 (2009).

38 Garcia, V. *et al.* Ferroelectric Control of Spin Polarization. *Science* **327**, 1106-1110 (2010).
39 Maksymovych, P. *et al.* Polarization Control of Electron Tunneling into Ferroelectric Surfaces. *Science* **324**, 1421-1425 (2009).
40 Gajek, M. *et al.* Tunnel junctions with multiferroic barriers. *Nat. Mater.* **6**, 296-302 (2007).
41 Chanthbouala, A. *et al.* A ferroelectric memristor. *Nat. Mater.* **11**, 860-864 (2012).
42 Yin, Y. W. *et al.* Enhanced tunnelling electroresistance effect due to a ferroelectrically induced phase transition at a magnetic complex oxide interface. *Nat. Mater.* **12**, 397-402 (2013).
43 Wen, Z., Li, C., Wu, D., Li, A. D. & Ming, N. B. Ferroelectric-field-effect-enhanced electroresistance in metal/ferroelectric/semiconductor tunnel junctions. *Nat. Mater.* **12**, 617-621 (2013).
44 Tanaka, K. *et al.* Scanning Nonlinear Dielectric Microscopy Nano-Science and Technology for Next Generation High Density Ferroelectric Data Storage. *Jpn. J. Appl. Phys.* **47**, 3311-3325 (2008).
45 Fujimoto, K. & Cho, Y. S. High-speed switching of nanoscale ferroelectric domains in congruent single-crystal $LiTaO_3$. *Applied Physics Letters* **83**, 5265-5267 (2003).
46 Cho, Y. Ultrahigh-density ferroelectric data storage based on scanning nonlinear dielectric microscopy. *Jpn. J. Appl. Phys.* **44**, 5339-5343 (2005).
47 Cho, Y. S. *et al.* Tbit/inch^2 ferroelectric data storage based on scanning nonlinear dielectric microscopy. *Applied Physics Letters* **81**, 4401-4403 (2002).
48 Lee, D. *et al.* Multilevel Data Storage Memory Using Deterministic Polarization Control. *Adv. Mater.* **24**, 402 (2012).
49 Kim, D. J. *et al.* Ferroelectric Tunnel Memristor. *Nano Lett.* **12**, 5697-5702 (2012).
50 Zeches, R. J. *et al.* A Strain-Driven Morphotropic Phase Boundary in $BiFeO_3$. *Science* **326**, 977-980 (2009).
51 Mazumdar, D. *et al.* Nanoscale Switching Characteristics of Nearly Tetragonal $BiFeO_3$ Thin Films. *Nano Lett.* **10**, 2555-2561 (2010).
52 Seidel, J. *et al.* Electronic Properties of Isosymmetric Phase Boundaries in Highly Strained Ca-Doped $BiFeO_3$. *Adv. Mater.* **26**, 4376-4380 (2014).
53 Zhang, J. X. *et al.* Large field-induced strains in a lead-free piezoelectric material. *Nat. Nanotechnol.* **6**, 97-101 (2011).
54 Kleemann, W., Borisov, P., Bedanta, S. & Shvartsman, V. V. Multiferroic and Magnetoelectric Materials-Novel Developments and Perspectives. *Ieee T. Ultrason. Ferr.* **57**, 2228-2232 (2010).
55 Eerenstein, W., Mathur, N. D. & Scott, J. F. Multiferroic and magnetoelectric materials. *Nature* **442**, 759-765 (2006).
56 Ma, J., Hu, J. M., Li, Z. & Nan, C. W. Recent Progress in Multiferroic Magnetoelectric Composites: from Bulk to Thin Films. *Adv. Mater.* **23**, 1062-1087 (2011).
57 Chu, Y. H. *et al.* Electric-field control of local ferromagnetism using a magnetoelectric multiferroic. *Nat. Mater.* **7**, 478-482 (2008).

58 Wu, S. M. *et al.* Reversible electric control of exchange bias in a multiferroic field-effect device. *Nat. Mater.* **9**, 756-761 (2010).
59 Chiba, D. *et al.* Electrical control of the ferromagnetic phase transition in cobalt at room temperature. *Nat. Mater.* **10**, 853-856 (2011).
60 Pantel, D., Goetze, S., Hesse, D. & Alexe, M. Reversible electrical switching of spin polarization in multiferroic tunnel junctions. *Nat. Mater.* **11**, 289-293 (2012).
61 Cherifi, R. O. *et al.* Electric-field control of magnetic order above room temperature. *Nat. Mater.* **13**, 345-351 (2014).
62 Ji, W., Yao, K. & Liang, Y. C. Bulk Photovoltaic Effect at Visible Wavelength in Epitaxial Ferroelectric $BiFeO_3$ Thin Films. *Adv. Mater.* **22**, 1763-1766 (2010).
63 Yi, H. T., Choi, T., Choi, S. G., Oh, Y. S. & Cheong, S. W. Mechanism of the Switchable Photovoltaic Effect in Ferroelectric $BiFeO_3$. *Adv. Mater.* **23**, 3403-3407 (2011).
64 Seidel, J. *et al.* Conduction at domain walls in oxide multiferroics. *Nat. Mater.* **8**, 229-234 (2009).
65 Seidel, J. *et al.* Domain Wall Conductivity in La-Doped $BiFeO_3$. *Phys. Rev. Lett.* **105**, 197603 (2010).
66 Guyonnet, J., Gaponenko, I., Gariglio, S. & Paruch, P. Conduction at Domain Walls in Insulating $Pb(Zr_{0.2}Ti_{0.8})O_3$ Thin Films. *Adv. Mater.* **23**, 5377 (2011).
67 Maksymovych, P. *et al.* Dynamic Conductivity of Ferroelectric Domain Walls in $BiFeO_3$. *Nano Lett.* **11**, 1906-1912 (2011).
68 Farokhipoor, S. & Noheda, B. Conduction through 71 degrees Domain Walls in $BiFeO_3$ Thin Films. *Phys. Rev. Lett.* **107**, 127601 (2011).
69 Yang, S. Y. *et al.* Above-bandgap voltages from ferroelectric photovoltaic devices. *Nat. Nanotechnol.* **5**, 143-147 (2010).
70 Seidel, J. *et al.* Efficient Photovoltaic Current Generation at Ferroelectric Domain Walls. *Phys. Rev. Lett.* **107**, 126805 (2011).
71 Maksymovych, P. *et al.* Tunable Metallic Conductance in Ferroelectric Nanodomains. *Nano Lett.* **12**, 209-213 (2012).
72 Vasudevan, R. K. *et al.* Domain Wall Geometry Controls Conduction in Ferroelectrics. *Nano Lett.* **12**, 5524-5531 (2012).
73 Sluka, T., Tagantsev, A. K., Bednyakov, P. & Setter, N. Free-electron gas at charged domain walls in insulating $BaTiO_3$. *Nat. Commun.* **4**, 1808 (2013).
74 Crassous, A., Sluka, T., Tagantsev, A. K. & Setter, N. Polarization charge as a reconfigurable quasi-dopant in ferroelectric thin films. *Nat. Nanotechnol.* **10**, 614 (2015).
75 Lee, W. M. *et al.* Spatially Resolved Photodetection in Leaky Ferroelectric $BiFeO_3$. *Adv. Mater.* **24**, Op49-Op53 (2012).
76 Sluka, T., Tagantsev, A. K., Damjanovic, D., Gureev, M. & Setter, N. Enhanced electromechanical response of ferroelectrics due to charged domain walls. *Nat. Commun.* **3**, 748 (2012).
77 Wang, J. *et al.* Epitaxial $BiFeO_3$ multiferroic thin film heterostructures. *Science* **299**, 1719-1722 (2003).
78 Bark, C. W. *et al.* Tailoring a two-dimensional electron gas at the $LaAlO_3/SrTiO_3$ (001) interface by epitaxial strain. *P. Natl. Acad. Sci.* **108**, 4720-4724 (2011).

79 Schlom, D. G. *et al.* Strain tuning of ferroelectric thin films. *Annu. Rev. Mater. Res.* **37**, 589-626 (2007).
80 Schlom, D. G., Chen, L. Q., Pan, X. Q., Schmehl, A. & Zurbuchen, M. A. A thin film approach to engineering functionality into oxides. *J. Am. Ceram. Soc* **91**, 2429-2454 (2008).
81 Martin, L. W., Chu, Y. H. & Ramesh, R. Advances in the growth and characterization of magnetic, ferroelectric, and multiferroic oxide thin films. *Mat. Sci. Eng. R* **68**, Iii-133 (2010).
82 Ramesh, R. & Spaldin, N. A. Multiferroics: progress and prospects in thin films. *Nat. Mater.* **6**, 21-29 (2007).
83 Choi, K. J. *et al.* Enhancement of ferroelectricity in strained $BaTiO_3$ thin films. *Science* **306**, 1005-1009 (2004).
84 Ederer, C. & Spaldin, N. A. Effect of epitaxial strain on the spontaneous polarization of thin film ferroelectrics. *Phys. Rev. Lett.* **95**, 257601 (2005).
85 Schlom, D. G. *et al.* Elastic strain engineering of ferroic oxides. *MRS Bulletin* **39**, 118-130 (2014).
86 Adamo, C. *et al.* Effect of biaxial strain on the electrical and magnetic properties of (001) $La_{0.7}Sr_{0.3}MnO_3$ thin films. *Applied Physics Letters* **95**, 112504 (2009).
87 Infante, I. C. *et al.* Bridging Multiferroic Phase Transitions by Epitaxial Strain in $BiFeO_3$. *Phys. Rev. Lett.* **105**, 057601 (2010).
88 Bea, H. *et al.* Evidence for Room-Temperature Multiferroicity in a Compound with a Giant Axial Ratio. *Phys. Rev. Lett.* **102**, 217603 (2009).
89 Nelson, C. T. *et al.* Spontaneous vortex nanodomain arrays at ferroelectric heterointerfaces. *Nano Lett.* **11**, 828-834 (2011).
90 Haeni, J. H. *et al.* Room-temperature ferroelectricity in strained $SrTiO_3$. *Nature* **430**, 758-761 (2004).
91 Cao, J. B. & Wu, J. Q. Strain effects in low-dimensional transition metal oxides. *Mat. Sci. Eng. R* **71**, 35-52 (2011).
92 Lee, K. & Baik, S. Ferroelastic domain structure and switching in epitaxial ferroelectric thin films. *Annu. Rev. Mater. Res.* **36**, 81-116 (2006).
93 Zavaliche, F. *et al.* Ferroelectric domain structure in epitaxial $BiFeO_3$ films. *Applied Physics Letters* **87**, 182912 (2005).
94 Chen, Y. B. *et al.* Ferroelectric domain structures of epitaxial (001) $BiFeO_3$ thin films. *Applied Physics Letters* **90**, 072907 (2007).
95 Streiffer, S. K. *et al.* Domain patterns in epitaxial rhombohedral ferroelectric films. I. Geometry and experiments. *J. Appl. Phys.* **83**, 2742-2753 (1998).
96 Damodaran, A. R. *et al.* Nanoscale Structure and Mechanism for Enhanced Electromechanical Response of Highly Strained $BiFeO_3$ Thin Films. *Adv. Mater.* **23**, 3170-3175 (2011).
97 Zhang, J. X. *et al.* Microscopic Origin of the Giant Ferroelectric Polarization in Tetragonal-like $BiFeO_3$. *Phys. Rev. Lett.* **107**, 147602 (2011).
98 Chisholm, M. F., Luo, W. D., Oxley, M. P., Pantelides, S. T. & Lee, H. N. Atomic-Scale Compensation Phenomena at Polar Interfaces. *Phys. Rev. Lett.* **105**, 197602 (2010).

99 Lichtensteiger, C., Fernandez-Pena, S., Weymann, C., Zubko, P. & Triscone, J. M. Tuning of the Depolarization Field and Nanodomain Structure in Ferroelectric Thin Films. *Nano Lett.* **14**, 4205-4211 (2014).
100 Streiffer, S. K. *et al.* Observation of nanoscale 180 degrees stripe domains in ferroelectric $PbTiO_3$ thin films. *Phys. Rev. Lett.* **89**, 067601 (2002).
101 Chu, Y. H. *et al.* Nanoscale Control of Domain Architectures in $BiFeO_3$ Thin Films. *Nano Lett.* **9**, 1726-1730 (2009).
102 Folkman, C. M. *et al.* Stripe domain structure in epitaxial (001) $BiFeO_3$ thin films on orthorhombic $TbScO_3$ substrate. *Applied Physics Letters* **94**, 251911 (2009).
103 Chu, Y. H. *et al.* Nanoscale domain control in multiferroic $BiFeO_3$ thin films. *Adv. Mater.* **18**, 2307-2311 (2006).
104 Jia, C. L., Urban, K. W., Alexe, M., Hesse, D. & Vrejoiu, I. Direct Observation of Continuous Electric Dipole Rotation in Flux-Closure Domains in Ferroelectric $Pb(Zr,Ti)O_3$. *Science* **331**, 1420-1423 (2011).
105 Tang, Y. L. *et al.* Observation of a periodic array of flux-closure quadrants in strained ferroelectric $PbTiO_3$ films. *Science* **348**, 547-551 (2015).
106 Chu, Y. H. *et al.* Domain control in mulfiferroic $BiFeO_3$ through substrate vicinality. *Adv. Mater.* **19**, 2662-2666 (2007).
107 Jang, H. W. *et al.* Domain Engineering for Enhanced Ferroelectric Properties of Epitaxial (001) $BiFeO_3$ Thin Films. *Adv. Mater.* **21**, 817-823 (2009).
108 Wang, R. V. *et al.* Reversible Chemical Switching of a Ferroelectric Film. *Phys. Rev. Lett.* **102**, 047601 (2009).
109 Miller, R. C. & Weinreich, G. Mechanism for the sidewise motion of 180-degrees domain walls in barium titanate. *Phys. Rev.* **117**, 1460-1466 (1960).
110 Brazier, M., Mansour, S. & McElfresh, M. Ferroelectric fatigue of $Pb(Zr,Ti)O_3$ thin films measured in atmospheres of varying oxygen concentration. *Applied Physics Letters* **74**, 4032-4033 (1999).
111 De Araujo, C. A. P., Cuchiaro, J. D., McMillan, L. D., Scott, M. C. & Scott, J. F. Fatigue-free ferroelectric capacitors with platinum-electrodes. *Nature* **374**, 627-629 (1995).
112 Pertsev, N. A. & Koukhar, V. G. Polarization instability in polydomain ferroelectric epitaxial thin films and the formation of heterophase structures. *Phys. Rev. Lett.* **84**, 3722-3725 (2000).
113 Lohse, O., Grossmann, M., Boettger, U., Bolten, D. & Waser, R. Relaxation mechanism of ferroelectric switching in $Pb(Zr,Ti)O_3$ thin films. *J. Appl. Phys.* **89**, 2332-2336 (2001).
114 Gruverman, A. & Tanaka, M. Polarization retention in $SrBi_2Ta_2O_9$ thin films investigated at nanoscale. *J. Appl. Phys.* **89**, 1836-1843 (2001).
115 Ganpule, C. S. *et al.* Polarization relaxation kinetics and 180 degrees domain wall dynamics in ferroelectric thin films. *Phys. Rev. B* **65**, 014101 (2002).
116 Guo, H. Y. *et al.* Study of domain stability on $(Pb_{0.76}Ca_{0.24})TiO_3$ thin films using piezoresponse microscopy. *Applied Physics Letters* **81**, 715-717 (2002).
117 Kang, B. S. *et al.* Polarization retention in $Pb(Zr_{0.4}Ti_{0.6})O_3$ capacitors with IrO_2 top electrodes. *Applied Physics Letters* **84**, 3127-3129 (2004).
118 Kim, D. J. *et al.* Polarization relaxation induced by a depolarization field in ultrathin ferroelectric $BaTiO_3$ capacitors. *Phys. Rev. Lett.* **95**, 237602 (2005).

119 Lou, X. J., Zhang, M., Redfern, S. A. T. & Scott, J. F. Local phase decomposition as a cause of polarization fatigue in ferroelectric thin films. *Phys. Rev. Lett.* **97**, 177601 (2006).
120 Jo, J. Y. *et al.* Polarization switching dynamics governed by the thermodynamic nucleation process in ultrathin ferroelectric films. *Phys. Rev. Lett.* **97**, 247602 (2006).
121 Merz, W. J. Domain Formation and Domain Wall Motions in Ferroelectric $BaTiO_3$ Single Crystals. *Phys. Rev.* **95**, 690-698 (1954).
122 Song, T. K., Aggarwal, S., Prakash, A. S., Yang, B. & Ramesh, R. Activation field of ferroelectric (Pb,La)(Zr,Ti)O_3 thin film capacitors. *Applied Physics Letters* **71**, 2211-2213 (1997).
123 Song, T. K. *et al.* Activation fields in ferroelectric thin film capacitors: Area dependence. *Applied Physics Letters* **73**, 3366-3368 (1998).
124 Hayashi, M. Note on Domain-Wall Motion in Ferroelectric Switching. *J. Phys. Soc. Jpn.* **34**, 1686-1686 (1973).
125 Hashimoto, S., Orihara, H. & Ishibashi, Y. Study of D-E Hysteresis Loop of Tgs Based on the Avrami-Type Model. *J. Phys. Soc. Jpn.* **63**, 1601-1610 (1994).
126 Tagantsev, A. K., Stolichnov, I., Setter, N., Cross, J. S. & Tsukada, M. Non-Kolmogorov-Avrami switching kinetics in ferroelectric thin films. *Phys. Rev. B* **66**, 214109 (2002).
127 Li, Y. W. & Li, F. X. In situ observation of electric field induced crack propagation in $BaTiO_3$ crystals along the field direction. *Scripta Mater.* **67**, 601-604 (2012).
128 Jiang, Y. J. & Fang, D. N. In situ observation of electric-field-induced domain switching and crack propagation in poled PMNT62/38 single crystals. *Mater. Lett.* **61**, 5047-5049 (2007).
129 Grigoriev, A. *et al.* Nanosecond domain wall dynamics in ferroelectric Pb(Zr,Ti)O_3 thin films. *Phys. Rev. Lett.* **96**, 187601 (2006).
130 Zhao, T. *et al.* Electrical control of antiferromagnetic domains in multiferroic $BiFeO_3$ films at room temperature. *Nat. Mater.* **5**, 823-829 (2006).
131 Kalinin, S. V., Rar, A. & Jesse, S. A decade of piezoresponse force microscopy: Progress, challenges, and opportunities. *Ieee T. Ultrason. Ferr.* **53**, 2226-2252 (2006).
132 Kalinin, S. V. *et al.* Nanoscale electromechanics of ferroelectric and biological systems: A new dimension in scanning probe microscopy. *Annu. Rev. Mater. Res.* **37**, 189-238 (2007).
133 Bonnell, D. A., Kalinin, S. V., Kholkin, A. L. & Gruverman, A. Piezoresponse Force Microscopy: A Window into Electromechanical Behavior at the Nanoscale. *MRS Bulletin* **34**, 648-657 (2009).
134 Mitsui, T. & Furuichi, J. Domain Structure of Rochelle Salt and Kh_2Po_4. *Phys. Rev.* **90**, 193-202 (1953).
135 Jesse, S. *et al.* Direct imaging of the spatial and energy distribution of nucleation centres in ferroelectric materials. *Nat. Mater.* **7**, 209-215 (2008).
136 Nelson, C. T. *et al.* Domain dynamics during ferroelectric switching. *Science* **334**, 968-971 (2011).

137 Catalan, G. & Scott, J. F. Physics and Applications of Bismuth Ferrite. *Adv. Mater.* **21**, 2463-2485 (2009).
138 Zavaliche, F. *et al.* Multiferroic $BiFeO_3$ films: domain structure and polarization dynamics. *Phase Transit.* **79**, 991-1017 (2006).
139 Christen, H. M., Nam, J. H., Kim, H. S., Hatt, A. J. & Spaldin, N. A. Stress-induced R-M-A-M-C-T symmetry changes in $BiFeO_3$ films. *Phys. Rev. B* **83** (2011).
140 Giannuzzi, L. A. & Stevie, F. A. A review of focused ion beam milling techniques for TEM specimen preparation. *Micron* **30**, 197-204 (1999).
141 Li, J., Malis, T. & Dionne, S. Recent advances in FIB-TEM specimen preparation techniques. *Mater. Charact.* **57**, 64-70 (2006).
142 Alani, R. Recent Advances in Ion Milling Techniques for Tem Specimen Preparation of Materials. *International Symposium on Electron Microscopy*, 461-478 (1991).
143 Tomus, D. & Ng, H. P. In situ lift-out dedicated techniques using FIB-SEM system for TEM specimen preparation. *Micron* **44**, 115-119 (2013).
144 Barber, D. J. Radiation-Damage in Ion-Milled Specimens - Characteristics, Effects and Methods of Damage Limitation. *Ultramicroscopy* **52**, 101-125 (1993).
145 Barna, A., Pecz, B. & Menyhard, M. TEM sample preparation by ion milling amorphization. *Micron* **30**, 267-276 (1999).
146 Zhang, J. X. *et al.* A nanoscale shape memory oxide. *Nat. Commun.* **4**, 2768 (2013).
147 Junquera, J. & Ghosez, P. Critical thickness for ferroelectricity in perovskite ultrathin films. *Nature* **422**, 506-509 (2003).
148 Fong, D. D. *et al.* Ferroelectricity in ultrathin perovskite films. *Science* **304**, 1650-1653 (2004).
149 Lichtensteiger, C., Triscone, J. M., Junquera, J. & Ghosez, P. Ferroelectricity and tetragonality in ultrathin $PbTiO_3$ films. *Phys. Rev. Lett.* **94**, 047603 (2005).
150 Jia, C. L., Lentzen, M. & Urban, K. Atomic-resolution imaging of oxygen in perovskite ceramics. *Science* **299**, 870-873 (2003).
151 Jia, C. L. *et al.* Unit-cell scale mapping of ferroelectricity and tetragonality in epitaxial ultrathin ferroelectric films. *Nat. Mater.* **6**, 64-69 (2007).
152 Pennycook, S. J. Scanning Transmission Electron Microscopy: Imaging and Analysis. *Springer 2011th Ed.*
153 Krivanek, O. L. *et al.* Atom-by-atom structural and chemical analysis by annular dark-field electron microscopy. *Nature* **464**, 571-574 (2010).
154 Okunishi, E. *et al.* Visualization of Light Elements at Ultrahigh Resolution by STEM Annular Bright Field Microscopy. *Microsc Microanal* **15**, 164-165 (2009).
155 Ishikawa, R. *et al.* Direct imaging of hydrogen-atom columns in a crystal by annular bright-field electron microscopy. *Nat. Mater.* **10**, 278-281 (2011).
156 Jia, C. L. *et al.* Atomic-scale study of electric dipoles near charged and uncharged domain walls in ferroelectric films. *Nat. Mater.* **7**, 57-61 (2008).
157 Kimoto, K. *et al.* Local crystal structure analysis with several picometer precision using scanning transmission electron microscopy. *Ultramicroscopy* **110**, 778-782 (2010).

158 Li, L. Z. *et al.* Atomic scale structure changes induced by charged domain walls in ferroelectric materials. *Nano Lett.* **13**, 5218-5223 (2013).
159 Yamamoto, N., Yagi, K. & Honjo, G. Electron-Microscopic Studies of Ferroelectric and Ferroelastic $Gd_2(MoO_4)_3$. IV. Polarization Reversal and Field-Induced Phase-Transformation. *Phys. Status Solidi A* **62**, 657-664 (1980).
160 Snoeck, E., Normand, L., Thorel, A. & Roucau, C. Electron-Microscopy Study of Ferroelastic and Ferroelectric Domain-Wall Motions Induced by the in-situ Application of an Electric-Field in $BaTiO_3$. *Phase Transit.* **46**, 77-88 (1994).
161 Randall, C. A., Barber, D. J. & Whatmore, R. W. Insitu Tem Experiments on Perovskite-Structured Ferroelectric Relaxor Materials. *J. Microsc.-Oxford* **145**, 275-291 (1987).
162 Tan, X. L., He, H. & Shang, J. K. In situ transmission electron microscopy studies of electric-field-induced phenomena in ferroelectrics. *J. Mater. Res.* **20**, 1641-1653 (2005).
163 He, H. & Tan, X. Electric-field-induced transformation of incommensurate modulations in antiferroelectric $Pb_{0.99}Nb_{0.02}[(Zr_{1-x}Sn_x)_{(1-y)}Ti_y]_{(0.98)}O_3$. *Phys. Rev. B* **72**, 024102 (2005).
164 Qu, W., Zhao, X. & Tan, X. Evolution of nanodomains during the electric-field-induced relaxor to normal ferroelectric phase transition in a Sc-doped $Pb(Mg_{1/3}Nb_{2/3})O_3$ ceramic. *J. Appl. Phys.* **102**, 084101 (2007).
165 Sato, Y., Hirayama, T. & Ikuhara, Y. Real-Time Direct Observations of Polarization Reversal in a Piezoelectric Crystal: $Pb(Mg_{1/3}Nb_{2/3})O_3$-$PbTiO_3$ Studied via In Situ Electrical Biasing Transmission Electron Microscopy. *Phys. Rev. Lett.* **107**, 187601 (2011).
166 Winkler, C. R. *et al.* Accessing intermediate ferroelectric switching regimes with time-resolved transmission electron microscopy. *J. Appl. Phys.* **112**, 052013 (2012).
167 Winkler, C. R., Damodaran, A. R., Karthik, J., Martin, L. W. & Taheri, M. L. Direct observation of ferroelectric domain switching in varying electric field regimes using in situ TEM. *Micron* **43**, 1121-1126 (2012).
168 Chang, H. J. *et al.* Watching domains grow: In-situ studies of polarization switching by combined scanning probe and scanning transmission electron microscopy. *J. Appl. Phys.* **110** (2011).
169 Gao, P. *et al.* Ferroelastic domain switching dynamics under electrical and mechanical excitations. *Nat. Commun.* **5**, 3801 (2014).
170 Gao, P. *et al.* Direct Observations of Retention Failure in Ferroelectric Memories. *Adv. Mater.* **24**, 1106-1110 (2012).
171 Vul, B. M., Guro, G. M. & Ivanchik, I. I. Encountering Domains in Ferroelectrics. *Ferroelectrics* **6**, 29-31 (1973).
172 Gureev, M. Y., Tagantsev, A. K. & Setter, N. Head-to-head and tail-to-tail 180 degrees domain walls in an isolated ferroelectric. *Phys. Rev. B* **83**, 184104 (2011).
173 Qi, Y. J. *et al.* Coexistence of ferroelectric vortex domains and charged domain walls in epitaxial $BiFeO_3$ film on $(110)_O$ $GdScO_3$ substrate. *J. Appl. Phys.* **111**, 104117 (2012).

174 Wang, W. Y. *et al.* Atomic Level 1D Structural Modulations at the Negatively Charged Domain Walls in $BiFeO_3$ Films. *Adv. Mater. Interfaces.* **2**, 1500024 (2015).
175 Gao, P. *et al.* Revealing the role of defects in ferroelectric switching with atomic resolution. *Nat. Commun.* **2**, 591 (2011).
176 Winchester, B., Wu, P. & Chen, L. Q. Phase-field simulation of domain structures in epitaxial $BiFeO_3$ films on vicinal substrates. *Applied Physics Letters* **99**, 052903 (2011).
177 Li, Y. L., Hu, S. Y., Liu, Z. K. & Chen, L. Q. Effect of substrate constraint on the stability and evolution of ferroelectric domain structures in thin films. *Acta Mater.* **50**, 395-411 (2002).
178 Hu, H. L. & Chen, L. Q. Three-dimensional computer simulation of ferroelectric domain formation. *J. Am. Ceram. Soc* **81**, 492-500 (1998).
179 Zhang, J. X. *et al.* Effect of substrate-induced strains on the spontaneous polarization of epitaxial $BiFeO_3$ thin films. *J. Appl. Phys.* **101**, 114105 (2007).
180 Zhang, J. X. *et al.* Three-dimensional phase-field simulation of domain structures in ferroelectric islands. *Applied Physics Letters* **92**, 122906 (2008).
181 Li, Y. L., Hu, S. Y., Liu, Z. K. & Chen, L. Q. Effect of electrical boundary conditions on ferroelectric domain structures in thin films. *Applied Physics Letters* **81**, 427-429 (2002).
182 Tagantsev, A. The role of the background dielectric susceptibility in uniaxial ferroelectrics. *Ferroelectrics* **69**, 321 (1986).
183 Devonshire, A. F. Theory of Barium Titanate .1. *Philos. Mag.* **40**, 1040-1063 (1949).
184 Chen, L. Q. Phase-field method of phase transitions/domain structures in ferroelectric thin films: A review. *J. Am. Ceram. Soc* **91**, 1835-1844 (2008).
185 Lubk, A., Gemming, S. & Spaldin, N. A. First-principles study of ferroelectric domain walls in multiferroic bismuth ferrite. *Phys. Rev. B* **80**, 104110 (2009).
186 Lubk, A. *et al.* Evidence of Sharp and Diffuse Domain Walls in $BiFeO_3$ by Means of Unit-Cell-Wise Strain and Polarization Maps Obtained with High Resolution Scanning Transmission Electron Microscopy. *Phys. Rev. Lett.* **109**, 047601 (2012).
187 Vasudevan, R. K. *et al.* Nanoscale Control of Phase Variants in Strain-Engineered BiFeO3. *Nano Lett* **11**, 3346-3354 (2011).
188 Rossell, M. D. *et al.* Atomic Structure of Highly Strained $BiFeO_3$ Thin Films. *Phys. Rev. Lett.* **108**, 047601 (2012).
189 Fong, D. D. *et al.* Stabilization of monodomain polarization in ultrathin PbTiO3 films. *Phys Rev Lett* **96**, 127601 (2006).
190 Liu, Y. Y., Liu, J. J., Xie, S. H. & Li, J. Y. Energetics of charged domain walls in ferroelectric crystals. *Appl Phys Lett* **91**, 172910 (2007).
191 Kresse, G. & Furthmuller, J. Efficient iterative schemes for ab initio total-energy calculations using a plane-wave basis set. *Phys. Rev. B* **54**, 11169-11186 (1996).
192 Blochl, P. E. Projector Augmented-Wave Method. *Phys. Rev. B* **50**, 17953-17979 (1994).

193 Dudarev, S. L., Botton, G. A., Savrasov, S. Y., Humphreys, C. J. & Sutton, A. P. Electron-energy-loss spectra and the structural stability of nickel oxide: An LSDA+U study. *Phys. Rev. B* **57**, 1505-1509 (1998).
194 Monkhorst, H. J. & Pack, J. D. Special Points for Brillouin-Zone Integrations. *Phys. Rev. B* **13**, 5188-5192 (1976).
195 Neaton, J. B., Ederer, C., Waghmare, U. V., Spaldin, N. A. & Rabe, K. M. First-principles study of spontaneous polarization in multiferroic $BiFeO_3$. *Phys. Rev. B* **71**, 014113 (2005).
196 Kingsmith, R. D. & Vanderbilt, D. Theory of Polarization of Crystalline Solids. *Phys. Rev. B* **47**, 1651-1654 (1993).
197 Xue, F., Gu, Y. J., Liang, L. Y., Wang, Y. & Chen, L. Q. Orientations of low-energy domain walls in perovskites with oxygen octahedral tilts. *Phys. Rev. B* **90**, 220101 (2014).
198 Li, Q. *et al.* Giant elastic tunability in strained $BiFeO_3$ near an electrically induced phase transition. *Nat. Commun.* **6**, 8985 (2015).
199 Miao, Q. *et al.* Self-assembled nanoscale capacitor cells based on ultrathin $BiFeO_3$ films. *Applied Physics Letters* **104**, 182903 (2014).
200 Chen, L. Q. & Shen, J. Applications of semi-implicit Fourier-spectral method to phase field equations. *Computer Physics Communications* **108**, 147-158 (1998).
201 Lee, D. *et al.* Emergence of room-temperature ferroelectricity at reduced dimensions. *Science* **349**, 1314-1317 (2015).
202 Stengel, M., Vanderbilt, D. & Spaldin, N. A. Enhancement of ferroelectricity at metal-oxide interfaces. *Nat. Mater.* **8**, 392-397 (2009).
203 Hull, S. *et al.* Neutron total scattering study of the delta and beta phases of Bi_2O_3. *Dalton T* **40**, 8737-8745 (2009).
204 Marti, X. *et al.* Skin Layer of $BiFeO_3$ Single Crystals. *Phys. Rev. Lett.* **106**, 236101 (2011).
205 Jarrier, R. *et al.* Surface phase transitions in $BiFeO_3$ below room temperature. *Phys. Rev. B* **85**, 184104 (2012).
206 Tang, W., Sanville, E. & Henkelman, G. A grid-based Bader analysis algorithm without lattice bias. *J. Phys.-Condens. Mat.* **21**, 8 (2009).
207 Seidel, J. *Topological Structures in Ferroic Materials Domain Walls, Vortices and Skyrmions Preface*. (Springer, 2016).
208 Wei, X. K. *et al.* Ferroelectric translational antiphase boundaries in nonpolar materials. *Nat. Commun.* **5**, 3031 (2014).
209 Privratska, J. & Janovec, V. Pyromagnetic domain walls connecting antiferromagnetic non-ferroelastic magnetoelectric domains. *Ferroelectrics* **204**, 321-331 (1997).
210 Privratska, J. & Janovec, V. Spontaneous polarization and or magnetization in non-ferroelastic domain walls: Symmetry predictions. *Ferroelectrics* **222**, 23-32 (1999).
211 Kezsmarki, I. *et al.* Neel-type skyrmion lattice with confined orientation in the polar magnetic semiconductor GaV4S8. *Nat. Mater.* **14**, 1116-+ (2015).
212 Rossler, U. K., Bogdanov, A. N. & Pfleiderer, C. Spontaneous skyrmion ground states in magnetic metals. *Nature* **442**, 797-801 (2006).

213 Muhlbauer, S. *et al.* Skyrmion Lattice in a Chiral Magnet. *Science* **323**, 915-919 (2009).
214 Yu, X. Z. *et al.* Real-space observation of a two-dimensional skyrmion crystal. *Nature* **465**, 901-904 (2010).
215 Heinze, S. *et al.* Spontaneous atomic-scale magnetic skyrmion lattice in two dimensions. *Nat. Phys.* **7**, 713-718 (2011).
216 Schulz, T. *et al.* Emergent electrodynamics of skyrmions in a chiral magnet. *Nat. Phys.* **8**, 301-304 (2012).
217 Jonietz, F. *et al.* Spin Transfer Torques in MnSi at Ultralow Current Densities. *Science* **330**, 1648-1651 (2010).
218 Wachowiak, A. *et al.* Direct observation of internal spin structure of magnetic vortex cores. *Science* **298**, 577-580 (2002).
219 Ivry, Y., Chu, D. P., Scott, J. F. & Durkan, C. Flux Closure Vortexlike Domain Structures in Ferroelectric Thin Films. *Phys. Rev. Lett.* **104** (2010).
220 Yadav, A. K. *et al.* Observation of polar vortices in oxide superlattices. *Nature* **530**, 198-+ (2016).
221 MacLaren, I. *et al.* Local stabilisation of polar order at charged antiphase boundaries in antiferroelectric $(Bi_{0.85}Nd_{0.15})(Ti_{0.1}Fe_{0.9})O_3$. *Apl Mater.* **1**, 021102 (2013).
222 MacLaren, I. *et al.* The atomic structure and chemistry of Fe-rich steps on antiphase boundaries in Ti-doped $Bi_{0.9}Nd_{0.15}FeO_3$. *Apl Mater.* **2**, 066106 (2014).
223 Kim, Y. M. *et al.* Direct observation of ferroelectric field effect and vacancy-controlled screening at the $BiFeO_3/La_xSr_{1-x}MnO_3$ interface. *Nat. Mater.* **13**, 1019-1025 (2014).
224 Kim, Y. M. *et al.* Probing oxygen vacancy concentration and homogeneity in solid-oxide fuel-cell cathode materials on the subunit-cell level. *Nat. Mater.* **11**, 888-894 (2012).
225 Wang, J., Xia, Y. F., Chen, L. Q. & Shi, S. Q. Effect of strain and deadlayer on the polarization switching of ferroelectric thin film. *J. Appl. Phys.* **110**, 114111 (2011).
226 Stengel, M. & Spaldin, N. A. Origin of the dielectric dead layer in nanoscale capacitors. *Nature* **443**, 679-682 (2006).
227 Tagantsev, A. K. & Gerra, G. Interface-induced phenomena in polarization response of ferroelectric thin films. *J. Appl. Phys.* **100**, 051607 (2006).
228 Guo, E. J., Roth, R., Das, S., Herklotz, A. & Dorr, K. Strain-induced improvement of retention loss in $PbZr_{0.2}Ti_{0.8}O_3$ films. *Applied Physics Letters* **106**, 072904 (2015).
229 Lee, D. *et al.* Flexoelectric Control of Defect Formation in Ferroelectric Epitaxial Thin Films. *Adv. Mater.* **26**, 5005-5011 (2014).
230 Paruch, P., Giamarchi, T. & Triscone, J. M. Domain wall roughness in epitaxial ferroelectric $PbZr_{0.2}Ti_{0.8}O_3$ thin films. *Phys. Rev. Lett.* **94**, 197601 (2005).
231 Vrejoiu, I. *et al.* Threading dislocations in epitaxial ferroelectric $PbZr_{0.2}Ti_{0.8}O_3$ films and their effect on polarization backswitching. *Philos. Mag.* **86**, 4477-4486 (2006).
232 Huang, Y. C. *et al.* Giant Enhancement of Ferroelectric Retention in $BiFeO_3$ Mixed-Phase Boundary. *Adv. Mater.* **26**, 6335-6340 (2014).

233 Gao, P. *et al.* Atomic-scale mechanisms of ferroelastic domain-wall-mediated ferroelectric switching. *Nat. Commun.* **4**, 2791 (2013).
234 Withers, R. L., Thompson, J. G. & Rae, A. D. The Crystal-Chemistry Underlying Ferroelectricity in $Bi_4Ti_3O_{12}$, Bi_3TiNbO_9, and Bi_2WO_6. *J. Solid State Chem.* **94**, 404-417 (1991).
235 Deniz, H. *et al.* Nanoscale Bi_2FeO_{6-x} precipitates in $BiFeO_3$ thin films: a metastable Aurivillius phase. *Journal of Materials Science* **49**, 6952-6960 (2014).
236 Liu, H. J. *et al.* Origin of a Tetragonal $BiFeO_3$ Phase with a Giant c/a Ratio on $SrTiO_3$ Substrates. *Adv. Funct. Mater.* **22**, 937-942 (2012).